

NAPTC-AED-1869

NAVAL AIR PROPULSION TEST CENTER

TRENTON, NEW JERSEY 08628

DRF-05091

N69-28029

NASA CR-101348

NAVAL AIR PROPULSION TEST CENTER
AERONAUTICAL ENGINE DEPARTMENT
NAVAL BASE, PHILADELPHIA, PA. 17112

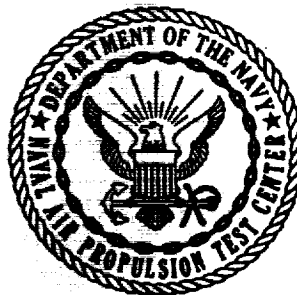
NAPTC-AED-1869

5 APR 1968

ROTOR BURST PROTECTION PROGRAM
INITIAL TEST RESULTS

PHASE IV - FINAL REPORT
PROBLEM ASSIGNMENT NASA DPR R-105

CASE FILE COPY



100 8012

NAVAL AIR PROPULSION TEST CENTER
AERONAUTICAL ENGINE DEPARTMENT
NAVAL BASE, PHILADELPHIA, PA. 19112

NAPTC-AED-1869

5 APR 1968

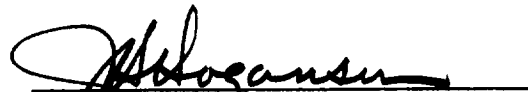
ROTOR BURST PROTECTION PROGRAM
INITIAL TEST RESULTS

PHASE IV - FINAL REPORT
NASA DPR R-105

Prepared by:

Authenticated by:


A. A. MARTINO
P. A. Engineer


J. L. HOGANSON
Commander, USN
Director


G. J. MANGANO
Test Engineer

PRIMARY DISTRIBUTION

NAVAIRSYSCOM INTERNAL

AIR-536
AIR-5360
AIR-5361
AIR-5362
AIR-5364
AIR-5367
AIR-530
AIR-330
AIR-414
DNL MAT 03L

OTHER ACTIVITIES

CO,NADC, Johnsville, Pa.
CO,NAPTC, Trenton, N. J.
NASA, Lewis Research Center (38)
NASA, Washington, D. C. (23)
FAA, Washington, D. C. (2)
ONR London
CO, NAEC (Library)
NASC,NAS, Norfolk, Va.
AEDC, Tullahoma, Tenn.
USNPGS, Monterey, Cal.
U.S.A. AML, Ft. Eustis, Va.
USAAMC, St. Louis, Mo.
AFSC, (APE) WPAFB, Ohio
CNO, Washington, D. C.

TABLE OF CONTENTS

<u>TITLE</u>	<u>PAGE NO.</u>
LIST OF PLATES	1 - 4
INTRODUCTION	5 - 11
CONCLUSIONS	12 - 13
RECOMMENDATIONS	14
DESCRIPTION OF TEST EQUIPMENT & INSTRUMENTATION	
Spin Chamber	15
Vacuum System	15
Drive System	15
High Speed Photographic System	15
Impact Strain Measuring System	16
PROCEDURES, METHODS & TECHNIQUES USED IN CONTAINMENT SYSTEM	
Types of Fragment Generators	16
Inducing a Controlled Disk Burst	16
Errors in Burst Speed Estimation	17
Resolving the Exact Speed of Burst	17
Producing a Blade Failure	17
Photographing a Rotor Burst - Some Problems & Techniques	18
Photo Lighting System	18
Increasing the Light Coverage	19
Film	19
Black & White	19
Color	19

TABLE OF CONTENTS (cont'd)

<u>TITLE</u>	<u>PAGE NO.</u>
Camera	19
Film Loading	19
Optical System - Subject Alignment	20 - 21
ANALYSIS OF RESULTS AND DISCUSSION	
Test Objectives & Data Compilation	22
Fragment Trajectory and Motion	22
Flat Disk	23
Rotor Blades	
Single Blade Failures	23 - 24
Partially Full Rotor (Blade Hammering)	24 - 25
Effect of Radial Clearance	25 - 28
Stress Concentration Effects	29
Starter Rotor Tri-Hub Burst	29 - 30
Material Evaluation	30 - 33
Fragment Shape Effects	34 - 36
REFERENCES	37
ACKNOWLEDGEMENT	38
APPENDICES 1 - 3	
ABSTRACT CARD	

LIST OF PLATES

<u>TITLE</u>	<u>PLATE NO.</u>
Development of a Turbomachine Containment/Control System Mathematical Model	1
Experimental Verification of Computer Model	2
Present Stage of Investigation	3
Air-powered Eight Inch Drive Turbine	4
Drive Spindle and Shaft Assembly for the Eight Inch Drive Turbine	5
Drive Shaft Arrestor	6
Typical Modified Flat Disk	7
Typical Modified Rotor Blade	8
Detail View of Photographic Set-up	9
Photo-lighting Head Modification	10
Color Photo Test Results	11
Proper Alignment for Camera-Mirror-Subject Components	12
Alignment Set-up for Camera-Mirror-Subject Components	13
Fragment Trajectory and Motion	14
Ideal Tri-hub Burst	15
Single Blade-Ring Interaction	16
Ring Deformation Due to a Single Blade Impact	17
Single Blade Dynamics and Ring Interactions	18
Post-test No. 10 Containment Ring	19
Post-test No. 10 Containment Ring Rubbed Area Detail	20

LIST OF PLATES

<u>TITLE</u>	<u>PLATE NO.</u>
Post-test No. 10 Containment Ring - Impacted Area Detail	21
Post-test No. 7 Containment Ring	22
Test No. 11, Blade Failure From a Partially Full Rotor	23
Post-test No. 11 Containment Ring	24
Post-test No. 11 Containment Ring - Detail of Impacted Area	25
Rotor Fragment Kinematics & Fragment-Ring Interactions	26
Post-test No. 4 Containment Ring	27
Post-test No. 4 Containment Ring - Fragment A Impacted Area	28
Post-test No. 4 Containment Ring - Fragment B Impacted Area	29
Post-test No. 4 Containment Ring - Fragment C Impacted Area	30
Test No. 6, Tri-hub Burst Within a Steel Ring; Large Radial Clearance	31
Post-test No. 6 Containment Ring	32
Post-test No. 6 Containment Ring - Fragment C Impacted Area	33
Drawing - Containment Ring Used for Tests 12, 13, 14, 15 & 21	34
Test No. 12 Containment Ring	35
Test No. 12 - Tri-hub Burst Within a Steel Ring; Small Radial Clearance	36
Post-test No. 12 Containment Ring	37
Post-test No. 12 Containment Ring - Fragment A Perforated Area	38
Post-test No. 12 Containment Ring - Bulged-out Center Section	39
Test No. 6 Containment Ring	40
Post-test No. 6 Containment Ring - Fragment A Impacted Area	41

LIST OF PLATES

<u>TITLE</u>	<u>PLATE NO.</u>
Post-test No. 6 Containment Ring - Fragment B Impacted Area	42
Post-test No. 6 Containment Ring - Fragment C Impacted Area	43
Post-test No. 5 Containment Ring	44
Post-test No. 5 Containment Ring - Perforated Area	45
Test No. 20, Pre-test Assembly	46
Post-test No. 20, Ring, Rotor, and Drive Spindle	47
Post-test No. 20 - Fragment Indentation on Inside Surface of Containment Ring	48
Test No. 17 Doron-Alumina Containment Device	49
Test No. 17, Tri-hub Rotor Within a Doron-Alumina Containment Device	50
Post-test No. 17 Fragment Generator	51
Post-test No. 17 Doron Inserts and Alumina Tile	52
Test No. 17 Doron Inserts	53
Fragment Shape Effect Data Compilation	54
Test No. 13, Fragment Shape Effects - Bi-hub Burst	55
Post-test No. 13 Containment Ring Distortion	56
Post-test No. 13 Containment Ring - Detail of Openings	57
Test No. 15, Fragment Shape Effects - Tri-hub Rim Burst	58
Post-test No. 15 Containment Ring	59
Post-test No. 15 Containment Ring - Indentation Details	60
Test No. 21, Fragment Shape Effects - Quad-hub Burst	61
Post-test No. 21 Containment Ring	62

LIST OF PLATES

<u>TITLE</u>	<u>PLATE NO.</u>
Post-test No. 14 Containment Ring, Opening "B" Detail	63
Post-test No. 14 Containment Ring, Opening "A" Detail	64

INTRODUCTION

1. The purpose of this report is to present the results of the first series of tests conducted by the Aeronautical Engine Department, Naval Air Propulsion Test Center, in support of Phase IV of the NASA-sponsored Rotor Burst Protection Program (reference a). The ultimate goal of this integrated program of theoretical and experimental research work is to provide lightweight containment/control systems that will prevent the fragments from failed turbo machines from injuring personnel and damaging adjacent equipment.

2. The previous three years of endeavor by the Aeronautical Engine Department, under the sponsorship of a NASA DPR R-105, amendments 1 and 2, have provided the first full-scale Government attempt to actively pursue this problem in depth and provide a means to scientifically investigate this heretofore scarcely explored field. The only attempts known to us, prior to the initiation of the Rotor Disk Burst Protection Program at the AED, were cut-and-try attempts by turbomachinery manufacturers only after a containment problem had become apparent. These attempts were usually limited by the availability of funds and time, and in most instances the solution was a heavy metallic ring that imposed a considerable weight penalty upon the equipment in trouble. A large percentage of the AED's previous effort was devoted to the design and construction of the Containment Evaluation Facility. Now that this

unique facility has been completed, AED's engineering effort has been directed to the continued development of test techniques and the design, testing, and evaluating of containment/control systems.

3. The problem of uncontained failures in associated APU's and starters is still very much with us. This is evidenced by the record of commercial airlines and U. S. Naval aviation experience reported herein in Appendix 1. Both the number of uncontained failures and the rate of these possibly catastrophic occurrences have increased from calendar year 1964 to calendar year 1966, and early 1967 data indicate that the uncontained problem is becoming more critical.

4. To better understand and appreciate AED's testing to date and the overall Rotor Burst Protection Program, a review of this program is desirable.

5. To scientifically investigate the problem of uncontained turbo-machine failures and eventually design a satisfactory containment/control device, one must first understand what happens in those few milliseconds when the rotor fragments attack the shroud or casing.

6. What are the forces, both quantitative and qualitative, being imposed upon the casing by the fragments?

What type of penetration process is taking place?

Are the fragments changing shape and size during the attack?

Is the entire case working to defeat the fragments or just the immediate area of the impact?

These are some of the questions that require answers. The objective of our studies is to answer these and other questions; and in doing so, generate realistic design data to assist all those interested in the design and production of satisfactory rotor burst containment/control systems.

7. To accomplish this objective, we have created both a program and a facility to support this program. The details concerning the construction of, and the equipment used in AED's Containment Evaluation Facility were reported in references b and c. Let us now look at the overall rotor burst protection program.

8. Containment programs in the past have been largely concerned with cut-and-try approaches which based the next test on the results obtained from the previous testing. The unimaginative plodding that usually accompanies such cut-and-try programs are both time-consuming and expensive and the results are usually the specific answers to one distinct containment problem and not necessarily protection at a minimum weight. Other attempts at containment designs, such as correlation of ballistic data to rotor fragment penetration, or utilization of designs and materials used on previous products are also without a good theoretical foundation. As mentioned in reference d, "Science advances in a series of alteration between theory and experiment. Theoretical formulations become mere speculation if sufficient empirical data are not available, because unless there are data points to which curves

can be fitted, it is meaningless to continue theorizing. However, the inefficiency and even futility of conducting tests without a theoretical background should also be realized."

9. A theoretical framework should be available so that the relationship between variables can be predicted quantitatively before the experiment or test is conducted. If the proper kind of theory is available, the engineer can plan his test so that the most important variables are investigated first while the second order of effect variables are given lower priority. It is this basic philosophy that is to be generally followed whenever possible throughout the Rotor Burst Protection program.

10. What a turbomachine manufacturer would like to have is a computer into which he could describe his machine, his proposed containment device, the operating conditions and environment, and then push a button and have the machine accurately tell him how the containment device will behave. The "magic box" we are speaking of is actually a computerized mathematical model (or models) that describes, through a series of equations, the interaction of the rotor fragments and the containment system.

11. A basic approach to develop such a mathematical model adopted by the AED is depicted on plate 1. The desired "magic box" is designated "computer model" and to obtain this model we must first begin at the far left of the diagram at the "system block." We must first know our system, i.e., our turbomachine and containment concept we are considering. The system must then be described as accurately as possible. By description, we mean both the physical characteristics of the system and the types of

interaction that can take place when a burst occurs. The "information source" block is where we go to get the information to aid in our system description. The more information available here, the more realistic is our system description and therefore so is our computer model. If more information is needed to fill these information gaps, additional supporting experiments must be designed and performed.

12. Now probably the most difficult portion of the development must be considered; the "mathematical model." The mathematical model must combine the physical characteristics and properties of the entire system with the laws of motion and force. This is to be done through theoretical formulation and mathematical analyses. In general, such mathematical models, when applied to ballistics or hypervelocity impacts, have been successful for only a particular set of conditions. It is our hope to generate a mathematical model accommodating the entire range of turbo-machines or at least a minimum number of ranges based upon size or some selected characteristic. The mathematical model will probably be quite complex, and the requirement for computerizing the mathematical model through proper programming is foreseen to obtain our "magic box" containment/control system mathematical model.

13. Once the computer model is established it will be necessary to verify how accurately the model depicts the actual system. Plate 2 illustrates one method to accomplish this. A computer model based upon

a sound theoretical background should require only a small number of actual comparative tests and computer parameter adjustments before proving to be a useful design tool.

14. The present state of AED's investigation at the end of phase IV is shown on plate 3. The major portion of AED's effort during phase IV of the RPB Program and the eventual attainment of a useful mathematical model was devoted to filling the information gap in this heretofore slightly studied field. While obtaining information about fragment kinematics and material reactions to the complex type of failure, AED was also, with each test, developing their test techniques and technical background. In addition to the tests designed to examine the previously mentioned factors, AED also conducted tests to evaluate new materials which, although not specifically designated for use as fragment containment materials, were intuitively considered as having possible applications in this field, and therefore, worth investigating.

15. The complexities of our investigation can better be understood by examining some of the factors that influence the containment/control process. Details concerning these items are discussed in reference b and will not be repeated here, but the following list will serve as a reminder:

MATERIAL

1. Strength
 - Static & Dynamic
2. Composition
3. Environmental Limits

DESIGN

1. Overall Product Design
2. Type of Support-Restraint System

DYNAMICS

1. Fragment Characteristics
 - a. Shape
 - b. Mass
 - c. Velocity
 - d. Orientation
2. Energy Distribution
 - a. Translation
 - b. Rotation
3. Deformation
 - a. Localized
 - b. Gross

CONCLUSIONS

16. The NASA sponsored Rotor Burst Protection program has produced the first high speed photographic sequence of an intentionally failed rotor within a containment device. This technical achievement has produced a means to both qualitatively and quantitatively study the fragment-containment system kinematics and material performance associated with disk and blade failures.

17. The qualitative results of the first twenty-one tests reported herein provide data that can assist in establishing basic guidelines for the design of containment systems.

18. Experimental results illustrate that fragments from a flat disk rotate about their own center of mass as they move tangentially outward. This combined type of action produces a complex failure mode of the containment system.

19. Single blade failures from a partially bladed turbine rotor travel in the same manner as described above.

20. The effect of radial clearance on the containment process was shown to be significant. Large clearances increase the possibility of a fragment contacting the containment device in a critical manner.

21. The inclusion of areas of possible stress concentrations can drastically reduce the containment potential of a containment system.

22. Based on the limited number of tests conducted, there is no one definite kinetic energy component, i.e., translational or rotational, that dominates the containment process. Fragment mass also has no apparent direct relationship to fragment containment.

22. The containment test of the Doron-Alumina "ring" indicated that these two materials have a potential for future containment/control systems.

23. The theoretical derivation and related curves of the energy distribution of fragments from a rotating flat disk provide the total, translational, and rotational kinetic energy per fragment for combinations of fragment included angle and radius ratio.

24. High speed color film evaluation tests within Spin Chamber No. 1 have produced relationships between operating conditions (light intensity, light duration, and a camera framing rate) and photograph quality.

25. The modification to certain photographic system equipment and refinements of spin test techniques have increased the quality and quantity of AED's testing.

26. Both the U.S. Commercial and Naval Aviation data reported herein give evidence to the fact that uncontained failures present an ever increasing danger to the operational safety of turbomachinery. The possible catastrophic proportions of this problem demand a rapid solution.

RECOMMENDATIONS

27. Support should be continued for the AED's integrated program of theoretical and experimental research effort toward the attainment of satisfactory containment/control systems.

28. Additional program support should be enlisted to aid in the development of theoretical models and analytical methods. Details concerning such a supplemental program would basically provide a theoretical model of the containment/control system under attack by fragments from a failed rotor. This model would provide transient signatures of the fragment-containment system and afford a basis for comparison between actual hardware and computer simulation.

29. That phase of the RBP program concerned with the control or redirection of fragments away from critical areas (fuel tanks, fuselage, nearby engines, heavily concentrated areas of control cables) and into less sensitive areas should receive a greater portion of the program effort.

30. The containment section of all specifications relative to turbo-machine qualification and/or certification should be reviewed in light of the RBP program and the apparent differences between small engine and ever-growing auxiliary power unit containment requirements.

31. A greater number of lightweight materials (fiber reinforcements especially) and design innovations should be introduced into the program for evaluation whenever the opportunity presents itself.

DESCRIPTION OF TEST EQUIPMENT AND INSTRUMENTATION

The following paragraphs will briefly describe the facilities used for the tests reported. A more comprehensive and detailed description of the Aeronautical Engine Department's Containment Evaluation Facility can be found in reference b.

SPIN CHAMBER

32. All the early disk and blade burst tests were conducted in Chamber 1 of the AEDCEF.

VACUUM SYSTEM

33. During most of these tests the chamber was evacuated to a pressure of 8 mm Hg abs. using six Kinney "110" vacuum pumps.

DRIVE SYSTEM

34. A Barbour-Stockwell 8 inch air turbine motor (speed range 0-25000 rpm) was used to rotate the disks and rotors to the burst speeds. A picture of this turbine and a drawing of the drive spindle and shaft assembly are shown in plates 4 and 5.

35. The drive assembly shown was selected for use because of its simple design, which permitted swift and inexpensive manufacture. These were important considerations because invariably the drive spindle, adapter and shaft were grossly deformed during each test.

36. The drive shaft arrester shown in plate 6 was used during the latter phase of testing to constrain excessive lateral motion of the drive shaft caused by the dynamic imbalance induced by a staggered fragment burst. If the motion were not limited, the shaft became progressively deformed and began whipping; often striking the containment device and causing excessive and unrealistic deformation.

During spin-up the drive shaft was not in contact with the bronze journal bearings of the shaft arrester - a radial clearance of approximately 0.050 was provided. Only when the drive assembly became imbalanced (after burst) and experienced relatively excessive lateral motion did the drive shaft contact the bearings. This allowed the drive assembly to retain its simply suspended configuration, (enabling the assembly to seek its own center of rotation) until burst occurred. This allows us to spin successfully, within our test speed range, without critically balancing the rotors used.

HIGH SPEED PHOTOGRAPHIC SYSTEM

37. A high speed photographic system capable of taking 224 pictures at a rate of 35000 pictures/second was used to photo-record events occurring in the chamber. This system consisted of a Beckman & Whitely Model 350

(Dynafax) continuous framing camera and two B&W Model 358 Electronic Flash photo lighting units.

IMPACT STRAIN MEASURING SYSTEM

38. An impact strain measuring system was used to measure and record the strains induced in the containment device by fragment impact. This system consisted of four foil type strain gages, Wheatstone bridges and two dual beam oscilloscopes outfitted with trace recording cameras. The system provided four channels of photo-recorded (Polaroid) continuous strain information.

PROCEDURES, METHODS & TECHNIQUES USED IN CONTAINMENT TESTING

TYPES OF FRAGMENT GENERATORS

39. Two types of rotors were used as fragment generators during the course of testing.

a. Flat steel disks 7 inches in diameter, and 3/8 of an inch thick that were manufactured "in-house", and

b. Axial flow rotors from various starters and engines. Depending on the type of test to be conducted, these rotors were "doctored" or modified to burst into fragments of specific shapes and sizes (blades or disk sectors) at predetermined rotational speeds.

INDUCING A CONTROLLED DISK BURST

40. The rotors used for disk burst tests (whether they were actual turbomachine rotors or flat disks) were modified as shown in plate 7. This modification provided a disk configuration in which the anticipated fragments (usually annular disk sectors - the size and shape of which are governed by test requirements) were integrally connected to the hub by what we termed "tensile release sections." This name arises from the fact that these release sections are placed in uniaxial tension by the centripetal forces generated during rotor or disk rotation. When a speed is reached that induces a tensile stress that exceeds the material strength, the section fails and the fragment is released from the hub. This configuration was used because:

a. It causes a uniaxial tensile stress field to be developed in the release section, rather than a more complex stress field as other arrangements, such as in a webbed release section.

b. It increases the accuracy of burst speed estimation. Handbook values of material strength used to calculate the burst speed are derived through uniaxial tensile testing; the same type of loading that the tensile release section experiences until failure.

c. It is an easy configuration to manufacture. Tolerances are not hard to hold because simple but accurate machine tools are used and also there is less chance for tool scarring to occur.

ERRORS IN BURST SPEED ESTIMATION

41. A review of plates 1, 2, and 3 of Appendix 3 shows that there is a difference between the "design" or estimated burst speeds and the actual burst speeds. This difference could be caused by any one or a combination of the following:

- a. Variations in the mechanical properties of the materials used.
- b. Material imperfections.
- c. Dimensional deviations caused by the normal tolerances of manufacture..
- d. Abnormal, but sometimes unavoidable, manufacturing deviations such as tool scars which give rise to unaccounted for stress concentrations.
- e. The simplifying assumptions used in pre-test stress analysis.
- f. Experimental error involved in measurements (fragment weights and centroids for example) taken for pre-test analysis.

All of these factors contribute toward causing a discrepancy between the calculated and actual burst speed. It is difficult to predict what the deviation will be for a particular configuration because these factors can reinforce or cancel their respective effects, e.g., the error in measuring or calculating a fragment centroid (say, making it smaller than it actually is) might be offset by a material strength that is actually higher than that used in the calculations.

PRODUCING A BLADE FAILURE

42. Blade failures at predicted speeds were induced by modifying the blade as shown in plate 8. This consisted of reducing the area normally required to support the centripetal load generated during rotation. A straight-forward centripetal force analysis was used $\sigma_u A = (W/g) \bar{r} \omega^2$ to determine the burst speed. We found that the simplest and most accurate way to get the values of W (the weight) and \bar{r} (the centroid) for a particular blade was to determine them experimentally.

PHOTOGRAPHING A DISK OR BLADE BURST - SOME PROBLEMS & TECHNIQUES

43. The type of equipment used to take high speed photographs of bursts has been described in paragraph 37. Now we will discuss some of the problems encountered in our particular application of this equipment and describe the techniques we used to solve these problems. But first let us describe how the equipment was used.

44. The subject, usually a turbine rotor or disk suspended from a drive system mounted on the chamber lid, was illuminated by reflecting the light from the photo flash unit heads off a flat front surface mirror centered below the subject and inclined at an angle of 45° from the optical axis of the photo light reflectors.. Two photo lighting heads consisting of a flash tube and reflector were used. They were positioned inside the chamber between the vacuum shell and steel protective liner. Pictures were taken of the subject image formed by the same mirror used to transmit the light. Similarly, the optical axis of the camera taking lens formed an angle of 45° with the plane of the mirror. Refer to plate 9 which shows the set-up just described. To take high speed pictures: the test cell was completely darkened; the camera was accelerated to the desired framing rate (it can maintain a constant framing rate for as long as 30 minutes or as short as 5 minutes - depending on the framing rate used); the camera capping shutter was opened; and the event or burst which triggered the photo lighting system was made to occur. Details on how the event was used to trigger the photo lights are presented in reference b. The duration of the photo lights were selected so that film rewrite on the continuous film strip did not occur. This was the procedure used to take high-speed photographs of the bursts.

45. Now we will discuss some of the techniques used and problems encountered in implementing these methods and procedures.

a. The Photo Lighting System

(1) Photo flash tube voltage breakdown difficulties- The flash tubes used in the photo lighting heads that operated inside the spin chamber experienced a voltage breakdown when the chamber was evacuated. These flash tubes, although they were rated and performed satisfactorily at normal atmospheric conditions, could not function without arcing under the vacuum conditions imposed on them during test. The solution to this problem was to envelop the photo lighting head and vent the envelope to the atmosphere. This was done as shown in plate 10 without lessening the light output of the tube or restricting the flexibility and function of the photo lighting head assembly.

(2) Increasing the light coverage - The photo lighting head consists of a flash tube & a tubular casing that houses the flash hyperbolic reflector whose illumination focus could be varied by sliding the reflector along the axis of the casing. Refer to plate 10. For a fixed light to subject distance (as was our case), the area covered by the light when focused for maximum intensity is also fixed. In some instances, where large rotors were to be photographed, the focused light coverage was not enough to satisfactorily illuminate the entire area of interest. In these cases a fixed focus 7 inch diameter parabolic reflector (Graflex press type reflector) was used to increase the light coverage with good results.

b. Film

(1) Black and White - Very satisfactory photos were taken using both Kodak 2475 and 2485 films. The 2485 film is about twice as fast as the 2475 and extends our picture taking capability using the photo lighting system described to include the entire framing rate range of the camera, which is 200 to 35000 pps. In all cases these films were processed as specified by the manufacturer in references f and g.

(2) Color - A photo system test program was conducted using Kodak type EF5241 Ektachrome Color film. The purpose of this program was to determine at what maximum camera framing rates could satisfactory color pictures be taken using either one or two of the photo lighting units when operated at their three difference light intensity output settings. The results of these tests are presented in plate 11. They indicate that good photos can be taken at camera framing rates as high as 15,000 pictures/second when using two photo lighting units set for maximum light output intensity.

c. Camera (Dynafax)

(1) Film loading - The most difficult operation when using the Dynafax camera is loading the film into the camera. It is not physically difficult to load the camera. The problem lies in being sure that the film is properly installed and has not fallen, or will not fall, from its mounting groove. The corrective procedure we established is to load the film, place the camera in a darkened room (or darken the room in which it is), remove the loading cassette and feel, by hand, if the film is firmly in place. It is worth the extra time it takes to go through this procedure because there is no way of telling if the film is not mounted properly or has fallen until after the test has been conducted, and this is an inopportune time to make the discovery.

(2) Optical System-Subject Alignment. Plate 9 shows the general arrangement of camera, photo lights, and imaging mirror used to take high speed photographs of the burst tests conducted. Since the pictures taken were to be used to get quantitative data describing the burst (such as fragment motion, speed, orientation, etc), the subject, camera optical system, and mirror had to be properly aligned. Proper alignment of these elements satisfied the following conditions (refer to plate 12).

(a) The plane of the mirror made an angle of 45° with the absolute horizontal plane.

(b) A plane parallel to the horizontal plane and containing the optical axis of the camera system made an interior angle of 45° with the mirror plane.

(c) The line of intersection formed by the plane containing the optical axis and the plane of the mirror was perpendicular to the optical axis of the camera system.

(d) The normal reflection of the optical axis plane was perpendicular to the subject plane of rotation.

46. If proper alignment were not made, data reduction from the films would be inaccurate or the data reduction analysis would be complicated by numerical compensations for misalignment - if these compensations could be made at all. To meet the requirements stated for proper alignment, the following methods and procedures for aligning the camera-mirror-subject system were used: A string, weighted at both ends, was strung horizontally across the chamber; crossing between the mirror and the subject. The end portions of this string passed through two eye bolts mounted opposite one another on the chamber wall and hung vertically. The eye bolts were positioned so that the horizontal string passed under the center of rotation of the rotor, and one leg of the vertically hung string passed over the center of the circular photo port. The weights at each end of the string held the section crossing the chamber taut and the vertical section plumb or normal to the horizontal plane (refer to plate 13).

47. The camera mounting surface was leveled (using a spirit level) and the camera was positioned so that its optical axis intersected the two vertically suspended strings. This was done by sighting through the camera focusing fixture and moving the camera until both strings appeared to coincide and passed through the center of a cross scribed on the camera focusing device.

48. The angle of the mirror was adjusted to make an angle of 45° with the horizontal plane by using the spirit level-angle arrangement shown in detail A on plate 13.

49. The mirror was then placed beneath the subject (and the string) and adjusted for angle as previously mentioned. When viewing through the camera focusing fixture and the photo port, the two vertical strings and the reflection of the horizontal stretched string appeared to coincide, then the camera-mirror-subject components were considered properly aligned. If the strings did not coincide, then the mirror was rotated until they did.

ANALYSIS OF RESULTS AND DISCUSSION.

Test Objectives and Data Compilation

50. Phase IV testing was designed to basically accomplish four objectives:

- a. Determine the fragment kinematics associated with a rotor burst.
- b. Investigate the major parameters affecting the basic interactions between fragments from failed high speed rotors and their casings or containment shrouds.
- c. Obtain an understanding of the behavior of certain materials, having an apparent potential for use in a lightweight containment/control system, under the attack of rotor fragments.
- d. Develop test equipment and techniques necessary to provide large quantities of quality data.

51. The results of AED's first 21 spin tests are qualitatively reported herein. A detailed compilation of these tests is presented in Appendix 3. This compilation is divided into four sections:

- a. Test objectives, photographic coverage, and burst speeds. (Plates 1, 2, and 3, Appendix 3).
- b. Fragment generator details (Plates 4, 5, and 6, Appendix 3).
- c. Containment system details (Plates 7, 8, and 9, Appendix 3).
- d. Photographic system details (Plates 10, 11, and 12, Appendix 3).

52. The following comments in this report are of a qualitative nature. A detailed quantitative examination of the high speed photographs is now in progress and will be reported in subsequent reports.

FRAGMENT TRAJECTORY AND MOTION

53. The initial portion of the AED program was to investigate the basic kinematics of fragments from failed rotors and their interactions with containment rings.

Flat Disk

54. A flat, uniformly thick, disk was modified to fail at 10,000 rpm and produce three annular sectors and a hub section. The failure occurred at 12,100 rpm and produced two annular sectors and one fragment composed of the third annular sector connected to the hub section. Pictures 2-1, 2-5, 2-9, and 2-13 of test No. 2 are shown on plate 14. There is a time interval of 200×10^{-6} seconds between each picture. The ring that the fragments are passing through is a photo triggering strip. It is made of a plastic film and presents negligible resistance to the fragments. The arrow in the pictures indicates the direction of disk rotation. Fragments A and B are seen to behave very much as illustrated on plate 15; i.e., the fragment rotates about its own center of mass as it travels along a tangential path.

ROTOR BLADES

Single Blade Failures

55. This complex fragment motion is also evident from examination of the pictures from test No. 10.

56. Plate 16 records the action of a blade from a turbine rotor of a "small" turboshaft engine as the blade interacts with a mild steel containment ring. Plate 8 shows the modified blade. The ring had a radial thickness of 0.125 inches. The length of the blade fragment was 3.5 inches from the blade tip to the area in the blade platform that was physically reduced to ensure failure at that location and at the pre-determined burst speed. The initial strike of the blade against the ring causes the electronic flash unit to operate. The rapid rise time of the flash unit permits the recording of almost the entire interaction. Picture 10-1 records the initial blade strike. The rotor was rotating counter-clockwise as is indicated by the arrows in the photograph. The blade struck with its tip attacking the ring at approximately the 10 o'clock position. Pictures 10-1 to 10-6 (plate 16) record the action of the blade as it continues to rotate in a CCW direction. Note that the area of the originally circular ring experiencing the impact is beginning to bulge.

57. The gross distortion of the 0.125 inch thick ring due to the impact of only the 0.08 pound blade is illustrated in the pictures on plate 17. The distortion at the 10 o'clock position causes that portion of the ring diametrically opposite the impact area to move inwardly and reduce the radial clearance between the blades remaining on the rotor and the containment ring. The ring distortion shown in picture 10-33 has taken place in approximately 2131×10^{-6} seconds. During this time, the rotor traveling at 21,200 rpm, has made slightly more than one revolution; the blade fragment has moved approximately 110° around the inner circumference of the ring. The blade fragment was apparently not struck by the blades that remained in the rotor.

58. Plate 18 shows blades numbered 2, 3, and 4 leaving the rotor and impacting the ring. Examination of the entire set of test No. 10 photographs indicates that blades 2, 3, and 4 rub against the inwardly displaced section of the ring (approximately 4 to 2 o'clock position) prior to blade failure. Pictures 10-35 and 10-38 show blades 3 and 4 rubbing the ring. It is suggested that this rubbing established a stress condition in the blades such that the last three blades all failed at the same position and struck the ring in a small concentrated area.

59. The post-test photograph of the containment ring of test No. 10 is shown in plate 19. The ring area that experienced the blade rubbing is shown on the right of the photo; the impacted area is on the left side. Plates 20 and 21 show, in detail, the total damage to the rubbed area and impacted area, respectively, of the ring.

60. A four-single blade burst, similar to test No. 10 was performed within a steel ring during test No. 7. High speed photographs were not obtained from test No. 7 and therefore it can only be assumed that the No. 7 blade failure was similar to No. 10. Plate 22 indicates the amount of total distortion experienced by the No. 7 containment ring. Comparing this post-test photograph with plate 19, a large difference in ring distortion can be seen. Two major parameters contributing to this difference are probably ring thickness and radial blade clearance. The ring from test No. 7 was twice as thick (0.250 inches vs. 0.125 inches) as the No. 10 ring; and the No. 7 test had a smaller radial clearance (0.475 inches vs. 0.6875 inches) than the No. 10 test.

Partially Full Rotor (Blade Hammering)

61. An important item that demands consideration when the containment/control of a rotor fragment, especially a blade, is studied, is the effect of the remaining portion of the rotor upon the released fragment as it tries to escape. Test No. 11 was designed to investigate this phenomena. A power turbine rotor from a "small" gas turbine engine (the same as tests numbered 7 and 10) was modified as shown in picture 11-0 of plate 23. Four blades were modified to fail just above the fir tree section at military speed. These blades were equally spaced around the disk. One unmodified blade was placed in front of (relative to the direction of rotation) the modified blade and two unmodified blades were fixed into the disk immediately behind the modified blade. The containment rings of test No. 10 and 11 were similar in material and size. The burst speed of the rotor of test No. 11 was 1450 rpm (21200 rpm vs. 19750 rpm) less than test No. 10 burst speed.

62. Unfortunately, there was an excessive time delay in the flashing of the electronic flash unit in test No. 11 and the film record was not initiated until all four blades had failed, interacted with the ring, and the ring had experienced a large amount of distortion. Picture 11-1 of plate 23 is the first picture of this series.

63. A post-test photograph of the containment ring from Test No. 11 is shown in plate 24. The area at the top of this photograph experienced the most damage. It is a very difficult task to determine what fragment caused what indentation or gouge mark. Plate 25 is a close-up of this damaged area. The direction of rotation is clockwise when viewing plate 25; i.e., the fragments moved from left to right. Many of the blades experienced a large amount of damage and it cannot be definitely determined whether they were damaged by their interaction with the containment ring or the spin chamber floor after the failure. What can be determined by matching fragment shapes to ring indentations is that gouge "A" on plate 25 was made by the section of the blade that had been reduced in the platform section; i.e., the blade was rotated around so as to strike with its base section. Impact area "B" was caused by the striking of the convex side of a blade against the ring. Impact area "C" was apparently caused by the impact of the flat side of the blade platform section.

64. The airfoil section of all the failed blades were bend over approximately 180° so as to form a "curled" tip.

65. Tests are scheduled at the AED to further investigate this "blade hammering" phenomena.

66. Test No. 16 was a three single-blade failure from a medium size jet engine turbine rotor. The high speed photographs were prematurely triggered (probably by a blade rub condition) prior to blade failure so no useful information was obtained from these pictures. A post-test examination of the fragments and ring did not produce any definite data.

EFFECT OF RADIAL CLEARANCE

67. A qualitative idea of the effects of radial clearance is obtained by comparing the action of tri-hub bursts in tests No. 4, 6, and 12. All three bursts produced the same type of annular sector fragments.

68. For test No. 4, the disk was 7.0 inches in diameter. This disk rotated inside a thin (0.0625 inch) steel containment ring having an inside diameter of 18.00 inches. This disk-ring combination provided a radial clearance of 5.5 inches. This relatively large clearance permits a great deal of fragment movement before ring interaction. Photograph 4-1 of plate 26 shows fragment A as it just leaves the disk. Photograph 4-9 (1504×10^{-6} seconds after photograph 4-1) shows the sharp outside diameter corner of fragment A about to make contact with the containment ring. Photograph 4-11 records fragment A rotating about one side (this side is not penetrating the containment ring). The other side of the fragment is speeding toward the ring. In photograph 4-13, fragment A pierces the ring with the second side, and fragment C, remaining attached to the hub section, is just about to strike the containment ring with a pointed section of the fragment. This corner of the fragment penetrates the containment ring as the hub section is rotated into and through the ring. In photograph 4-21, fragment A has almost completely perforated the ring while fragment C is approximately one-half the way through the ring. Note the ring is elongated at the points of impact and the ring sections between these impacted areas are displaced inwardly. Photographs 4-21 and 4-23 record the outside diameter edge of fragment B attacking the containment ring. Photograph 4-24 shows fragment B deeply imbedded in the ring. Fragment B did not penetrate the ring.

69. The damaged containment ring of test No. 4 is shown in plate 27. When you compare this photograph to picture 4-24, it is evident that a goodly portion of the ring damage was done after the fragments interacted with the ring; probably when the intentionally fragile containment ring supporting chains fell and allowed the ring to fall to the spin chamber floor. This type of information is a highlight of the effectiveness of the AED's high speed photographic system. Prior to this system, there would be no way of determining what portion of the action occurred at what time period.

70. Photographs 28, 29, and 30 detail the areas of the containment ring impacted by fragments A, B, and C, respectively.

71. Photograph 28 shows the opening in the ring produced by fragment A as it sheared a plug about 50% of the opening length and ripped through the remaining opening. The upper right corner of this photograph shows the inside portion of the ring contacted by fragment C. Note how the ring "folded" around the fragment.

72. The shape of the outside diameter edge of fragment C is easily recognizable in photograph 30.

73. The perforated ring area attacked by the large hub-sector fragment B is shown in picture 29. The strip of material sheared and then bent over is typical of the perforations of many of the metal rings.

74. For test No. 6, the disk was 7.00 inches in diameter and the steel containment ring had an inside diameter of 14.95 inches. This disk-ring combination established a radial clearance of approximately 4.0 inches. From photograph 6-2, plate 31, it is seen that all the annular sector fragments left the hub section within a very short time period and moved out toward the ring. Photograph 6-6 shows all three fragments having passed through the thin plastic photo-triggering system and fragments A and B striking the ring at the same instant. 184 microseconds later in photograph 6-7, it is seen that a section of the ring between fragments A and B has separated from the remainder of the ring. Fragment C has just made contact with the ring. Photograph 6-18 shows fragment A, in contact with the smaller ring section; bending this section into an "S" shape. Fragment B remains in contact with the larger ring segment, forcing it also into an "S" shape. The side edge of fragment C penetrated the containment ring. Note that all three fragments are continuing to rotate as they continue to move outwardly. Photograph 6-24 records the maximum penetration of fragment C into the ring. Post-test investigations (plate 32) revealed that fragment C remained wedged in the ring. Plate 33 shows the area of the containment ring struck by fragment C. A plug of metal is sheared from the ring very similar to the action of a punch-press.

75. Unlike tests No. 4 and 6, which had relatively large radial clearances, test No. 12 was conducted with a comparatively "tight" (0.4375 inches) radial clearance. Plate 34 is a drawing of the containment ring used for test No. 12. This ring is shown prior to tests in plate 35. A typical strain gage installation can be seen. The leads and electrical connectors from the four strain gages are noticeable in the upper right corner of the photograph. The white compound on the leads is a sealant used to support the strain gage leads and prevent them from coming off the terminal strip. The thin center section was designed to be marginal relative to containment capability. The heavier flange sections were necessary to properly manufacture and position the ring.

76. The first photograph of the action sequence (photograph 12-1), plate 36, shows the fragments A and B have both left the hub section and have contacted the containment ring with their outside diameter edge. Fragment C is still attached to the hub section and has not contacted the ring.

77. Probably the most important effect of radial clearance between disk and ring now becomes evident. Unlike tests No. 4 and 6 where the large clearances permit a multitude of possible initial fragment impact orientations, a close clearance of test No. 12 restricts the initial impact orientation. In this particular disk-ring combination, only the outside diameter edge of the fragment can make initial contact.

78. In photograph 12-9, all three fragments are attacking the ring forcing it from its original circular shape, into a triangular shape.

79. In 1560×10^{-6} seconds, fragment C first breaks away from the hub section. This is shown in photograph 12-21. In this photograph it can be seen that fragment A has rotated from its initial position in photograph 12-1 (approximately 11 o'clock) to a 1 o'clock position, and fragment B has moved from 7 o'clock to 9 o'clock. The triangular shaped ring of photograph 12-9 is now seen to be more elliptical than triangular.

80. A comparison of the location of one of the ring index marks in photograph 12-1 with its location in photograph 12-21 indicates a point of interest. Although the freely supported ring has undergone a large amount of deformation in the time period (1560×10^{-6} seconds) the ring has only been rotated approximately 3° by the impacting fragments.

81. Photograph 12-33 shows that fragment A has moved into a position where it is now moving toward the containment ring with a pointed corner. Prior to this moment, the fragments were sliding around the inside of the ring with their smooth outer diameter edges.

82. Fragment A has just penetrated the ring in photograph 12-43; i.e., the containment ring was not perforated until approximately 3276×10^{-6} seconds after the disk burst. At this instant, the containment ring has only rotated approximately 18° . Photograph 12-57 shows fragment A penetrating into the ring. Note that the fragment is continuing to rotate about its center of mass as it penetrates. In 6708×10^{-6} seconds (photograph 12-87), fragment A has completely penetrated the ring. Fragments B and C are still rotating within the ring.

83. Photograph 12-125, the last photograph of this action sequence, shows that fragments B and C are still inside the containment ring after 9672×10^{-6} seconds.

84. A post-test photograph (plate 37) of the underside of the containment ring shows the final ring distortion. Plate 38 shows the opening through which fragment A passed. The large amount of plastic working of the thin center as it was forced outward by the fragments is apparent in this photograph. The two "ring index" marks can also be seen. Plate 39 views the ring from another direction. Again, it can be seen that the center section experienced gross deformation over the entire section.

STRESS CONCENTRATION EFFECTS

85. An interesting aspect of test No. 6 was the affect of stress concentrations on the behavior of impacted containment rings. Plate 40 shows the 0.010 scribe marks placed on the outer surface of the ring. This grid system was established to assist in the determination of plastic deformation of the ring. A post-test photograph of the containment ring is shown in plate 32. The fracture of the ring in the areas struck by fragments A and B occurred along the longitudinal grid marks (plates 41 and 42, respectively). The partial cracking in the larger segment of the containment ring (plate 43) occurred parallel to one of the longitudinal scribe marks.

86. In comparison to this action we can look at a similar test (No. 5), that unfortunately, did not produce high speed photographs. The following comments are therefore based only on post-test investigations.

87. A similar tri-hub burst was produced at a slightly higher speed than test No. 6 (13800 rpm vs. 12750 rpm). The containment ring for test No. 5 was 0.024 inches (0.252 vs. 0.228) thicker than the ring for test No. 6. The three annular sector fragments from test No. 5 apparently struck the ring simultaneously and at points equidistant around the inner circumference (plate 44). Two of the fragments left imprints in the ring but did not crack or penetrate the ring. The third fragment partially sheared a plug from the ring. Plate 45 details this plugged section still attached to the ring. This plugging action is very similar to that produced by fragment C of test No. 6.

88. Due to the very different results of what could be considered fairly similar tests, one must consider the effects that intentional or unintentional stress raisers, such as ring stampings, holding mechanisms (holes, clamps, etc.), could have on the final behavior of a containment ring. This particular area is scheduled for additional investigation by the AED.

Starter Rotor Tri-Hub Burst

89. The objective of test No. 20 was to investigate the behavior of a steel ring having the same inside diameter, axial length, and weight as the Energy Absorbent Resin ring of test No. 8. The ring was to be attacked by a tri-hub burst of a starter rotor. Plate 46 shows the modified starter rotor and containment ring in position beneath the spin chamber center cover assembly.

90. The quality of the high speed photographs was not sharp enough to reproduce in this report but certain qualitative data was obtained. The first photograph of the high speed sequence indicated that all fragments had separated from the hub and interacted with the ring. The ring in this photograph has a triangular shape. One of the fragments ricocheted out of the plane of rotation and ended its interaction with the ring at 950×10^{-6} seconds after the first picture. A second fragment ended its contact with the ring at approximately 1710×10^{-6} seconds. The last fragment rebounded out of the ring at 3040×10^{-6} seconds after the first picture.

91. The post-test photograph of the containment ring of test No. 20 (plate 47) is very similar to that of the No. 5 test ring. Plate 48 records one of the three areas of the inside of ring No. 20 showing the indentation of the bladed edge of the rotor fragment. This marking indicates the fragments remained in one area relative to the ring distortion.

92. This triangular shape of containment rings that have experienced deliberate tri-hub bursts during containment tests is very common. It is suggested that, although the tri-hub produces a fragment possessing the maximum translational kinetic energy per fragment, this type of rotor failure may not necessarily be the most critical type to impose upon all types of turbomachinery. The fact that the fragments from a tri-hub burst tend to distort the ring evenly may be less hazardous than a burst that produces a different distribution of fragments, such as a single pie-shaped fragment from a rotor.

93. AED has no definite recommendations concerning the type of test that should be required for various turbomachines to satisfy the containment section of appropriate specifications, but we do suggest that these specifications be re-evaluated in light of the data produced by the Rotor Burst Protection program.

MATERIAL EVALUATION

94. In addition to the study of fragment-containment/control system interactions, AED effort includes a sub-program to investigate the potential of various materials that either intuitively, or because of their performance in other fields, such as lightweight armor, shock absorption, etc., look promising. Only three materials were investigated during this phase. Many more materials, and combinations of materials, will be investigated during subsequent tests.

95. Test No. 17 provided an interesting insight into the possible used of "Doron" and "Alumina", aluminum oxide (Al_2O_3).

96. Doron is fabricated from various plies of unidirectional Fiberglas fabric (made to Military Specification MIL-F-9084, Glass Fabric, Unidirectional) which are laid up with alternate plies oriented 90° to each other and bonded together, usually with a general-purpose polyester thermal setting resin purchased under Military Specification MIL-R-7575 entitled "Resin, Polyester, Low-Pressure Laminating", reference 5 (Ballistic Technology of Lightweight Armor Materials by Francis S. Mascianica, U. S. Army Materials Research Agency, Watertown, Mass., September 1964, AMRA MS 6407). The Doron plates, curved, 5 inches x 5 inches x 1/2 inch, weighing approximately 0.876 lb/plate, used in test No. 17, were provided to the AED by the U.S. Army Natick Laboratory, Natick, Mass. These curved panels were originally designed for use as fighting armor inserts.

97. The Alumina tiles, 5 inches x 5 inches x 1/2 inch, weighing approximately 1.67 lb/tile were supplied to the AED by the Naval Research Laboratory, Washington, D. C. Investigation of the capabilities of ceramic materials, such as aluminum oxide (Al_2O_3), in the field of ballistic protective armor, has indicated that they hold considerable promise for this application when combined as a layer-type composite with other materials.

98. Plate 49 shows the Doron-Alumina composite "ring" used for test No. 17. The Doron and Alumina tiles were placed within a thin (0.125 inches) aluminum casing. The casing was designed to properly position the tiles relative to the trajectory of the fragments and not necessarily to provide protection.

99. The quality of the high speed photographs of test No. 17 was only fair and the number of usable prints was limited. Photograph 17-0 of plate 50 shows the bladed gas generator rotor, modified to fail in a tri-hub burst, inside the containment "ring" prior to the test. Photographs 17-2, 17-3, 17-4, and 17-5 of plate 50 record the reaction of the fragments as they interact with the Doron-Alumina tiles.

100. In photograph 17-2, the trailing blades of fragment A strike the center of an Alumina tile. The blades were made from a nickel based steel similar to most turbine rotor materials. The blade is approximately 2.3 inches long; the airfoil section being approximately 1.8 inches. Approximately 1/2 of the blades on fragment A (the leading blades) have not touched the tile. In pictures 17-3 and 17-5, the trailing corner of the disk portion of fragment A is seen to be approaching the tile, indicating the trailing edge blades are being deformed and/or sheared from the disk. The post-test of fragment A, plate 51, shows the first six blades of the trailing edge have been sheared off while the remainder have been grossly deformed. The fragment leading edge blades are bent in the opposite direction, probably due to the secondary impact of the fragment.

101. Fragment B makes its initial contact with a Doron panel in picture 17-3. All but the five leading blades are making contact. The post-test photograph of fragment B (plate 51) shows that all but three blades (near the trailing edge) have been sheared off just above the fir tree section. A determination of when this damage occurred cannot be made.

102. It isn't until picture 17-4 of plate 50 that fragment C, attached to the hub section, contacts a Doron panel. Picture 17-5 shows that only about 1/3 of the blades (at the trailing edge) are in slight contact with the Doron. Post-test photograph of fragment C indicates a small amount of damage was done to all but the four trailing blades. Three of the blades were forced out of the disk during the test and are shown beside fragment C.

103. The aluminum supporting "ring" did not begin to separate until 580×10^{-6} seconds (picture 17-9) after the first picture was taken. The curved portion of the aluminum "ring" apparently failed in picture No. 17-11 (725×10^{-6} seconds). The Alumina tile support was still intact at the last discernible photograph, picture 17-15 (1015×10^{-6} seconds) after the first picture.

104. The very hard surface of the Alumina tile produced very advantageous effects relative to containment/control:

a. The sharp edges of the blades and fragments are removed either by abrasion, bending or curling fragment edges. This dulling of the fragment cutting edges is especially important when these hard face materials are used to front composite designs using softer back-up materials (metal, plastic, or fibers) that are susceptible to cutting or slicing.

b. The shattering of the hard surface distributed the fragment load over a greater area of the backing material, thereby, reducing the impact stress.

c. Much of the fragment's energy is dissipated in causing the deformation of rotor fragments.

105. Plate 52 pictures two Doron inserts and the fragments of an Alumina tile after test No. 17. The ripping across the center of the inserts is in the plane of rotor rotation. It cannot be determined if the damage to the Alumina tile was caused by the fragment impact or by the fall to the spin chamber floor. The tape on the inserts and tile is part of the photo-triggering system.

106. Plate 53 shows two Doron inserts from test No. 17 and a new insert. Note the extreme delamination of the two impacted inserts. Fragment energy is dissipated by the Doron as it experiences inter-laminar shear.

107. Previous limited attempts by others to use reinforced plastics, similar to Doron, in spin tests, reported that the metal fragments shredded the material and then penetrated the ring. Containment of similar rotor failures in spin tests, were achieved by placing a steel ring inside the reinforced plastic ring. Apparently the hard inner steel ring removed the sharp edges from the fragments and helped to distribute the impact load.

108. Future AED testing will include various combinations of containment/control systems utilizing various ceramics and reinforced plastics.

109. Test No. 17 was originally attempted as test No. 9 which was unsuccessful when the rotor to drive spindle retaining mechanism failed and allowed the rotor to fall to the spin chamber floor. No contact was made between the rotor and the containment device.

110. Another material tested for its possible use as a containment/control material was an Energy Absorbent Resin (EAR). This material reportedly has a high internal friction characteristic.

111. For test No. 8, a typical starter axial turbine rotor was made to fail in a tri-hub burst into a ring made of EAR. High speed photographs were not obtained from this test. A post-test examination showed the EAR ring was fragmented into many small pieces; the largest being approximately one-third of the ring. It was suspected that a large amount of fragment energy could be absorbed by the fragmentation of the ring material if the material and fragments had remained in contact with one another for a longer period of time. It was this suspicion that led AED to wrap a nylon cloth around the outer circumference of a second EAR ring (test No. 19). The nylon used was from a sample (provided by the U.S. Army Natick Laboratory, Natick, Mass.) of cloth, nylon, ballistic, 2 x 2, basketweave, 13.5 oz. min., 15 oz. max., square yard.

112. A drive shaft failure during the acceleration of the starter rotor fragment generator during test No. 19 prevented an evaluation of the nylon wrapped, EAR ring. Test No. 19 will be repeated.

FRAGMENT SHAPE EFFECTS

113. A series of tests was conducted to investigate the effects of fragment size on the containment of fragments from bursting rotors. Definite conclusion cannot be made concerning the results of these tests due to the limited number of tests conducted, but certain insights can be gained.

114. This series was composed of tests No. 12, 13, 14, 15, and 21 (a repeat of test No. 14). Details concerning these tests, including fragment kinetic energies, are presented in plate 54. All tests used the same type of ring as described in plates 34 and 35.

115. The results of test No. 12 were presented in the "Effects of Radial Clearance" section of this report. Each fragment theoretically possessed 32.3% of the total kinetic energy of the rotor, 21.1% being the translational component and 11.2% being the rotational component. One of these fragments from test No. 12, weighing 1.178 pounds, did penetrate the containment ring.

116. For test No. 13, a bi-hub burst was produced. Each fragment weighed 0.59 pounds (1.768-1.178) more than a fragment of test No. 12. Unlike test No. 12, the individual fragments of test No. 13 had as its major kinetic energy component its rotational component (30.8% of the total rotor energy) as compared to its translational component (18.7%). A review of the high speed photographs of test No. 13, plate 55, shows the gross deformation of the ring but indicates that neither of the fragments penetrated the ring. This hints that fragment mass is not necessarily the dominant factor when studying containment. Fragment total kinetic energy cannot be directly applied as a containment design parameter either since the individual fragments of test No. 13, that were contained, possessed more than twice the total kinetic energy (39536 in.-lb) vs. 16237 in.-lb) as an individual fragment of test No. 12 which was not contained.

117. The once circular ring (picture 13-0, plate 55) has been grossly elongated along an X-axis in 584×10^{-6} seconds after the first picture (picture 13-9). The two fragments continue to distort the ring until it is elongated along a Y-axis (picture 13-49). This elongation is attributed to the working of the ring material and not to the rotation of the ring. The fact that the ring has rotated only slightly can be seen by noting that the "ring index mark" (circled on plate 55) has moved only a small amount in the clockwise direction. In the later pictures of this test (pictures 13-73 to 13-137) the disk fragments continue to reshape the ring. This reshaping has the effect of reducing the amount of out-of-roundness noted in the earlier pictures and the ring is also rotating more. One reason for the increased rotation of the ring is the impact of the hub section into the ring

(picture 13-87). In pictures 13-113 and 13-137 it is seen that fragment "a" is moving toward the chamber lid and out of the plane of rotation. Fragment "b" remained in the plane of rotation for the duration of the high speed photographs.

118. Plate 56 shows the post-test photograph of the test No. 13 containment ring. Post-test examinations revealed that this ring experienced the greatest permanent elongation of all similar rings. Plate 57 details the damage done to the thin center section of the ring. The opening at the bottom of the photograph was caused by the hub impact. This opening, that extended approximately one-third of the way around the ring, was caused by a rip in the section and a bending outward of the material. The opening was not large enough for a fragment to pass through. The damage at the top of the photograph was caused by two small circumferential rips in the center section. No material was missing from the entire ring.

119. The large deformation experienced by the containment ring of test No. 13 is interesting to note, not only because the ring design and material must be capable of undergoing such large plastic deformation without failing, but also since, if this ring had been constrained in some manner rather than freely supported as it was, the restraining or supporting system would have to be so constructed to either permit this varied movement without failing at the connecting point or strong enough to restrict the movement of the ring. If the ring movement is restricted, the stress distribution in the ring will be changed.

120. Some manufacturers of jet engine starters design their axial turbine rotors to fail at a reduced section of the disk. This reduced section is located just below (radially inward) the blade holding section of the rotor and extends completely around the rotor. At some speed greater than normal operating speed, the rotor fails, releasing the rim section and thereby limiting the speed of the larger hub section, since the driving blades are now removed, and secondly causing a smaller fragment to attack the ring.

121. Test No. 15 was conducted to investigate this type of action. Some of the high speed photographs of test No. 15 are presented on plate 58. Picture 15-1 shows the initial contact of fragment "a" with the ring. In 608×10^{-6} seconds after the first picture, the disk, with two of the annular rim sectors still connected to the disk, makes contact with the ring. In picture 15-15 (1064×10^{-6} seconds after the first picture), the ring experienced its largest elongation (along a 45° axis). A review of pictures 15-19 to 15-99 indicates the complex action that is possible in a spin chamber test where there are no axial restraints and the fragments may be deflected out of the plane of rotation and entirely away from the containment

device. Spin testing using actual components such as housings, exhaust ducting, stator or guide vanes, etc., increase the complexity of ring-fragment interaction since the fragments cannot move axially but are redirected into the ring for secondary strikes. The evaluation of containment tests using all or part of actual hardware are therefore very difficult to analyze without the use of high speed photographic techniques. Such techniques require that certain test compromises be made between the use and location of actual hardware and photographic viewability.

122. Plates 59 and 60 show the containment ring after test No. 15. Plate 59 indicates the final out-of-roundness of the ring. Similar to the action noted in test No. 13, the final distortion was not as elongated as shown by the high speed pictures (picture 15-15 for example). The total action of all the fragments restore the ring, to a certain degree, to its original circular shape. Plate 60 details the distortion of the thin center section of the ring. The deepest indentation (bottom of the photograph) was probably caused by the impact of the hub and remaining two fragments as recorded in pictures 15-9 to 15-27.

123. The high speed photographs of test No. 21, a quad-hub burst, are presented in plate 61. The radius ratio (hub radius divided by disk radius) for test No. 21 was the same as tests No. 12 and 13. Plate 7 shows the type of disk used for tests No. 21 and 14. Test No. 21 was a repeat of No. 14 because we did not obtain high speed photographs of test No. 14.

124. Picture 21-3 of plate 61 shows that in 196×10^{-6} seconds after the first picture all four fragments had contacted the ring. The equally spaced radial force loading is apparent in picture 21-19. In picture 21-33, fragment "a" is starting to penetrate the ring as fragment "d" slips alongside (below in the photo) fragment "a". Picture 21-43 and 21-57 record fragment "a" as it passes through the ring. Fragments "c" and "d" have left the ring in picture 21-95 and fragment "a" is now completely through the ring.

125. The opening in the test No. 21 ring, caused by fragment "a", is shown in plate 62. It is interesting to note the serrated edges of the opening where the fragment caused a cutting action, similar to a can opener, as it penetrated the ring and folded back the thin ring material. This same type of serration was noted on the post-test examination of the test ring from test No. 14. The two openings in this ring are detailed in plates 63 and 64. Both openings are large enough to permit the passage of the fragments of test No. 14. The edge of opening "B" (top of plate 63) was serrated. Marks on the outside of the torn metal strip of opening "A", plate 64, indicate it was bent back over the opening when the ring struck the spin chamber floor after the test. The edge of opening "A" was relatively smooth as if sheared in a press.

REFERENCES

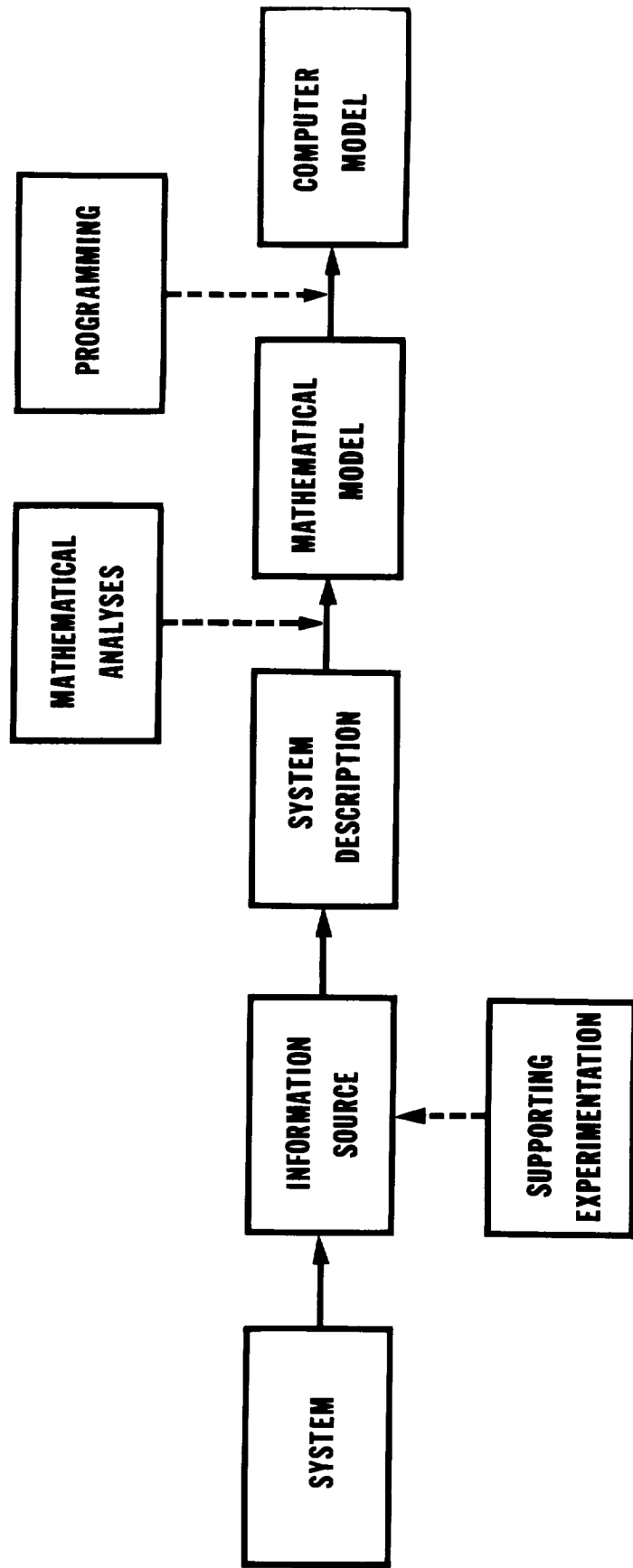
126. Reference material noted in this report is as follows;

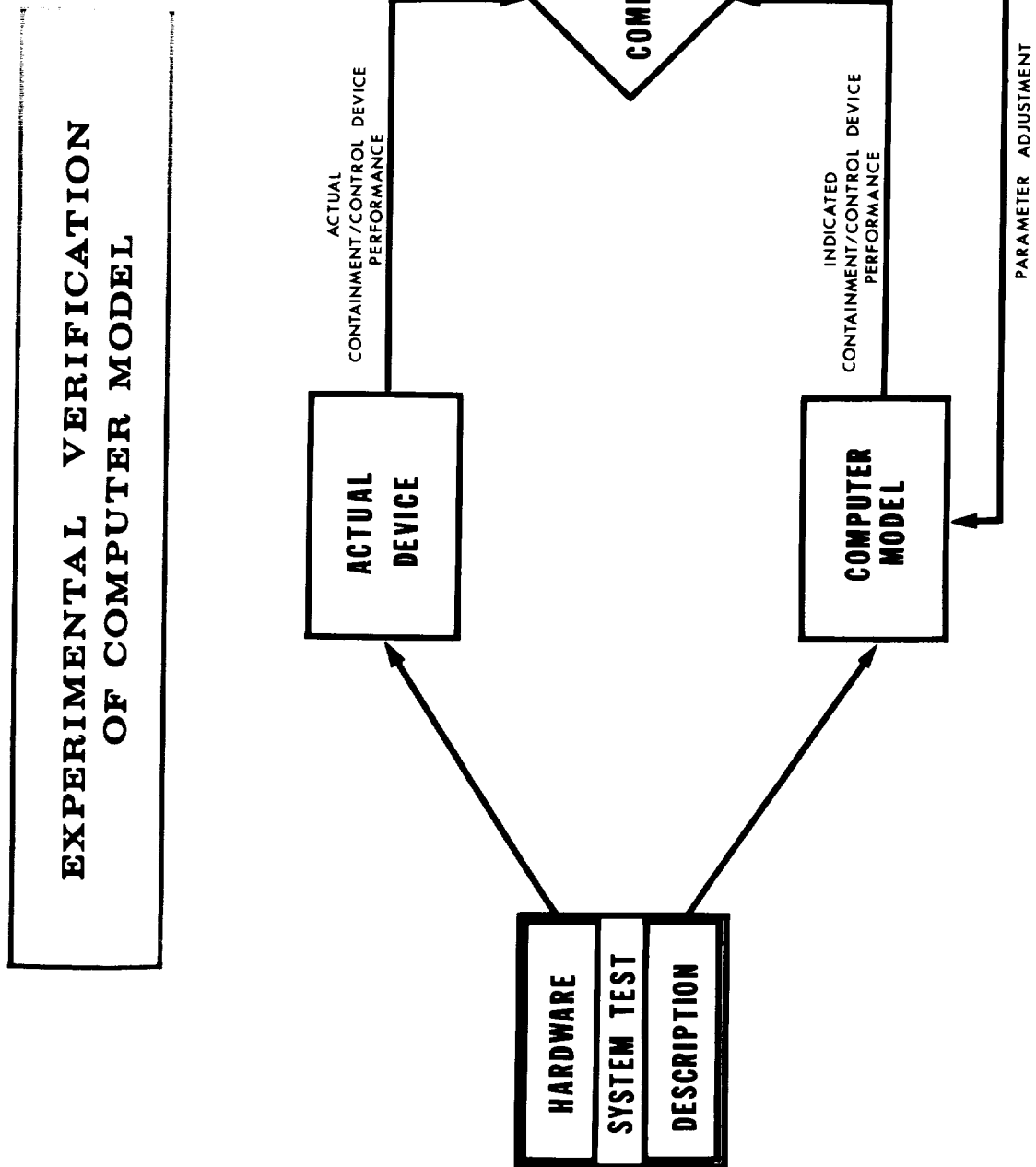
- a. NASA Defense Purchase Request R-105, Amendment No. 3, dated 10 August 1966.
- b. Martino, A. A. and Mangano, G. J., "Turbine Disk Burst Protection Study - Final Phase II-III Report on Problem Assignment NASA DPR R-105", NAEC-AEL Report No. 1848, 28 February 1967.
- c. Martino, A. A. and Mangano G. J., Aeronautical Engine Laboratory, NAEC, Phila., Penna., "AELCEF - A Tool to Make Rotor Burst Containment a Reality," SAE Paper No. 670332, April 25, 1967.
- d. Steck, E. L., Frost Engineering Development Corp., Englewood, Calif. "A Review of Restraint Systems Test Methods," ASME 63-WA-279, Nov. 1963.
- e. Mascianica, Francis S., "Ballistic Technology of Lightweight Armor Materials (U)," AMRA MS 64-07, September 1964, U.S. Army Materials Research Agency.
- f. Kodak Data Release for 2475 Recording Film, Kodak Publication No. P-95.
- g. Kodak Data Release for 2485 High Speed Recording Film, Kodak Publication No. P-94.

ACKNOWLEDGEMENT

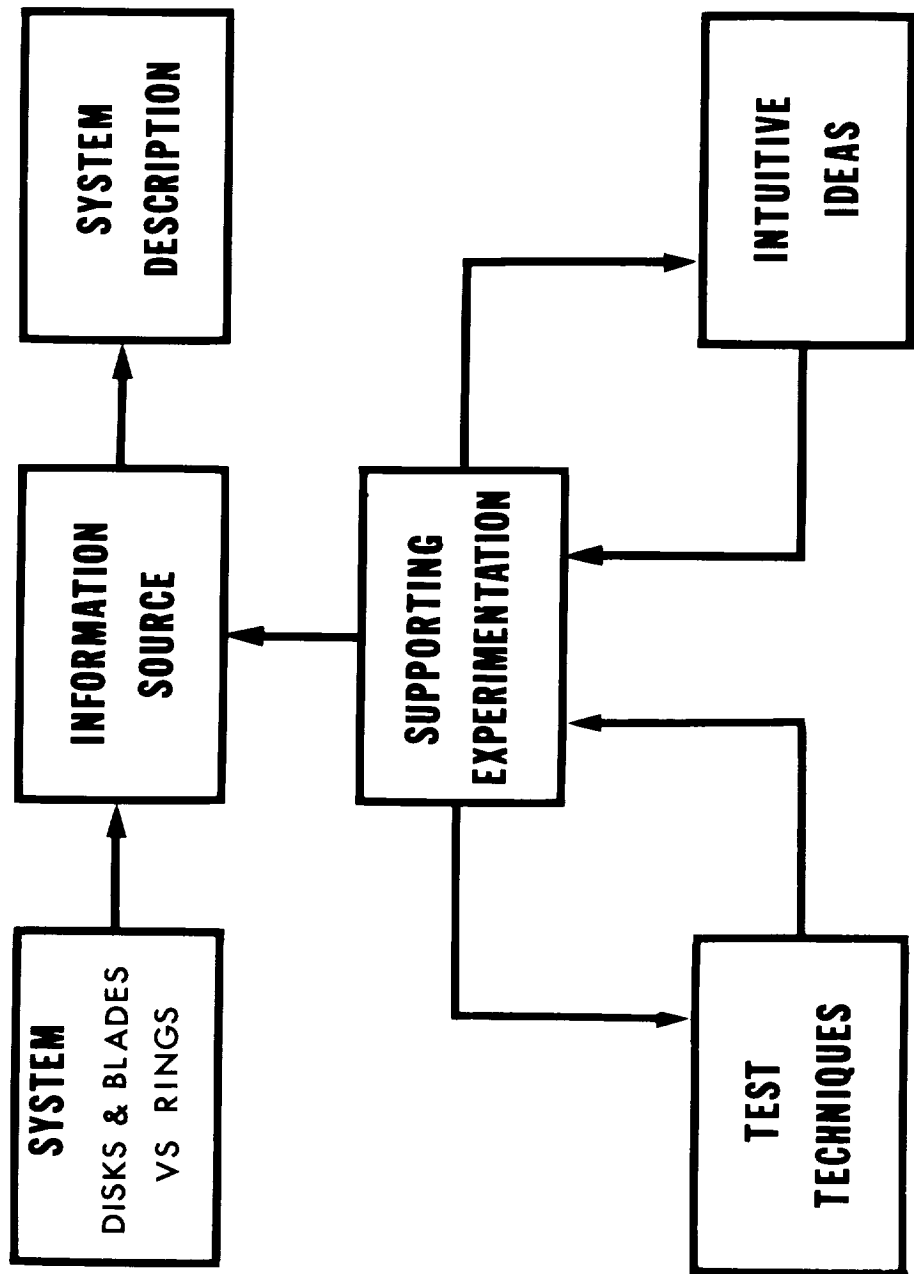
The authors wish to express their appreciation to the many industrial and government organizations who have actively participated in the Rotor Burst Protection program. The continuation of these interchanges is essential to the attainment of the program's goals.

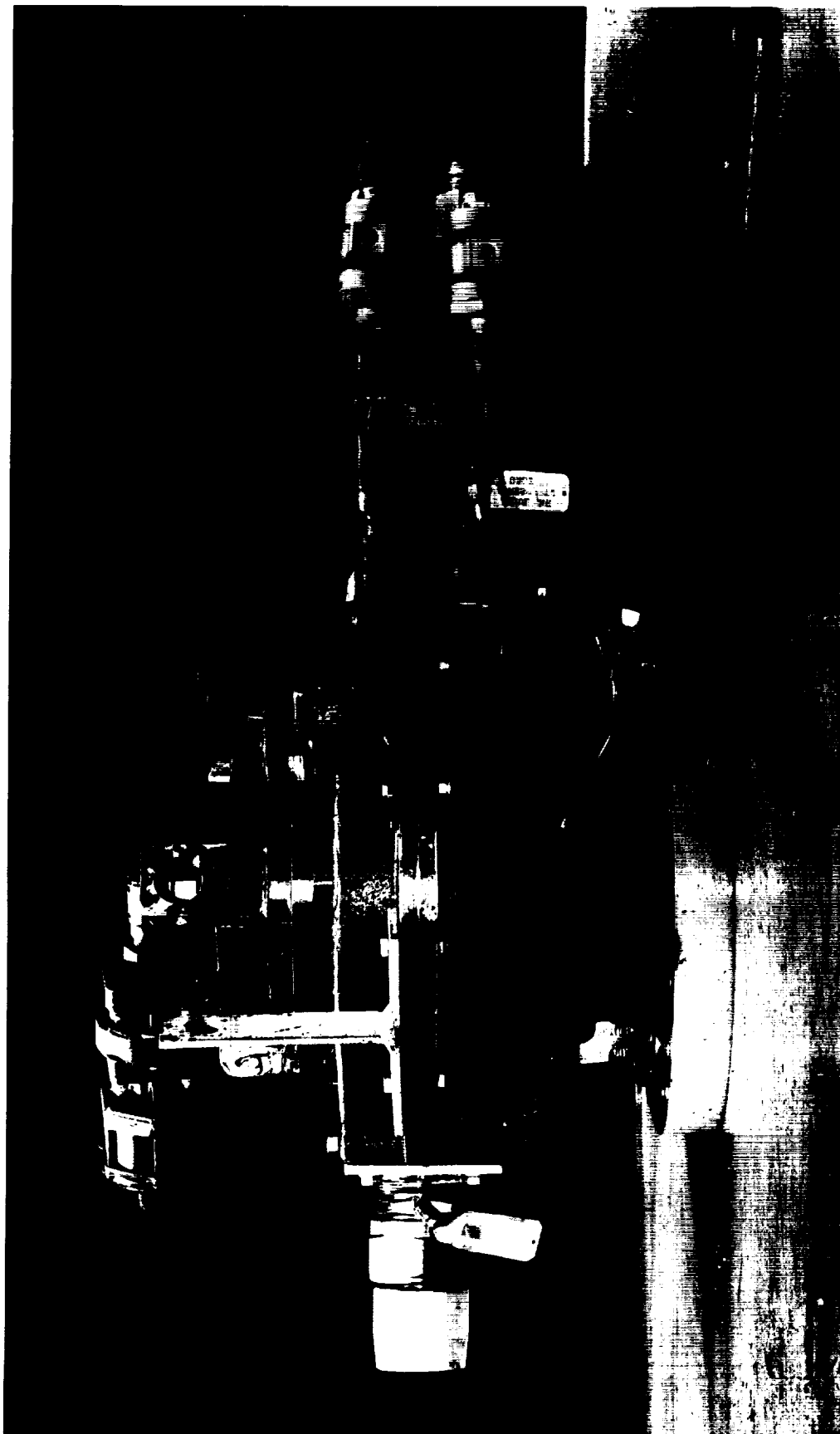
**Development of a
TURBOMACHINE CONTAINMENT/CONTROL SYSTEM
MATHEMATICAL MODEL**





PRESENT STAGE OF INVESTIGATION



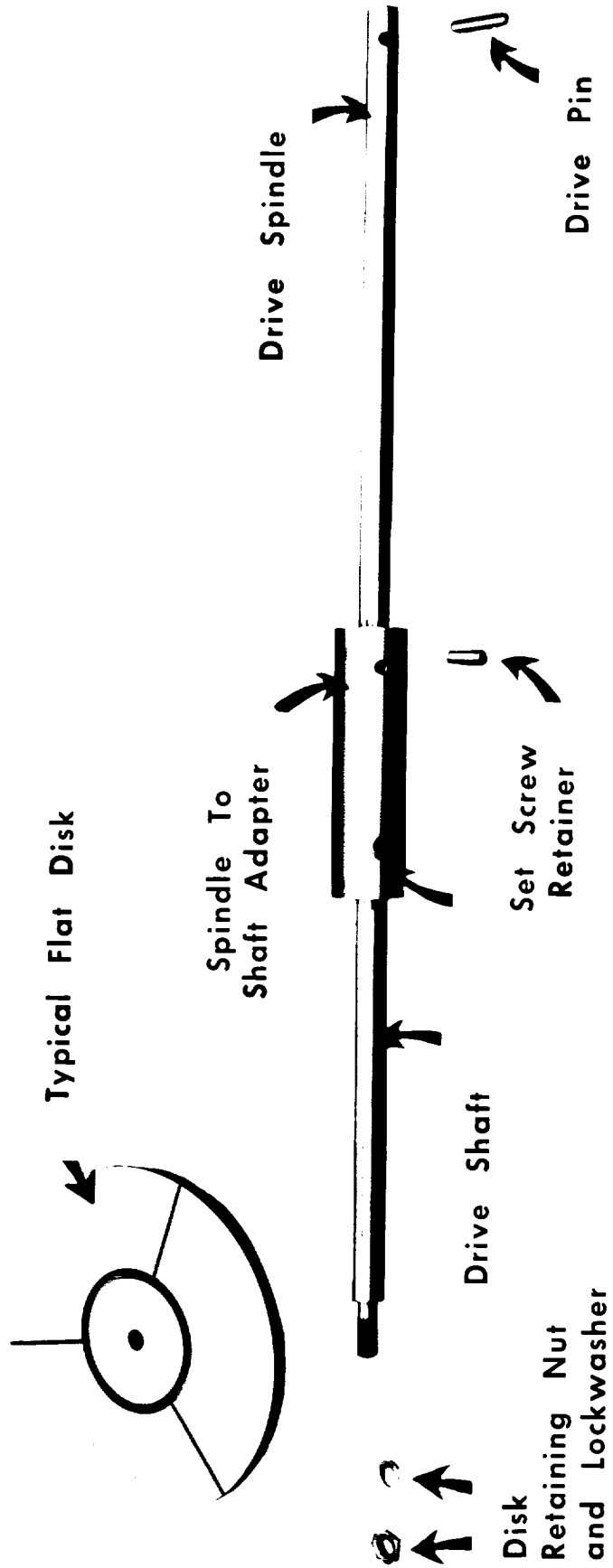


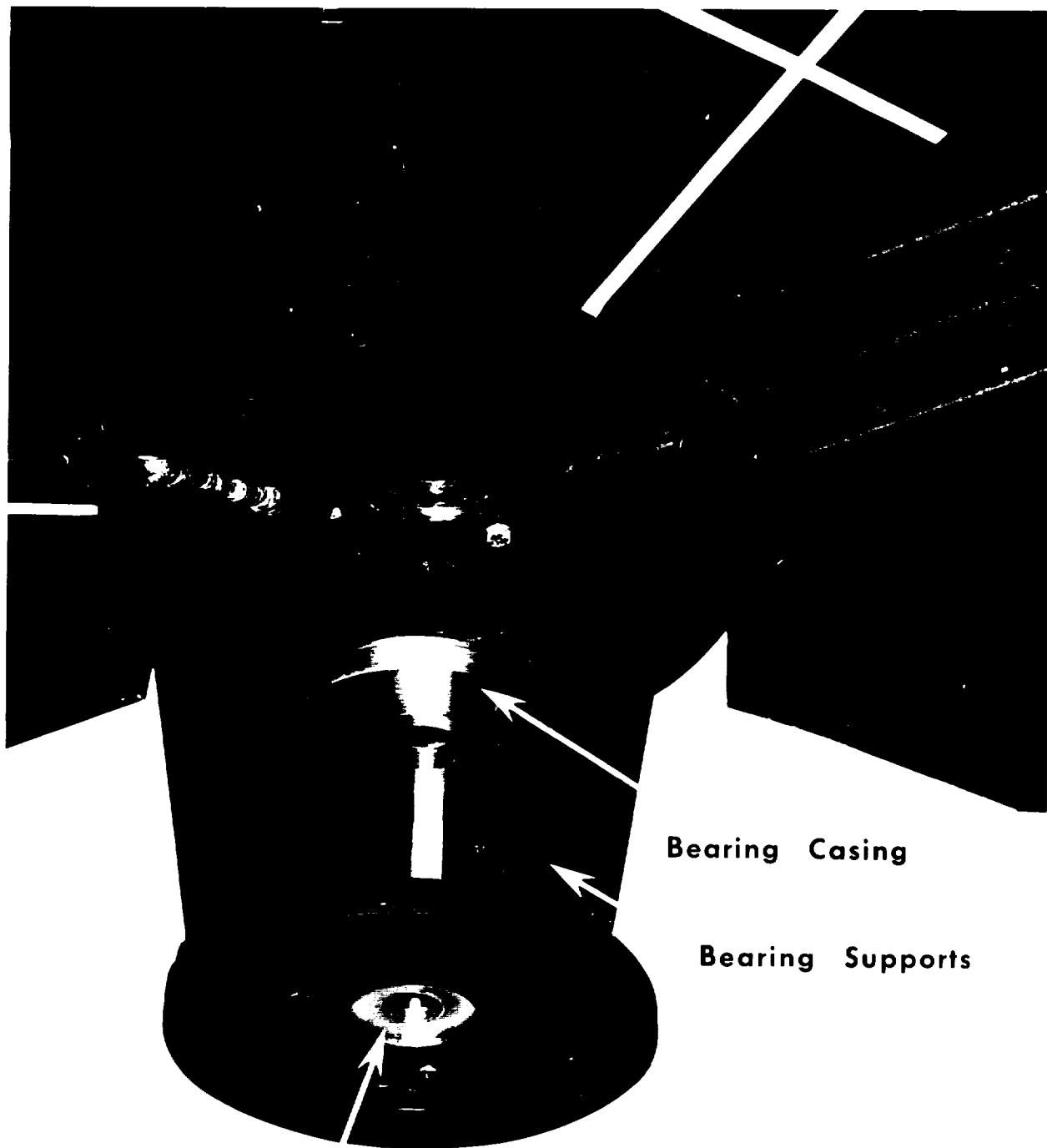
AIR POWERED EIGHT INCH DRIVE TURBINE

PHOTO NO: CAN-385996(L)-1-68

PLATE 4

DRIVE SPINDLE AND SHAFT ASSEMBLY FOR 8" DRIVE TURBINE

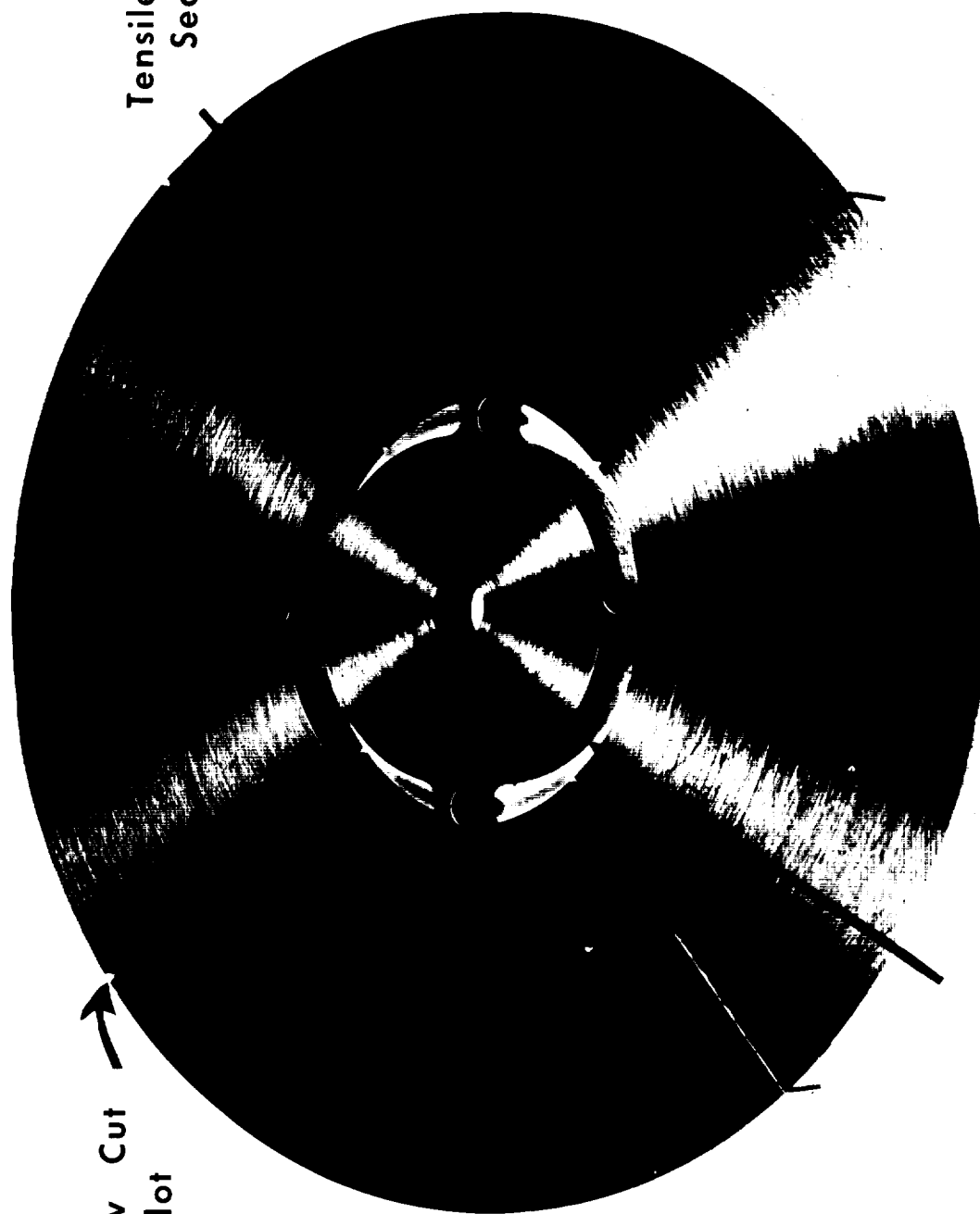




Lower Bearing

TURBINE DRIVE SHAFT ARRESTER

MODIFIED FLAT DISK
4 SECTOR FRAGMENT GENERATOR



Saw Cut Slot

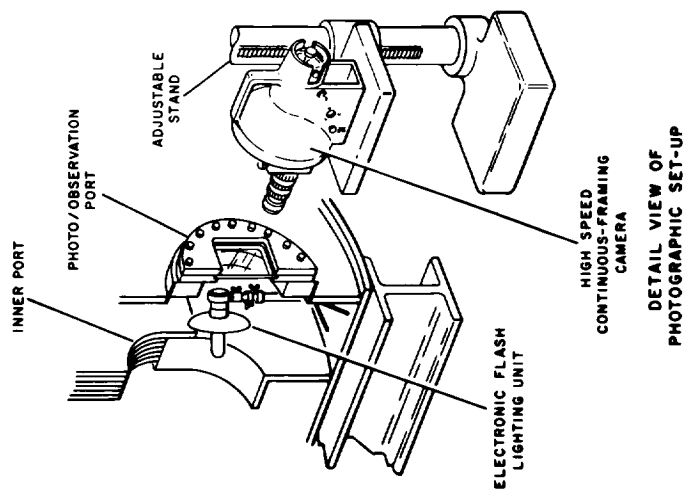
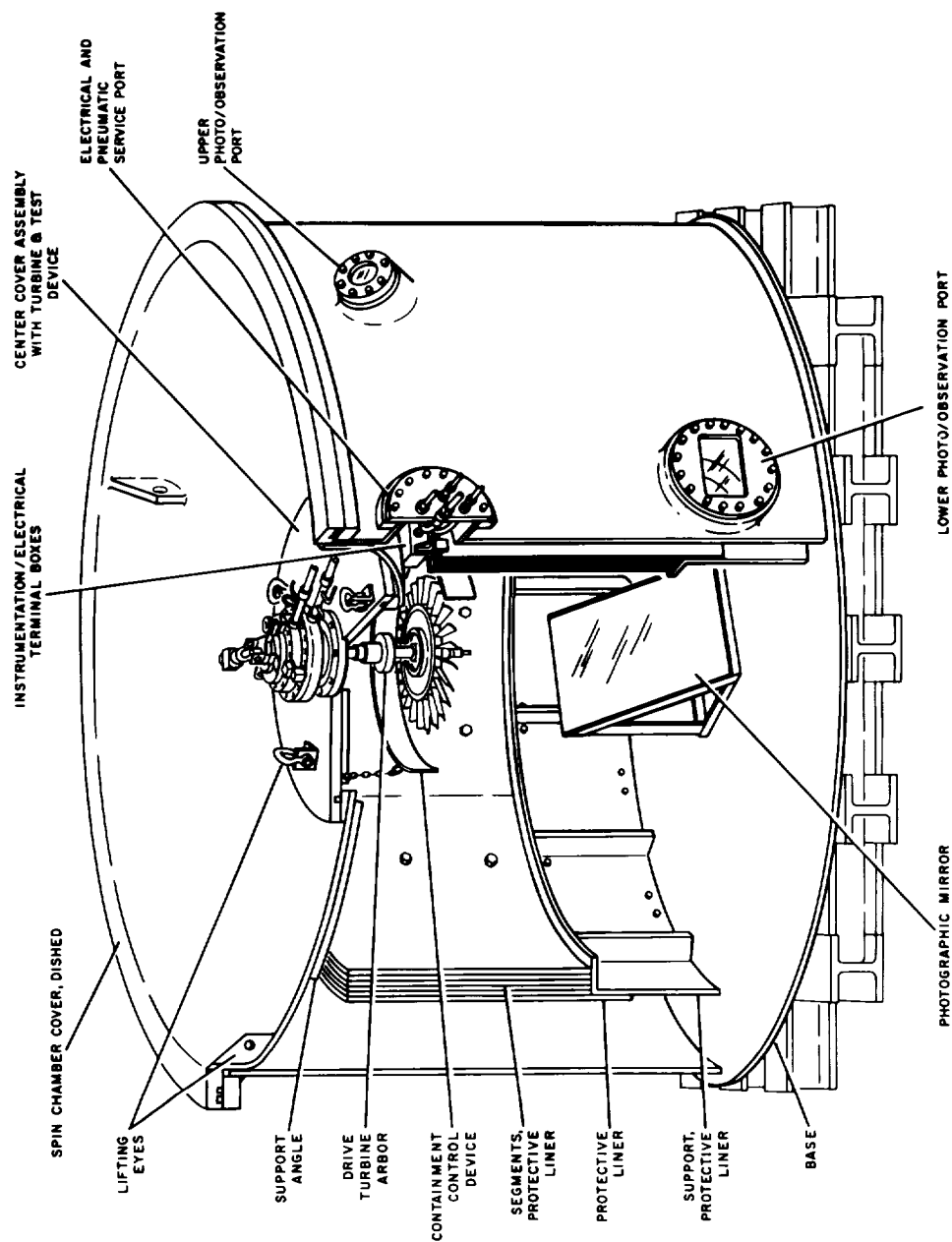
Tensile Release Section

Milled Slot

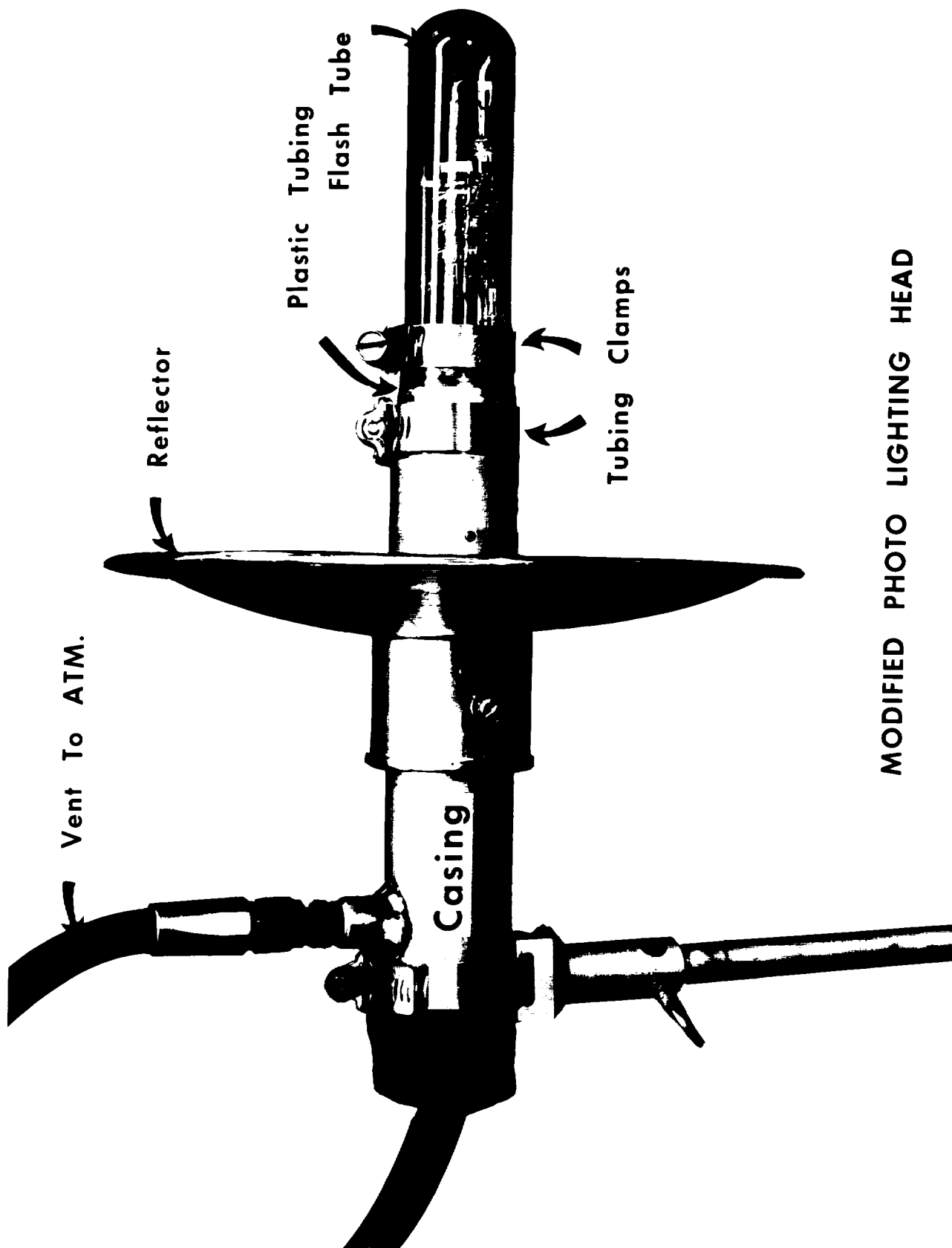


Failure Section

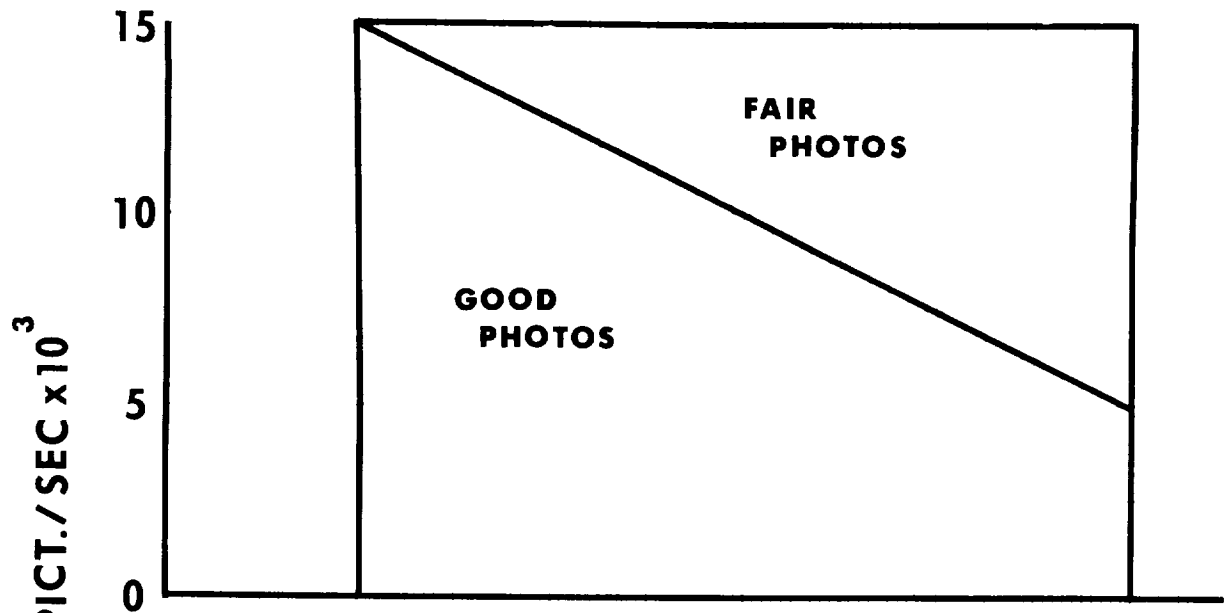
MODIFIED TURBINE BLADE



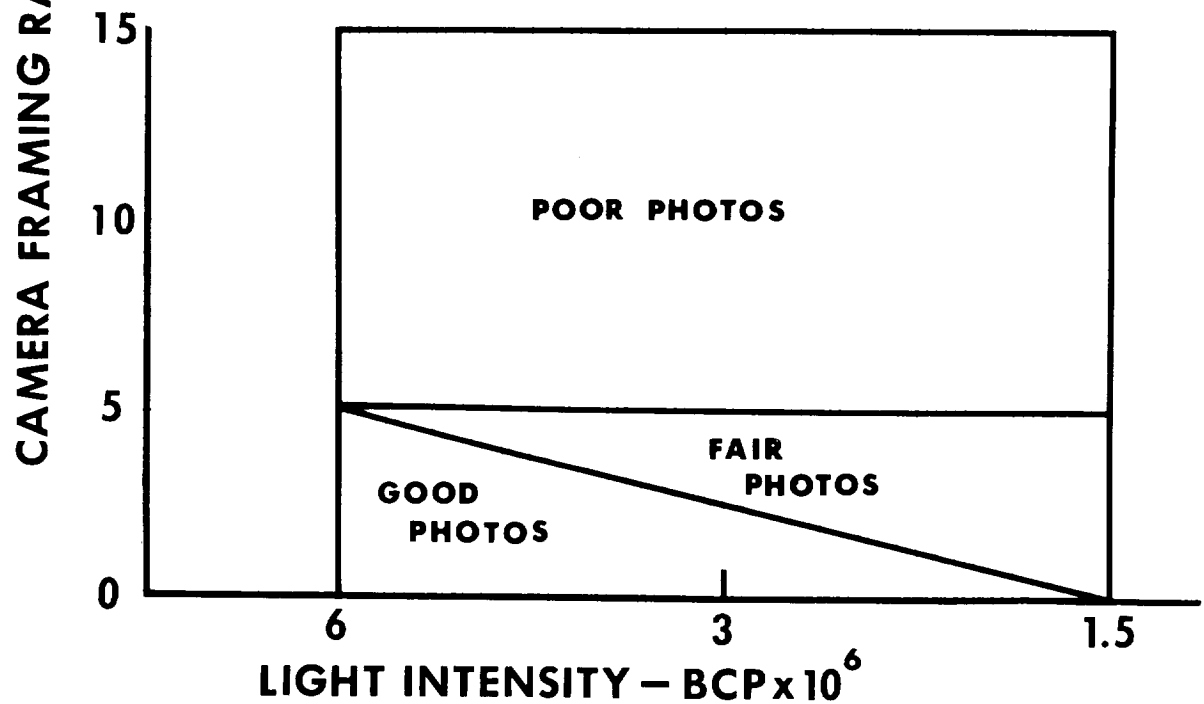
CUTAWAY ASSEMBLY-AEDCEF-SPIN CHAMBER NO. 1



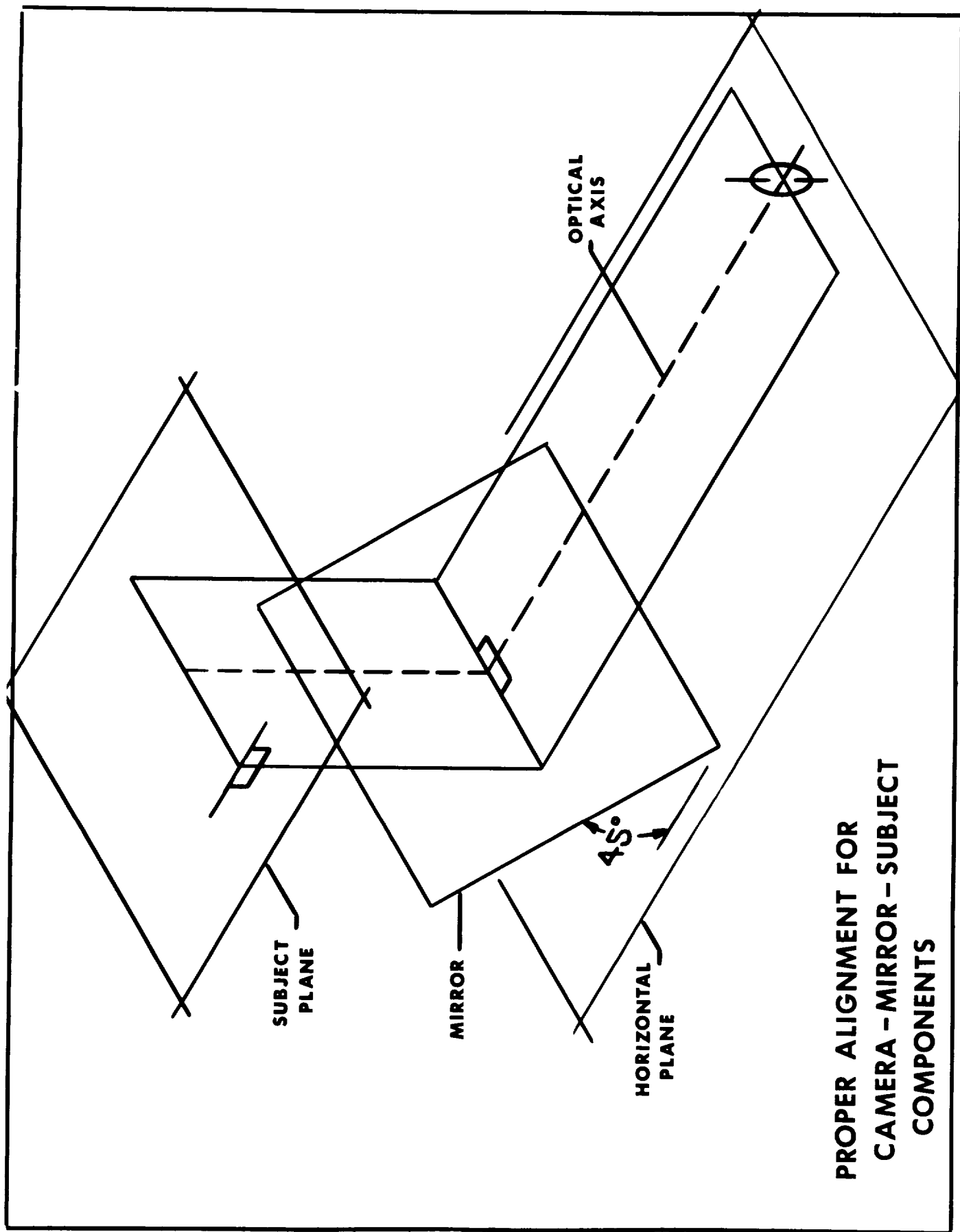
TWO LIGHTS B W MOD 358



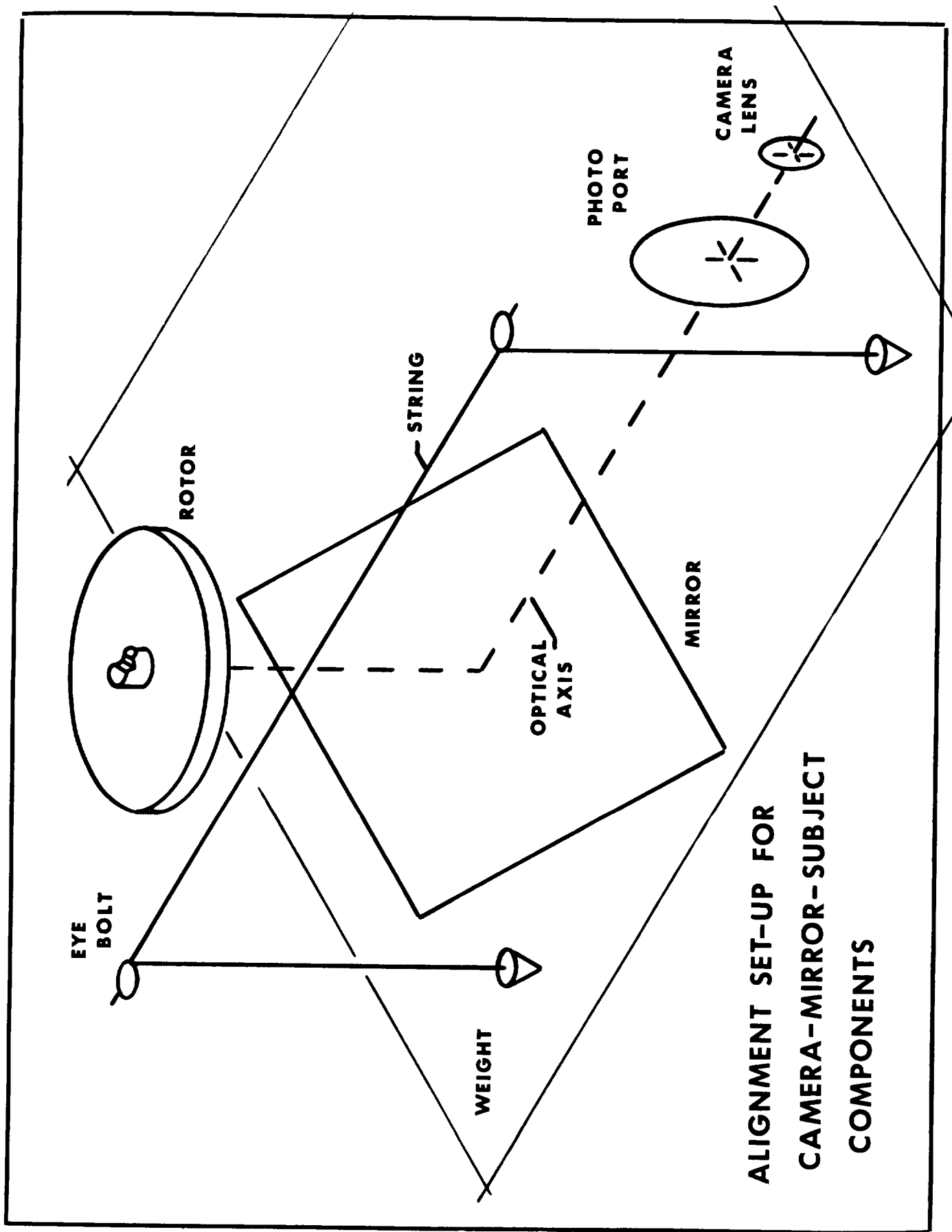
ONE LIGHT B W MOD 358



PICTURE TAKING CAPABILITY OF THE PHOTO SYSTEM
 USING KODAK EF5241 COLOR FILM IN THE DYNAFAX
 CAMERA OUTFITTED WITH 3/8 STOPS



**PROPER ALIGNMENT FOR
CAMERA - MIRROR - SUBJECT
COMPONENTS**

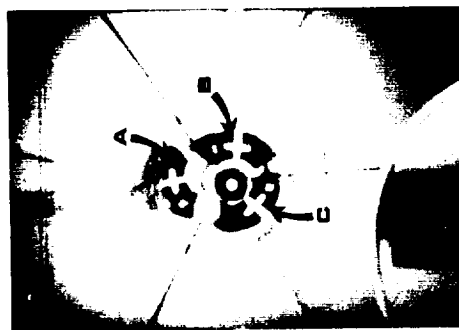


**ALIGNMENT SET-UP FOR
CAMERA-MIRROR-SUBJECT
COMPONENTS**

TEST NO. 2

Picture number

2-1



t=0

2-5



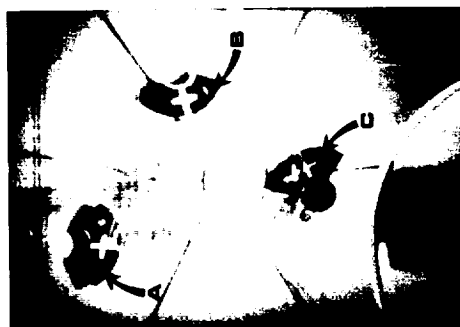
t=800

2-9



t=1600

2-13

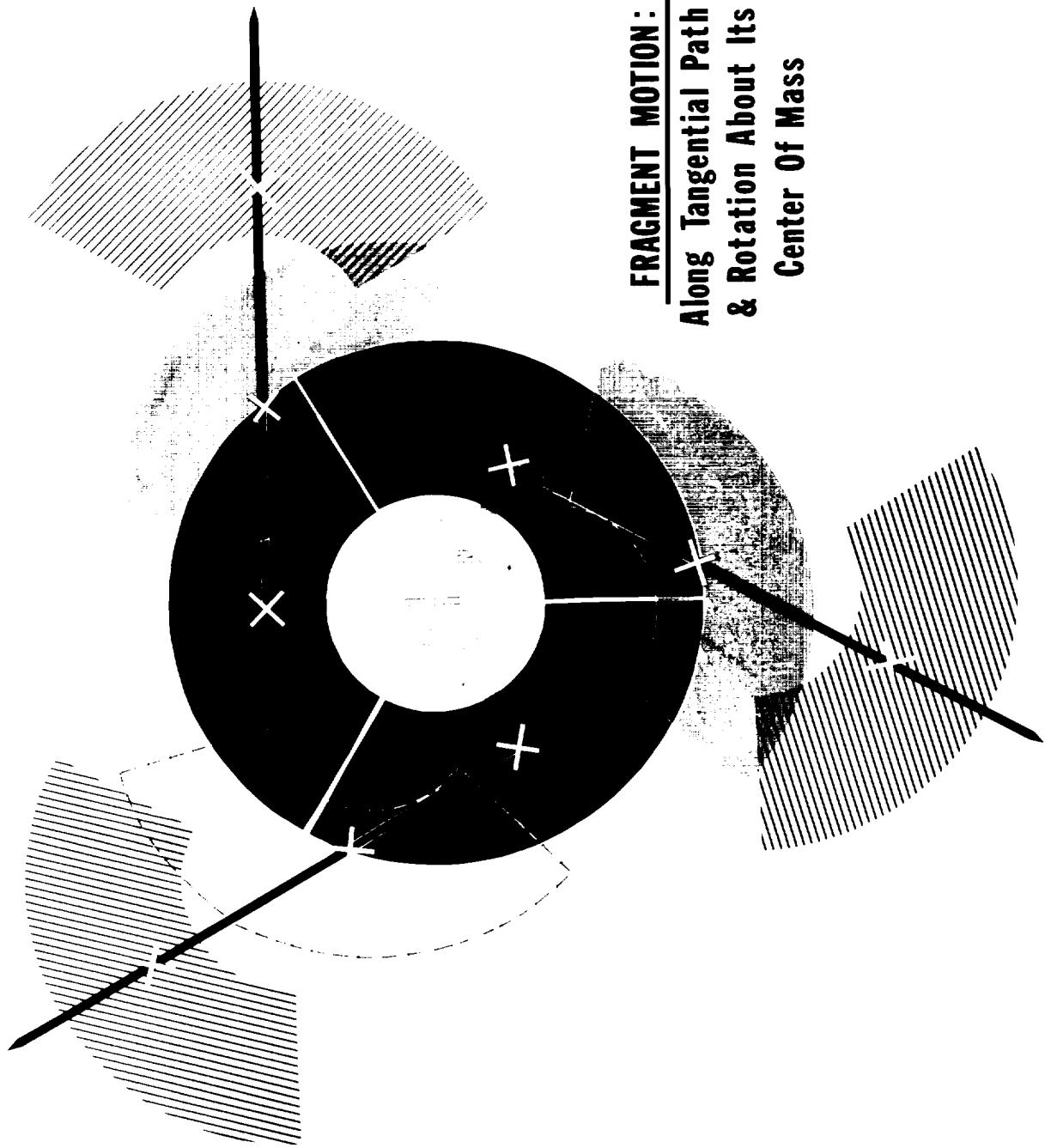


t=2400

t = Time (microseconds) since first picture

FRAGMENT TRAJECTORY & MOTION

IDEAL TRI-HUB DISK BURST

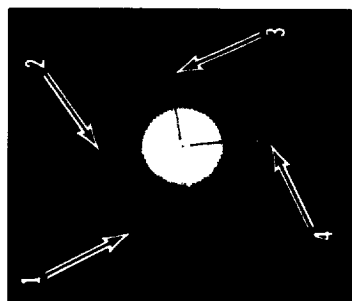


FRAGMENT MOTION:
Along Tangential Path
& Rotation About Its
Center Of Mass

TEST NO. 10 SINGLE BLADE-RING INTERACTION

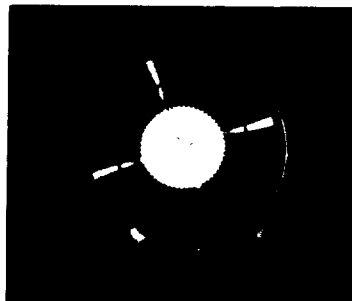
Picture number:

10-1



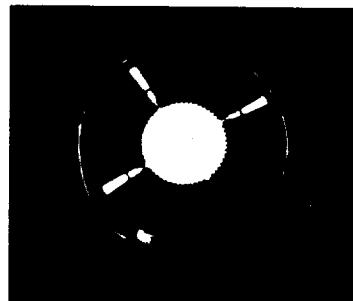
$t=0$

10-2



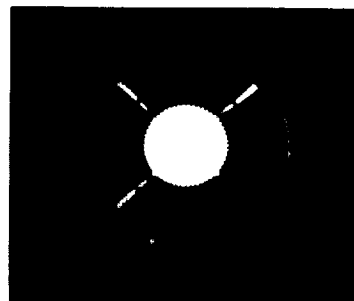
$t=66.6$

10-3



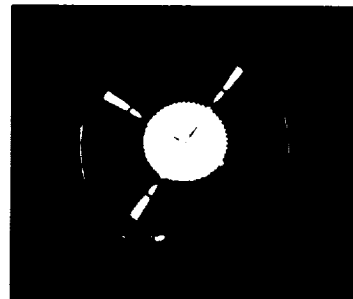
$t=133.2$

10-4



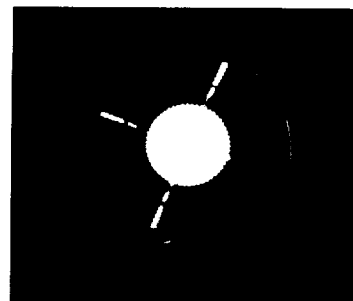
$t=199.8$

10-5



$t=266.4$

10-6



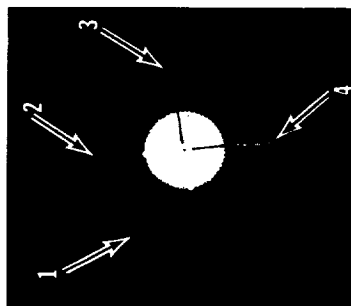
$t=333.0$

$t=$ Time(microseconds) since first picture

TEST NO. 10 RING DEFORMATION DUE TO A SINGLE BLADE IMPACT

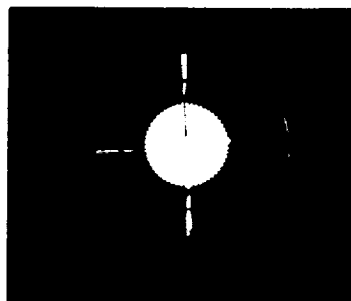
Picture number:

10-1



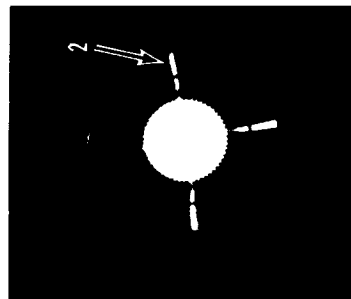
t=0

10-8



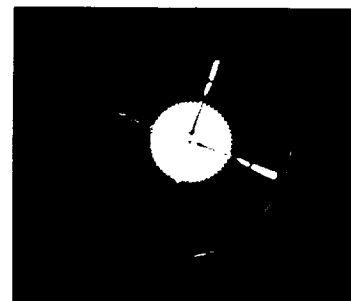
t=466.2

10-23



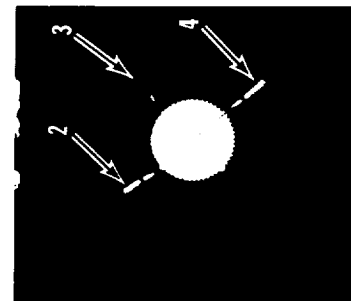
t=1465.2

10-28



t=1798.2

10-33



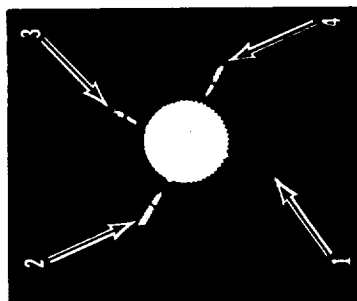
t=2131.2

t=Time (microseconds) after first picture

TEST NO. 10 SINGLE BLADE DYNAMICS & RING INTERACTIONS

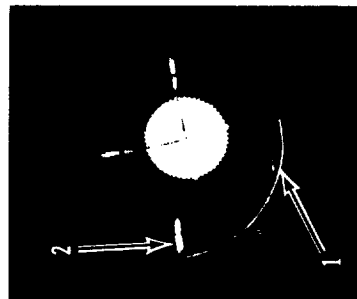
Picture number:

10-35



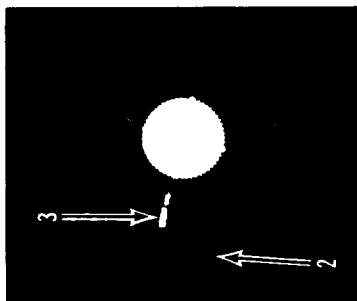
t=2264.4

10-38



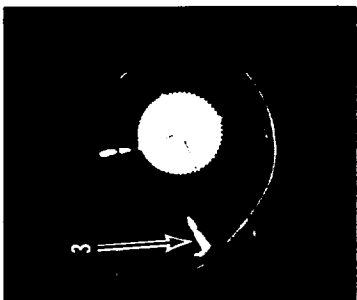
t=2464.2

10-43



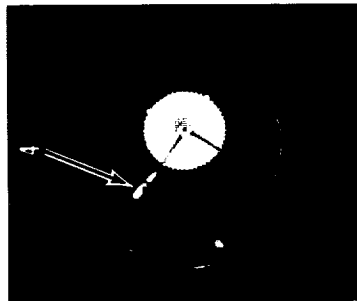
t=2797.2

10-46



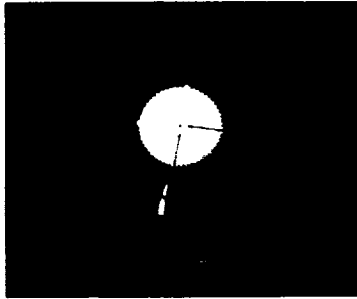
t=2997.0

10-49



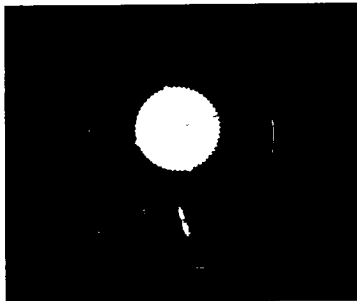
t=3196.8

10-51



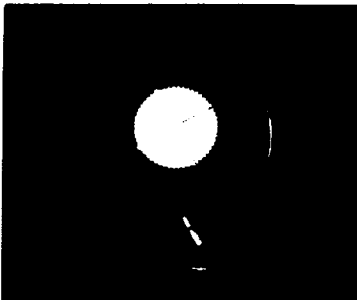
t=3330.0

10-53



t=3463.2

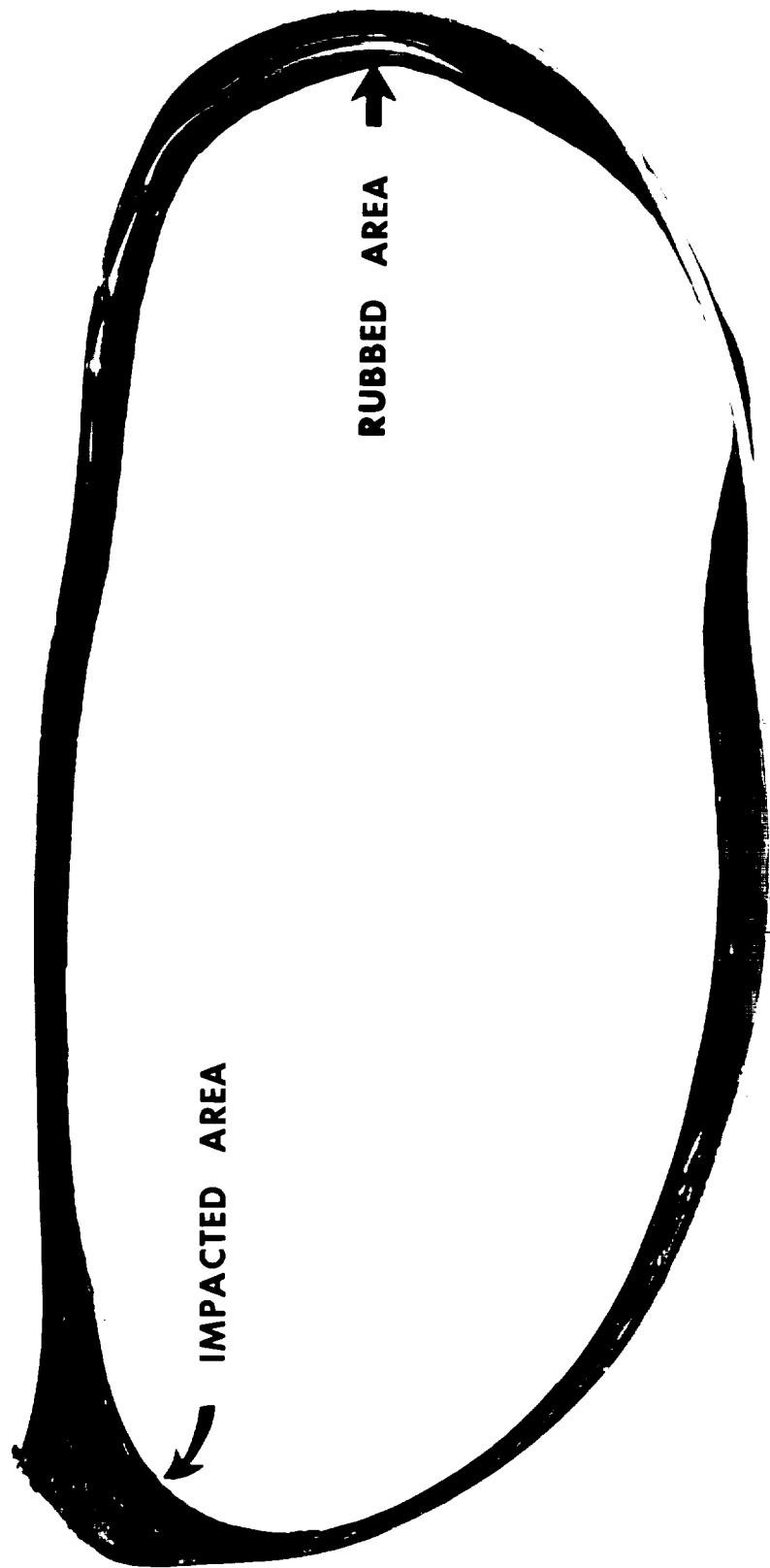
10-54



t=3529.8

t=Time (microseconds) since first picture

**POST-TEST NO. 10
CONTAINMENT RING**



POST-TEST NO. 10
CONTAINMENT RING-RUBBED AREA DETAIL

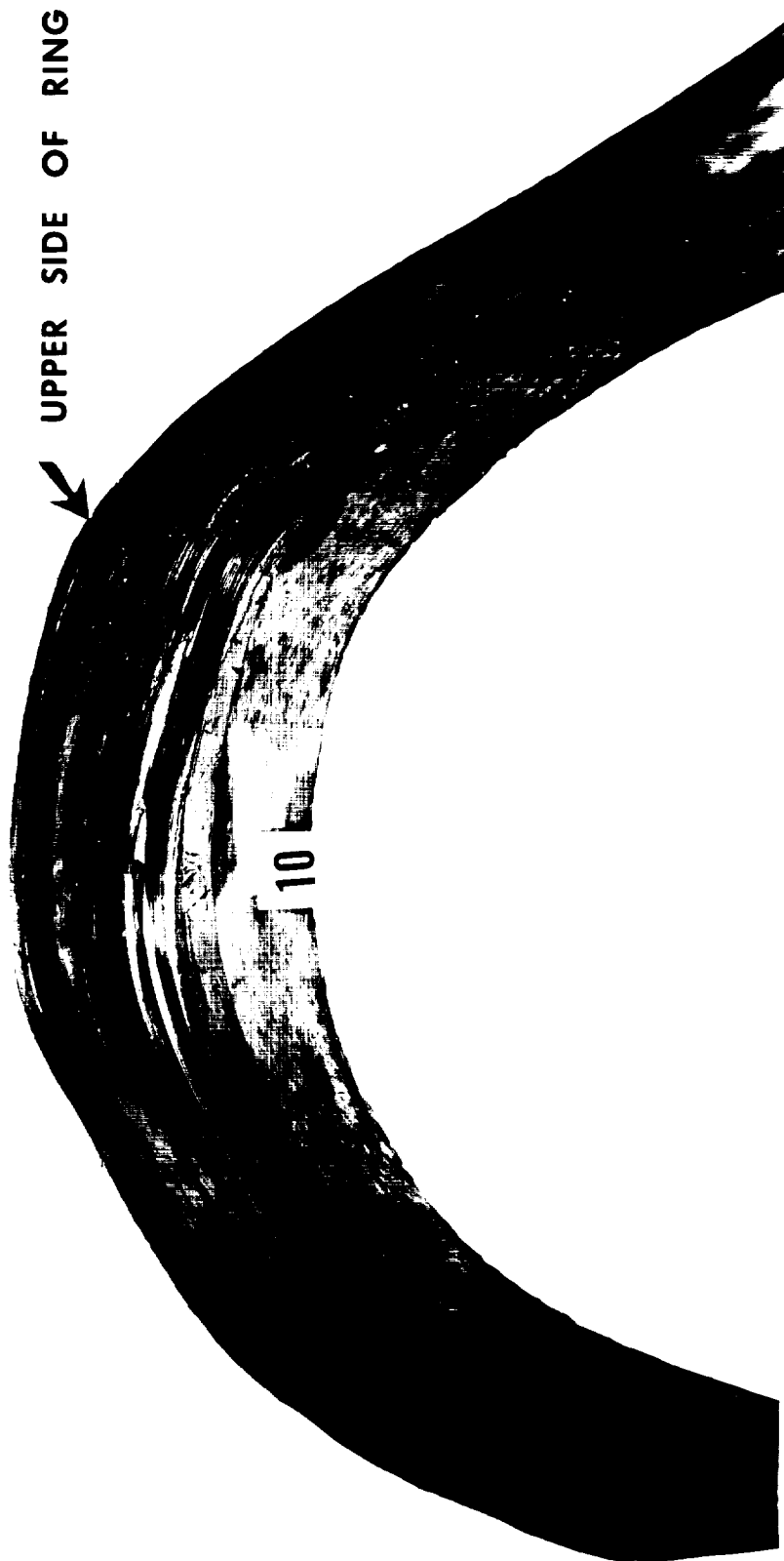


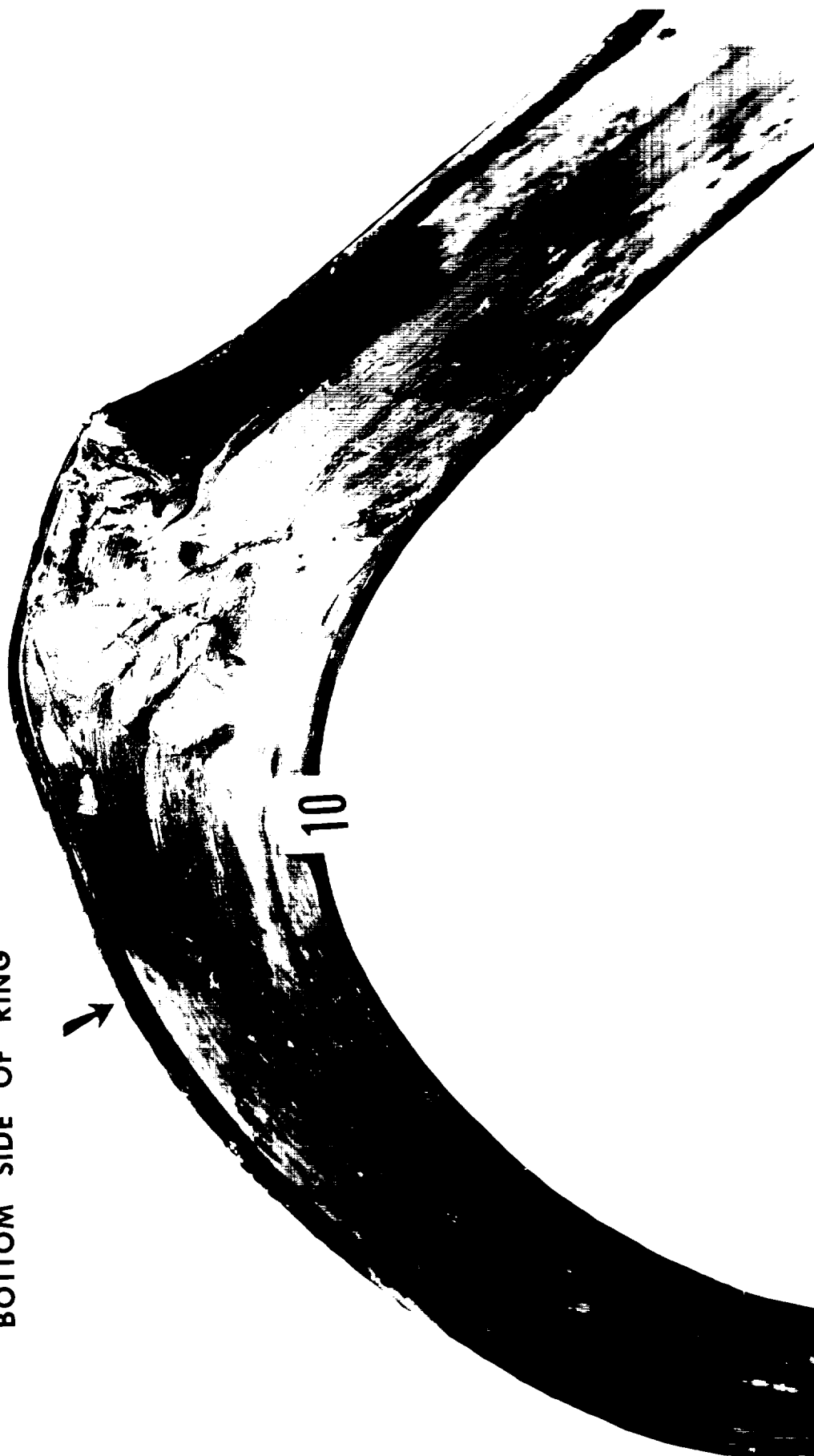
PHOTO NO: CAN-383340(L)-7-67

PLATE 20

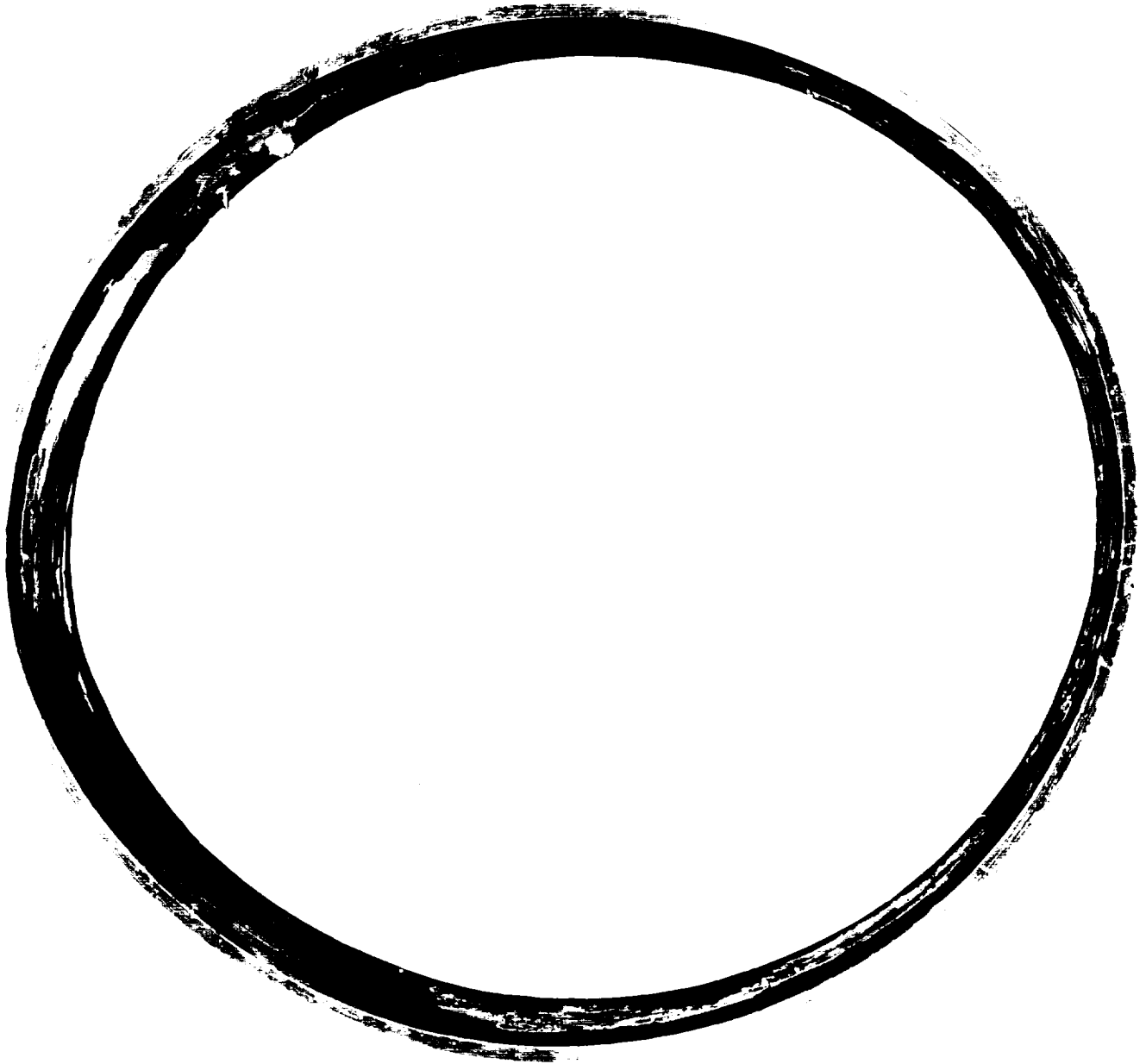
PLATE 20

POST-TEST NO. 10
CONTAINMENT RING-IMPACT AREA DETAIL

BOTTOM SIDE OF RING



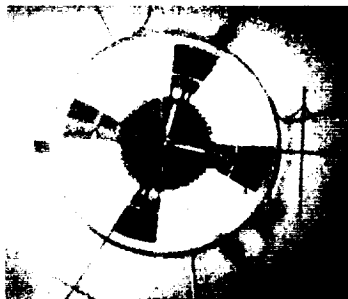
POST-TEST NO. 7
CONTAINMENT RING



TEST NO. 11 BLADE FAILURE FROM A PARTIALLY FULL ROTOR

Picture number:

11-0



11-1



t=0

11-3



t=270

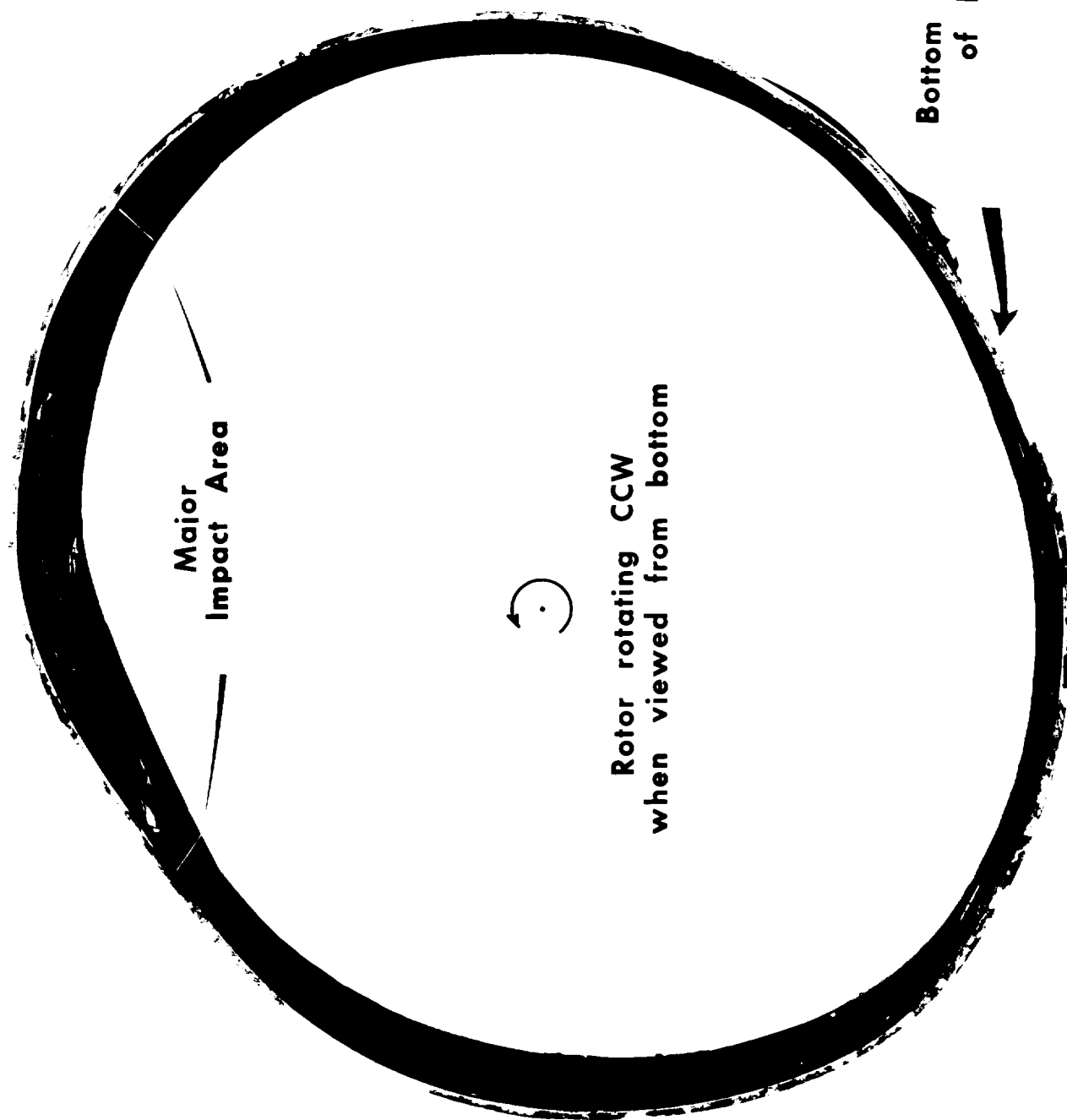
11-5



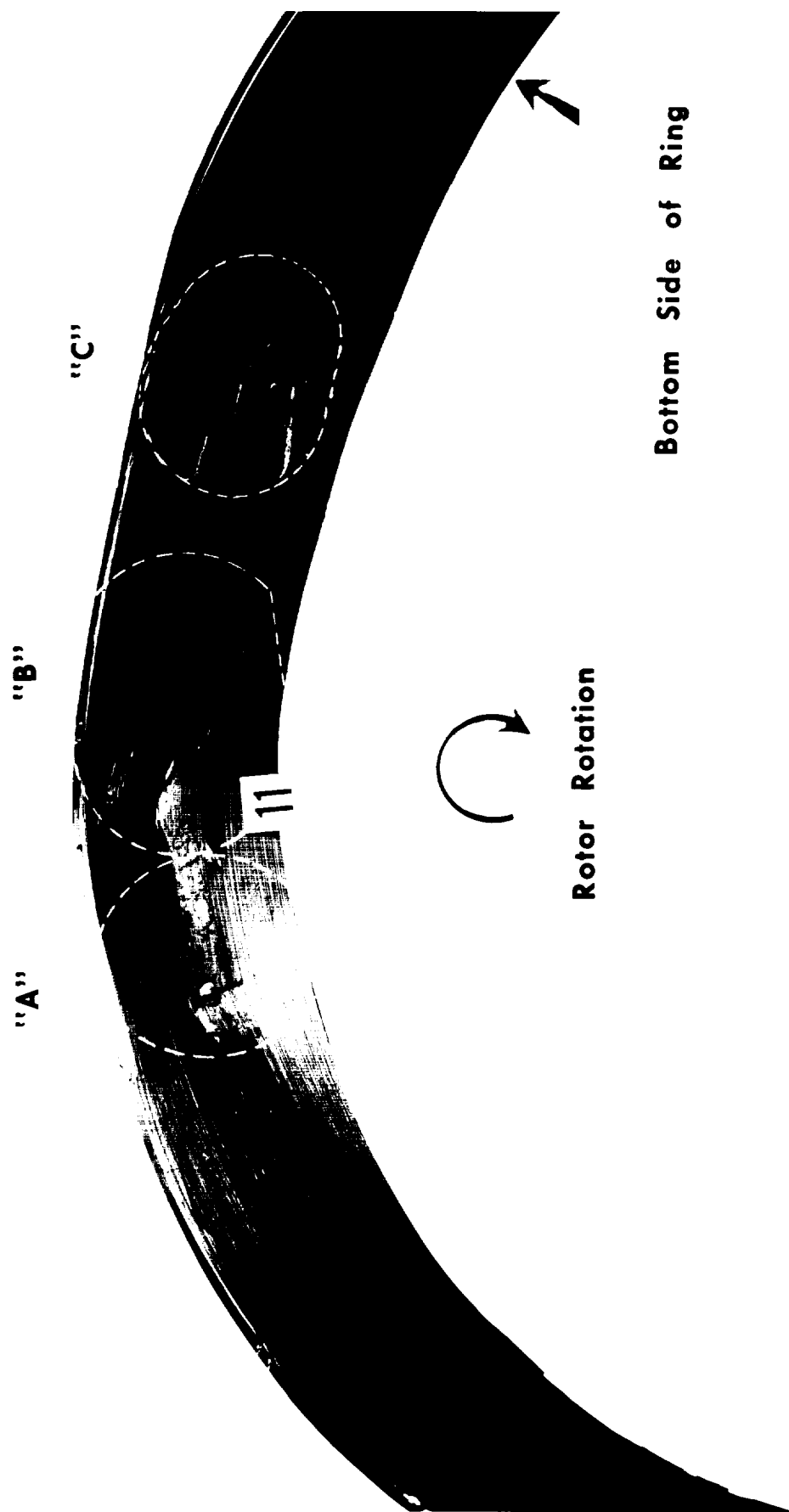
t=540

t = Time (microseconds) since first picture
A = Paper photo-triggering strip
B = Ring supporting chains

POST-TEST NO. 11 CONTAINMENT RING



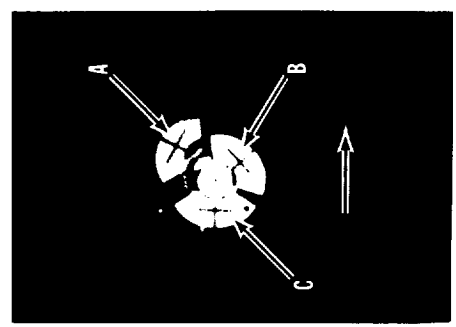
POST-TEST NO. 11
CONTAINMENT RING-DETAIL OF IMPACTED AREA



TEST NO. 4

ROTOR FRAGMENT KINEMATICS & FRAGMENT-RING INTERACTIONS

Picture number:
4-1



$t=0$

4-9



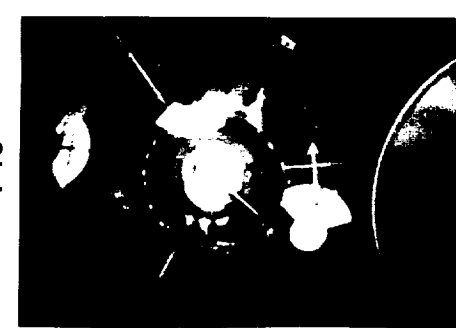
$t=1504$

4-11



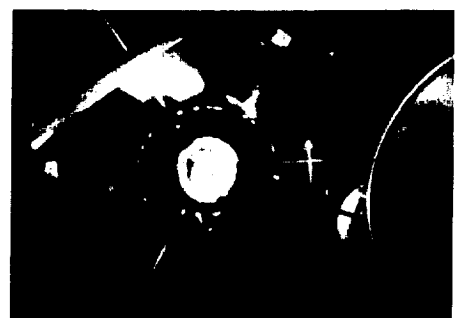
$t=1880$

4-13



$t=2256$

4-21



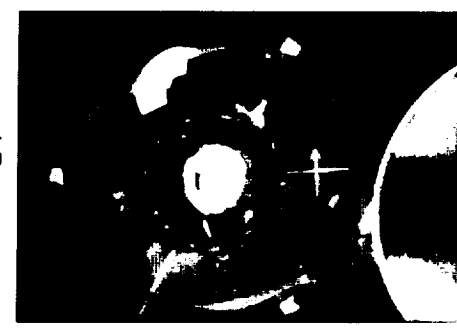
$t=3760$

4-23



$t=4136$

4-24



$t=4324$

t =Time (microseconds) since first picture

POST-TEST NO. 4 CONTAINMENT RING



PHOTO NO: CAN-383329(L)-7-67

PLATE 27

PLATE 27

POST-TEST NO. 4
CONTAINMENT RING- FRAGMENT A IMPACTED AREA

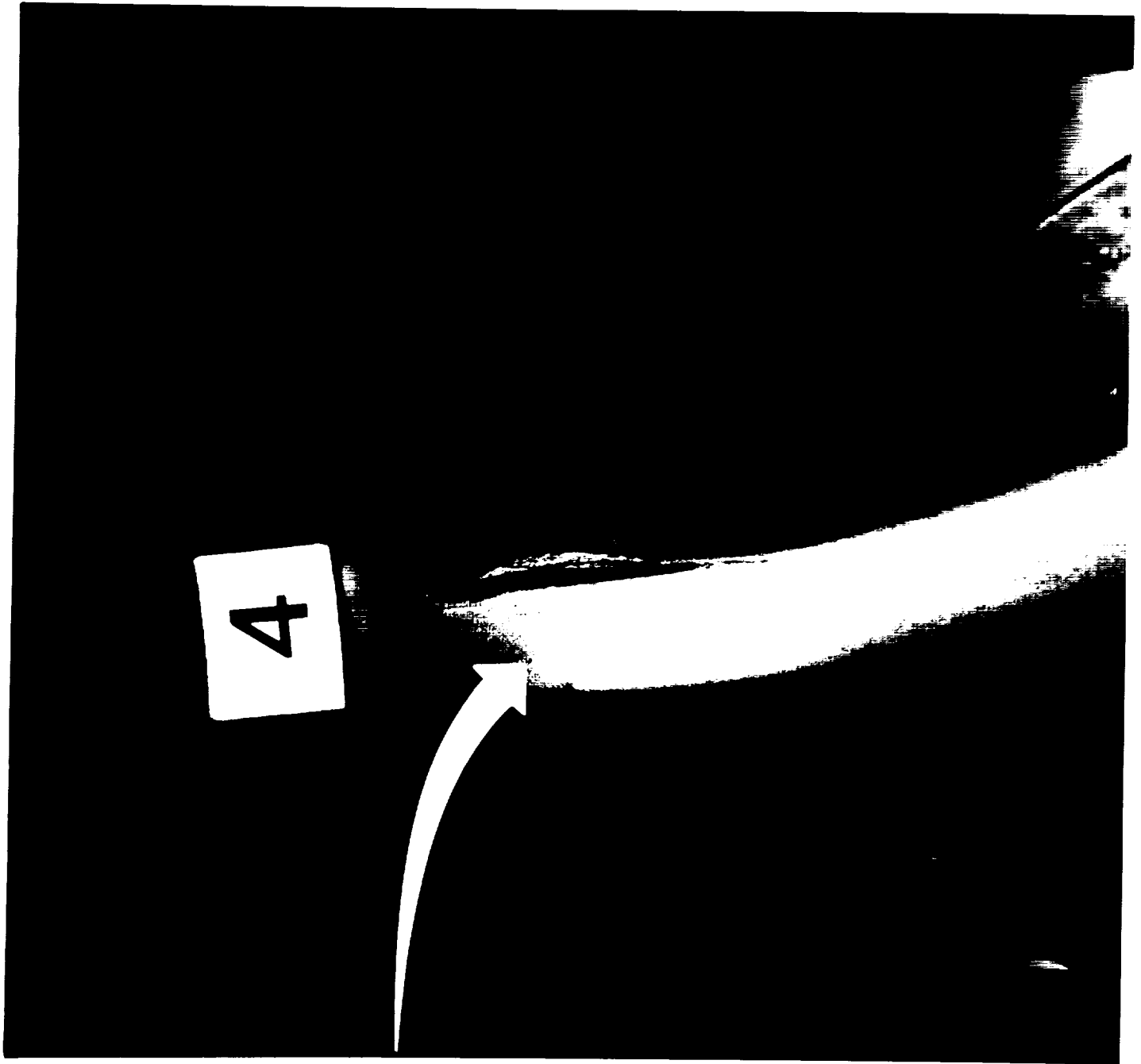


POST-TEST NO. 4
CONTAINMENT RING- FRAGMENT B IMPACTED AREA

Bottom side of ring



POST-TEST NO. 4
CONTAINMENT RING-
FRAGMENT C IMPACTED AREA



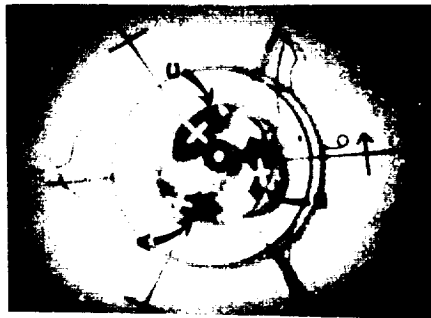
Outside surface of ring

TEST NO. 6

TRI-HUB BURST WITHIN A STEEL RING; LARGE RADIAL CLEARANCE

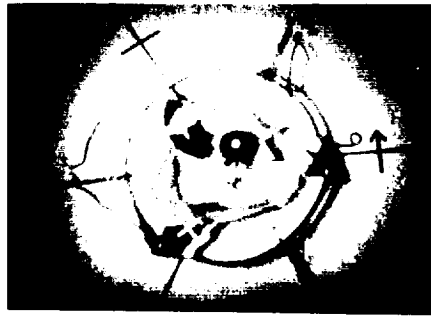
Picture number :

6-2



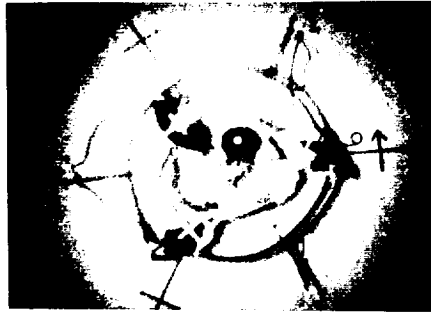
t=184

6-6



t=920

6-7



t=1104

6-18



t=3128

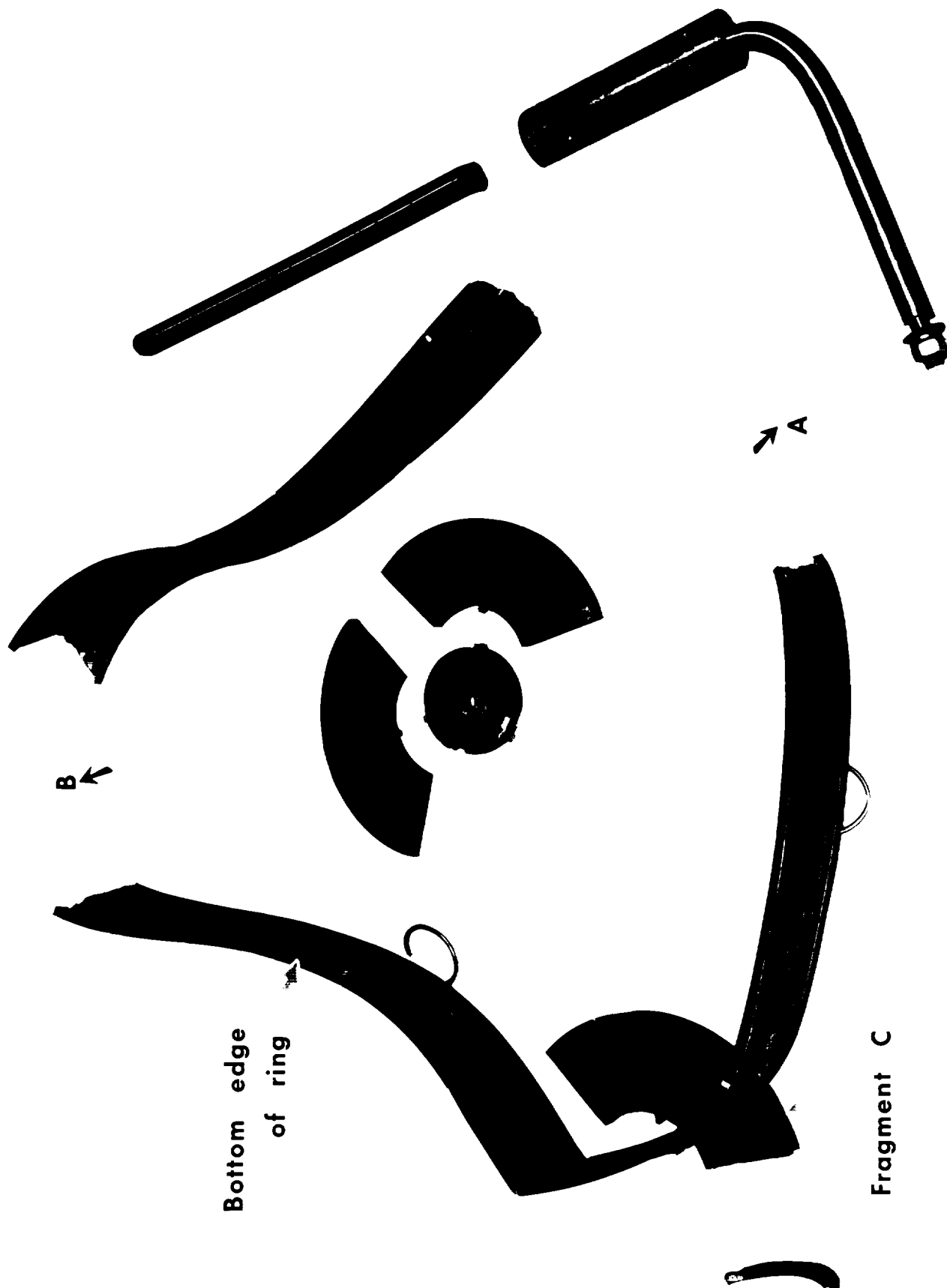
6-24



t=4232

t=Time (microseconds) since first picture

POST-TEST NO. 6 CONTAINMENT RING



FRAGMENT C IMPACTED AREA
POST-TEST NO. 6 CONTAINMENT RING



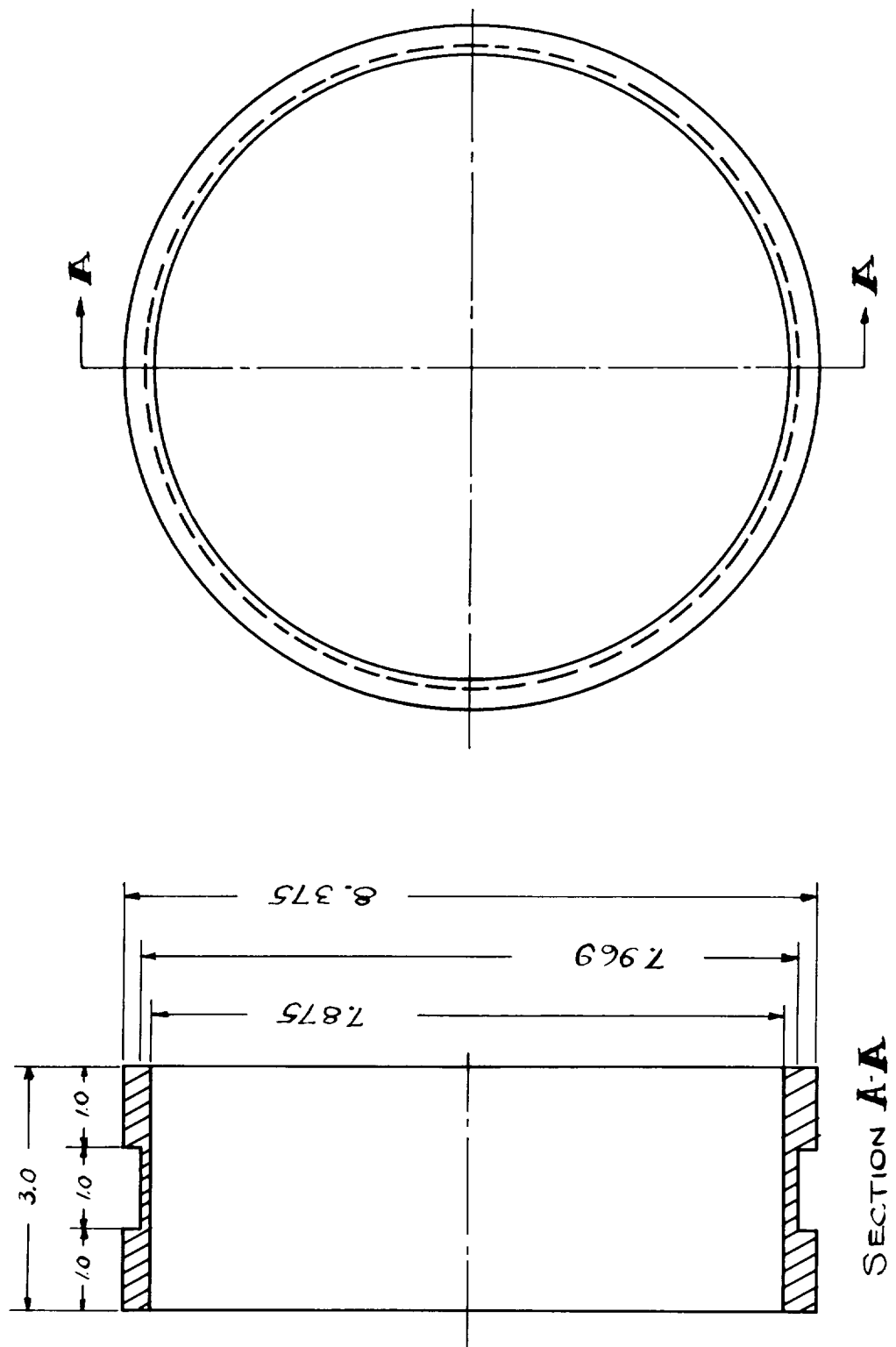
PHOTO NO: CAN-383347(L)-7-67

PLATE 33

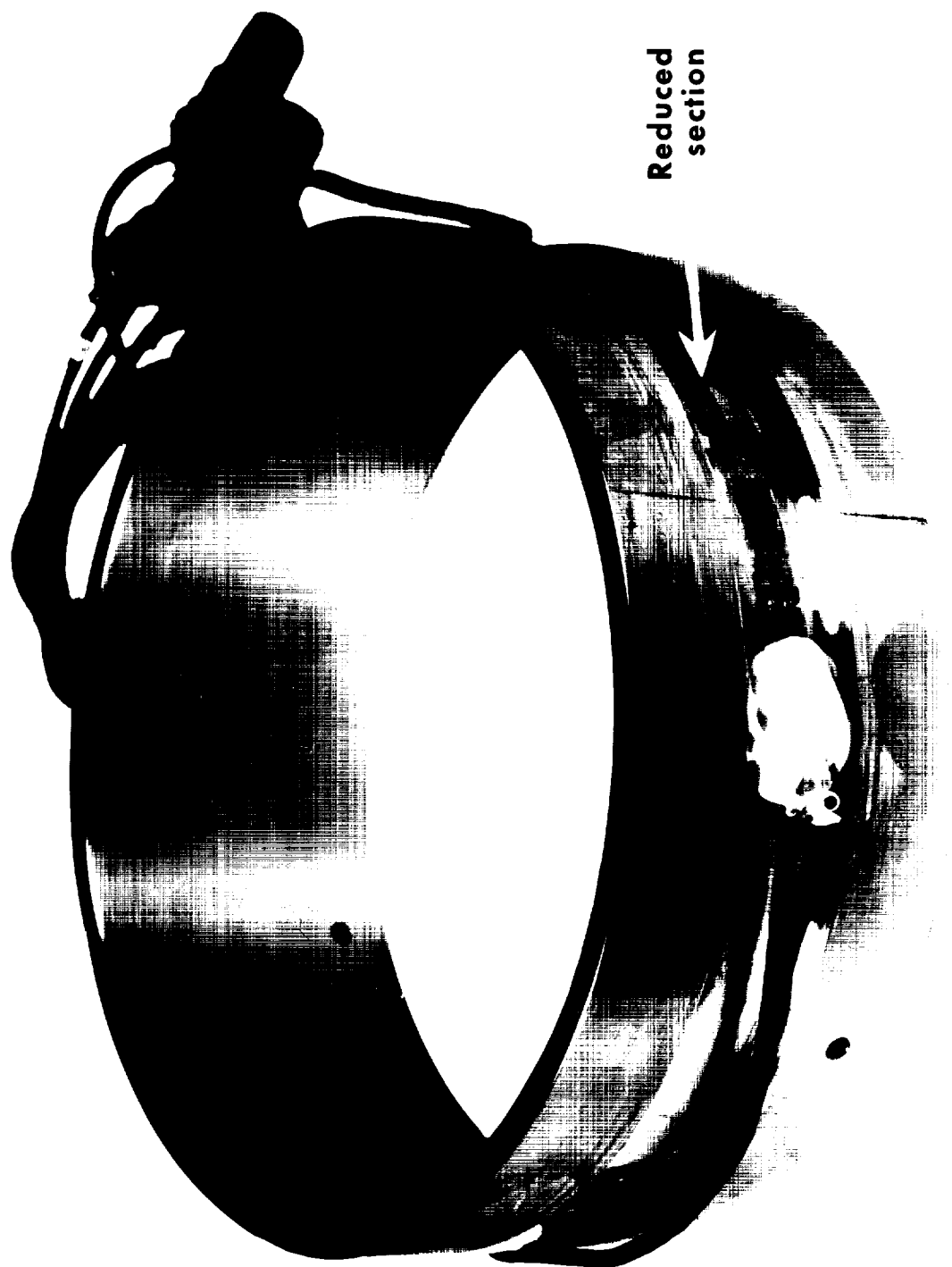
PLATE 33

CONTAINMENT RING

TEST NO. 12, 13, 14, 15, & 21



TEST NO. 12 CONTAINMENT RING



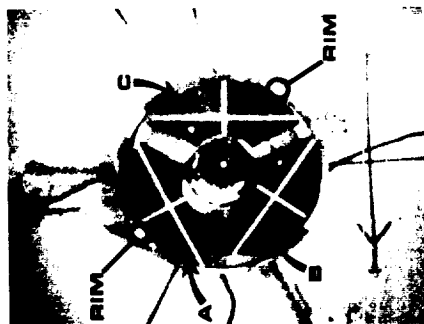
Reduced
section

Strain gage

TEST NO. 12 TRI-HUB BURST WITHIN A STEEL RING; SMALL RADIAL CLEARANCE

Picture number :

12-1



$t=0$

12-9



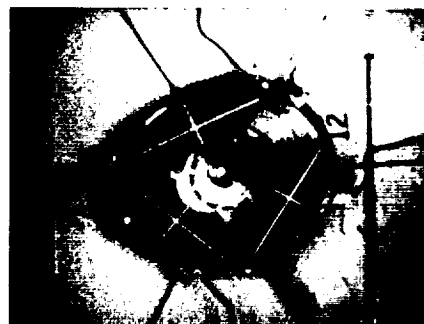
$t=624$

12-21



$t=1560$

12-33



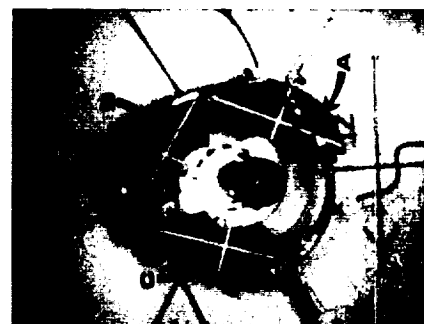
$t=2496$

12-43



$t=3276$

12-57



$t=4368$

12-87



$t=6708$

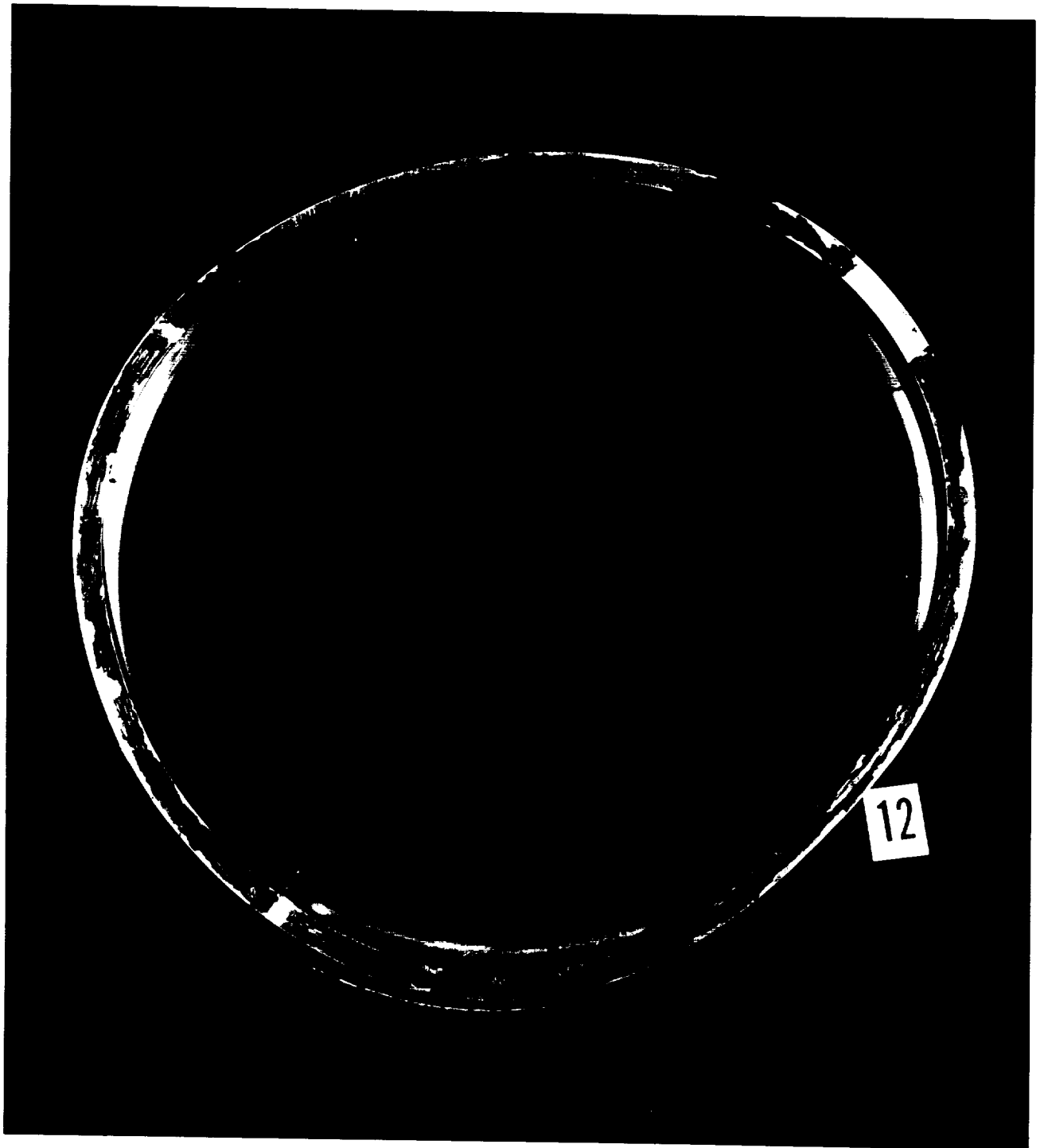
12-125



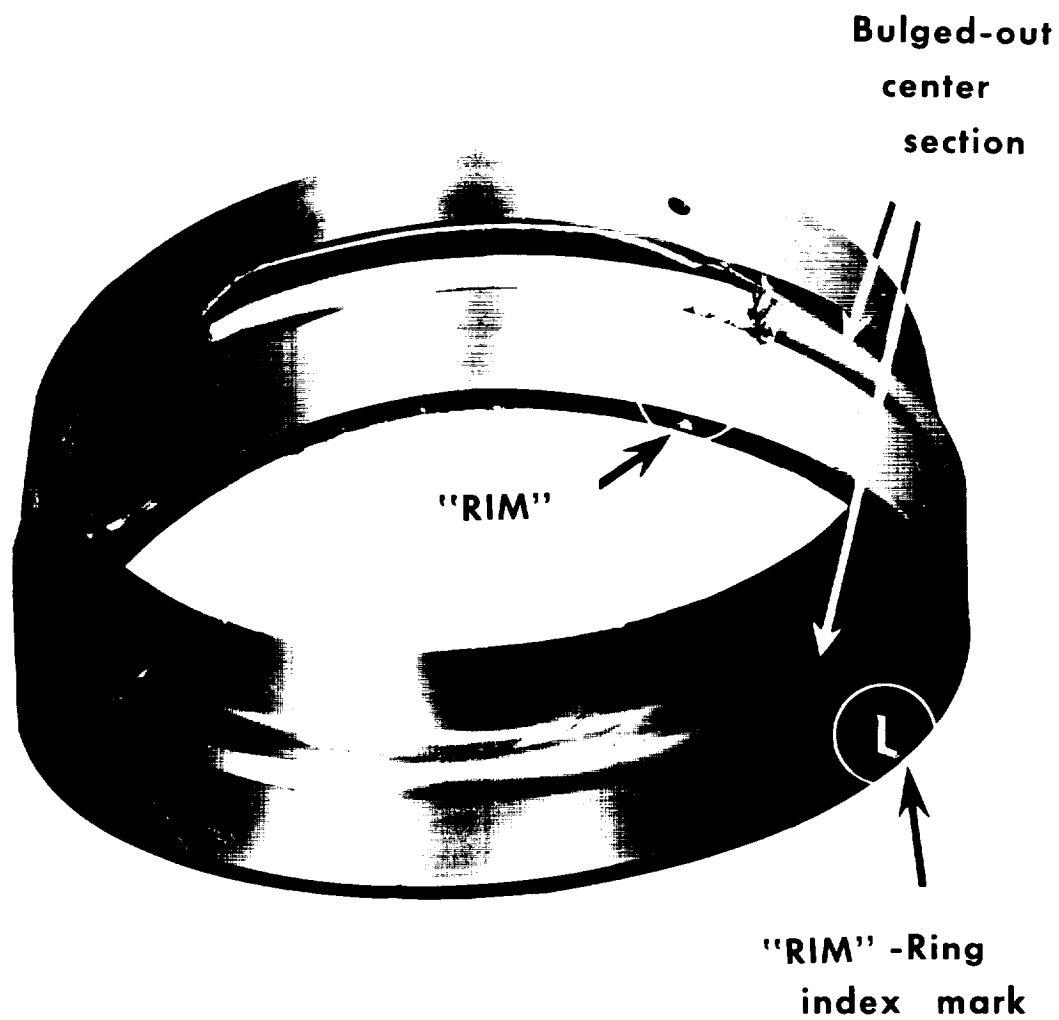
$t=9672$

t =Time (microseconds) since first picture
"Rim" = Ring Index Mark

POST-TEST NO. 12 CONTAINMENT RING



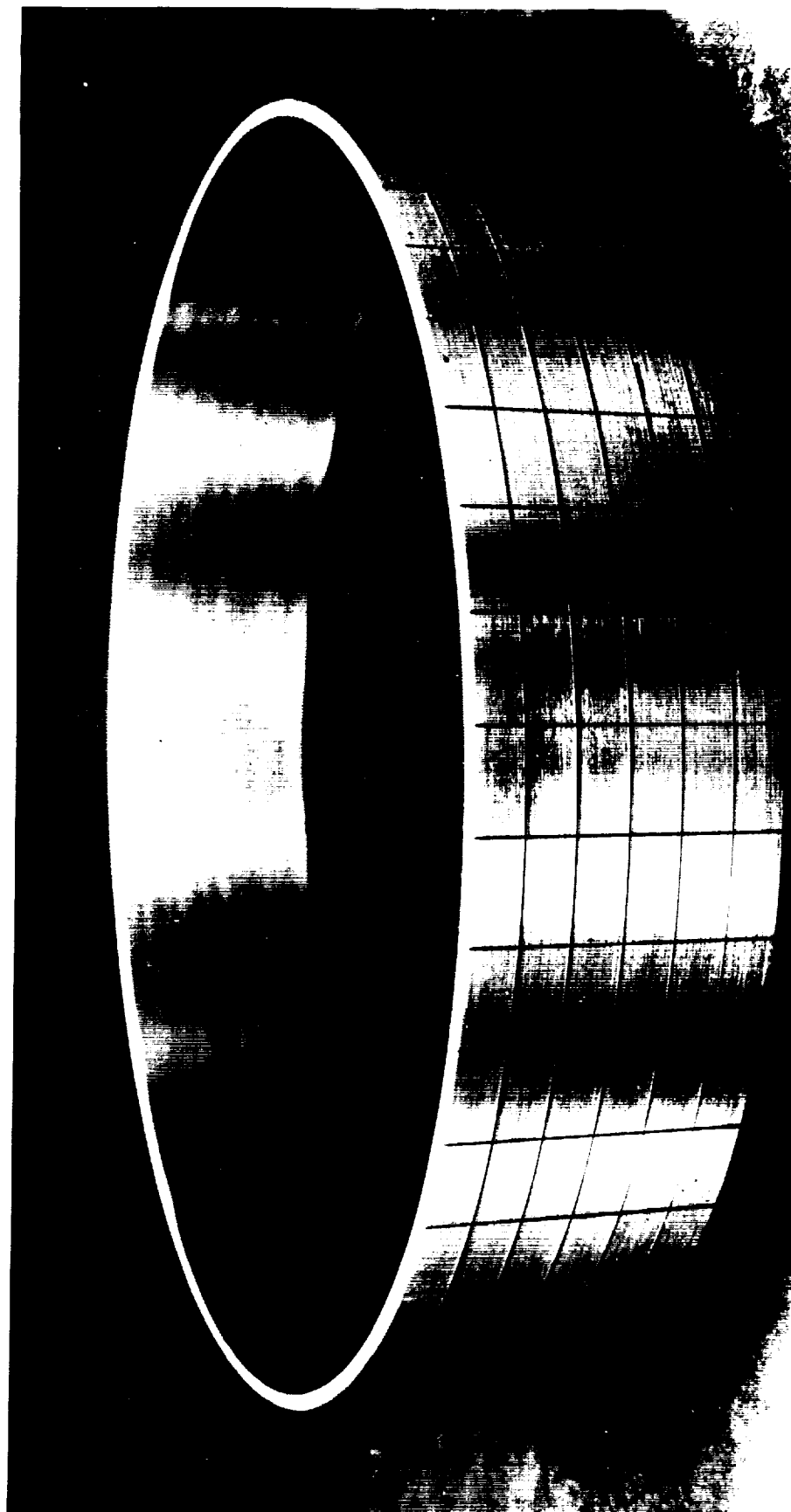
POST-TEST NO. 12
CONTAINMENT RING-FRAGMENT A PERFORATED AREA



POST-TEST NO. 12 CONTAINMENT RING
BULGED-OUT CENTER SECTION

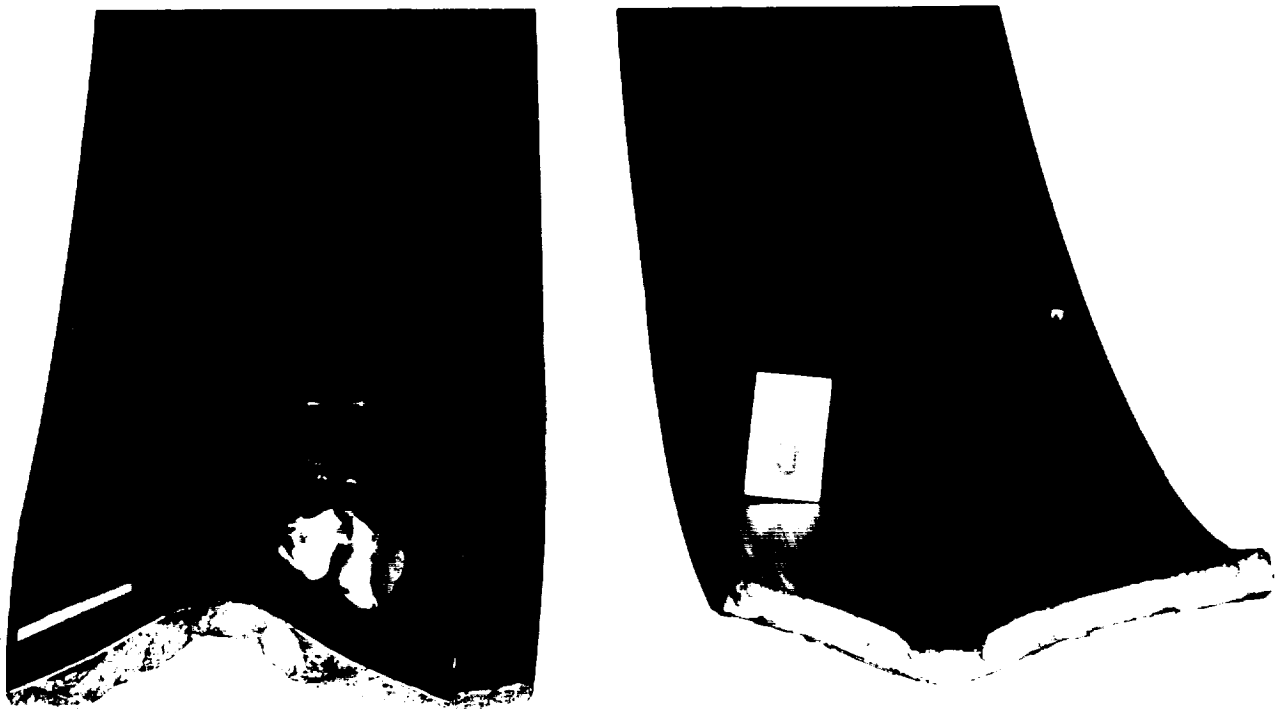


TEST NO. 6 CONTAINMENT RING

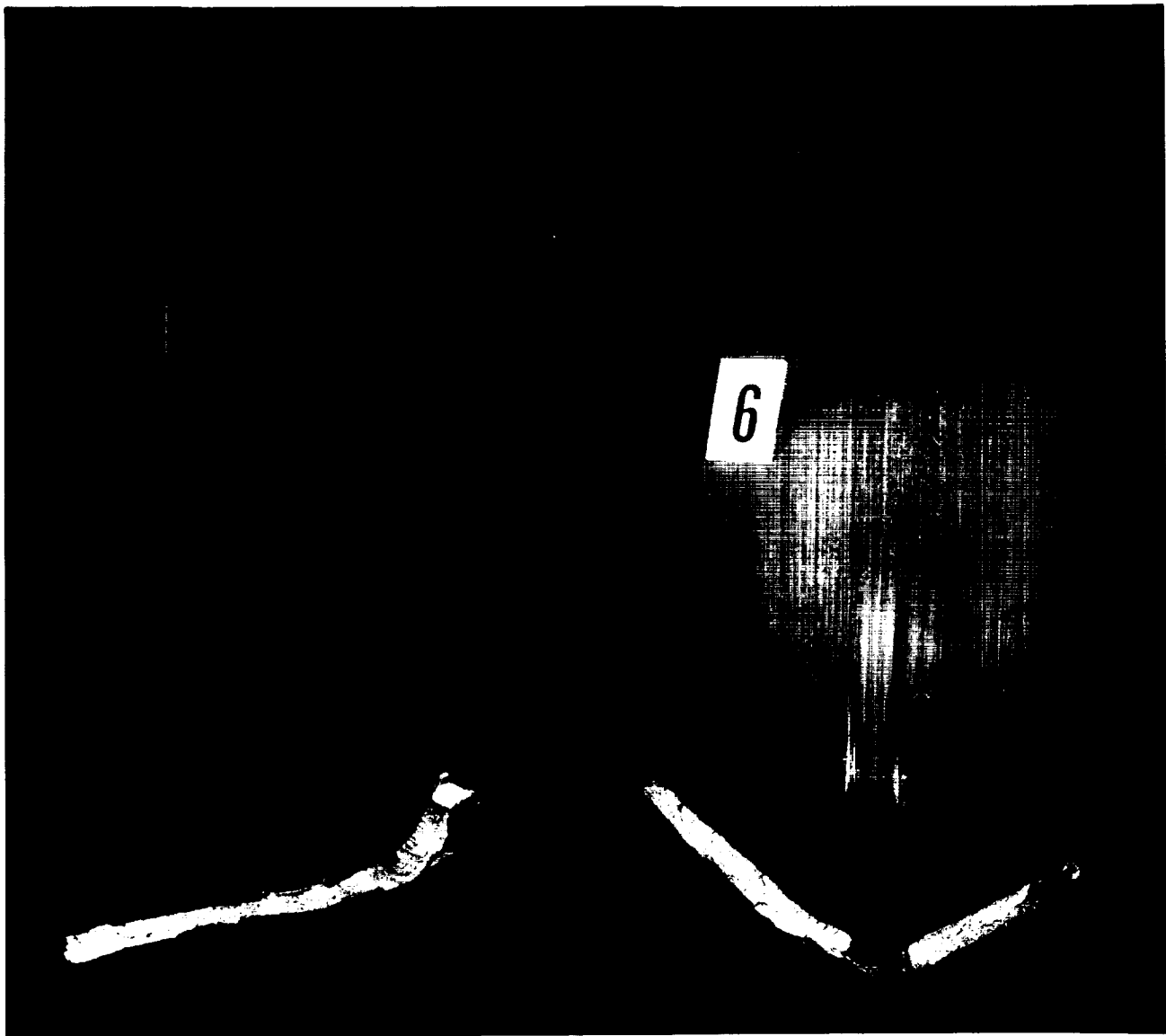


Scribe marks 0.010" deep

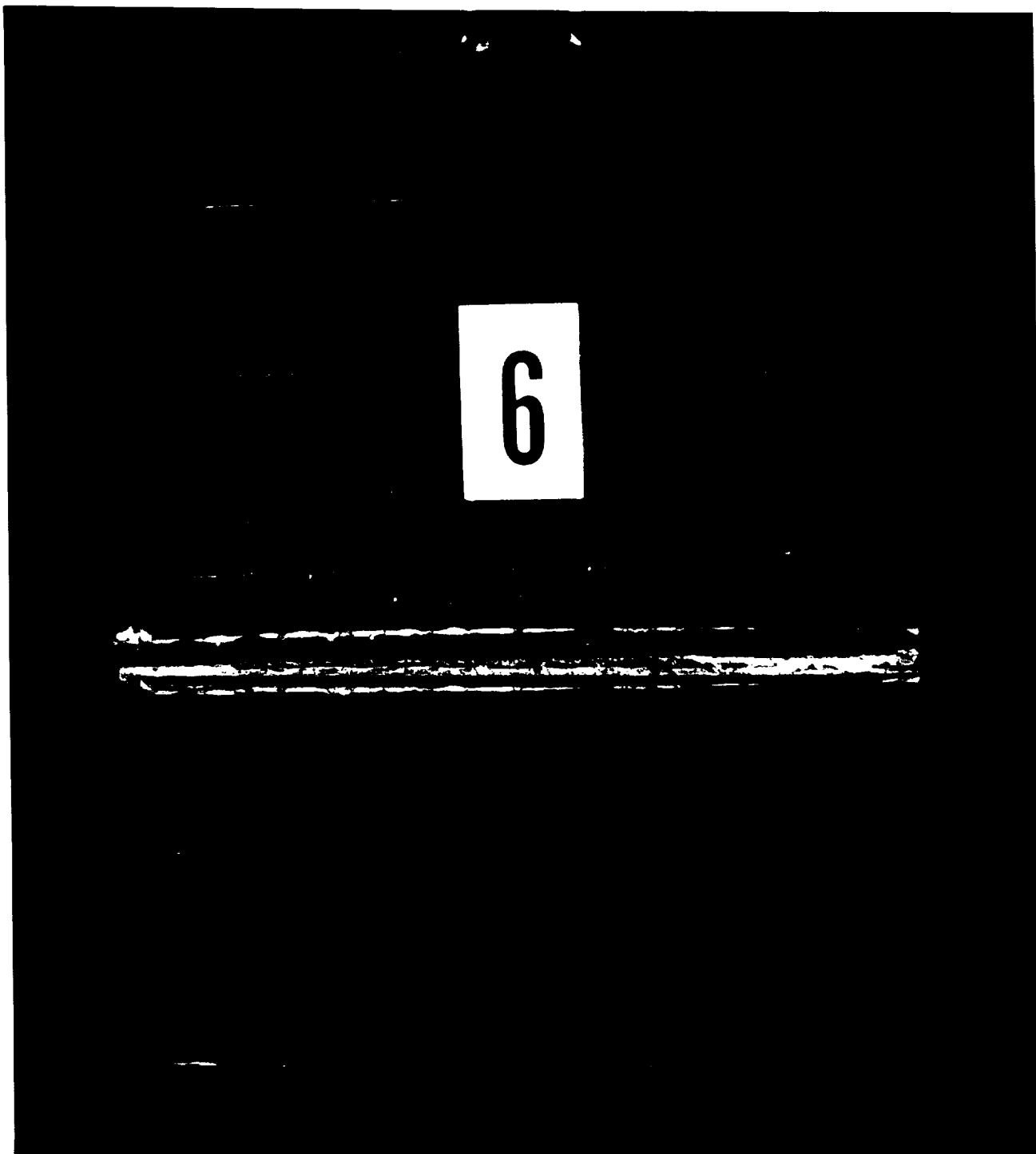
POST-TEST NO. 6 CONTAINMENT RING
FRAGMENT A IMPACTED AREA



POST-TEST NO.6 CONTAINMENT RING
FRAGMENT B IMPACTED AREA



POST-TEST NO. 6 CONTAINMENT RING
FRAGMENT C IMPACTED AREA



POST-TEST NO. 5 CONTAINMENT RING

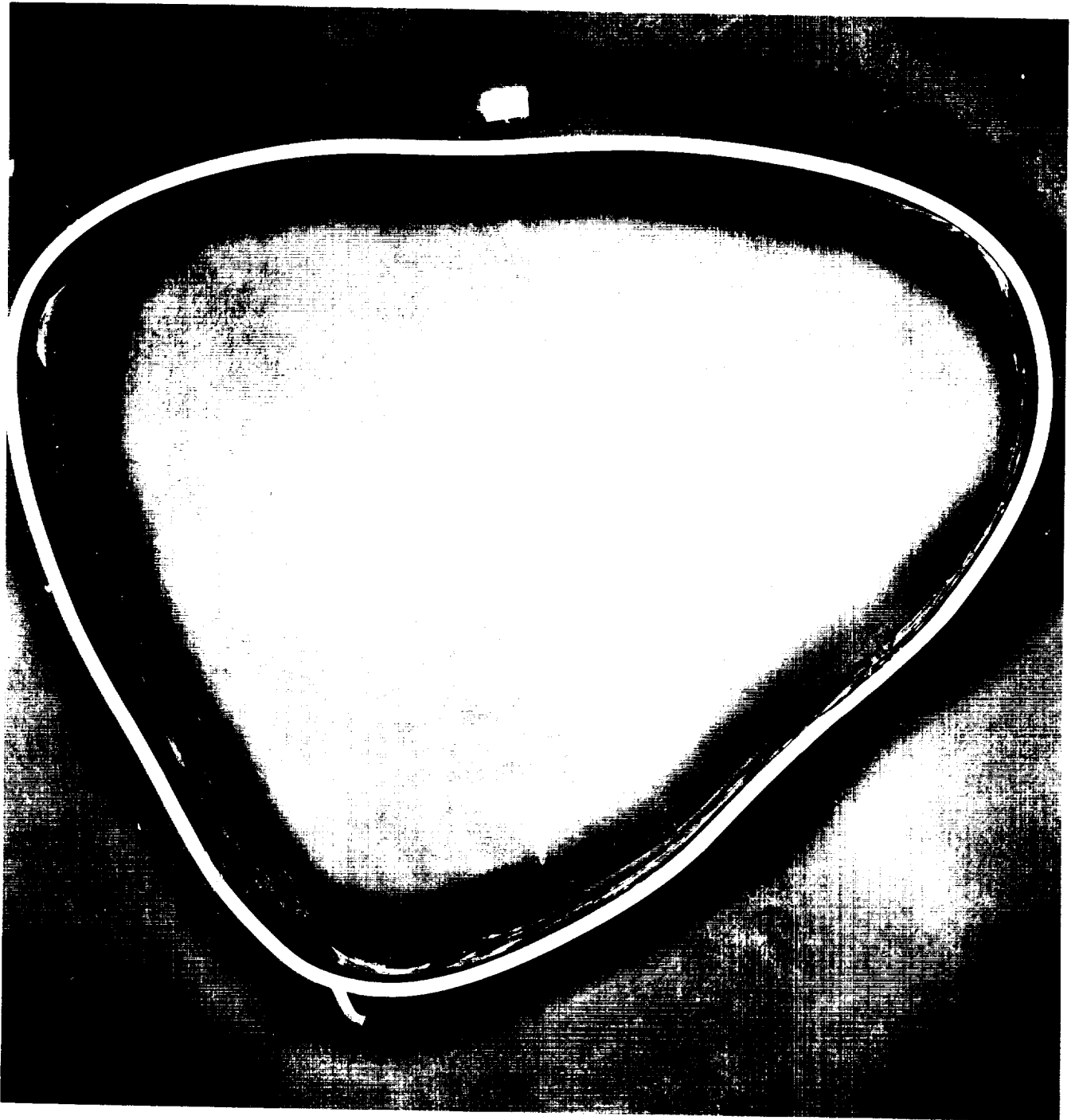


PHOTO NO: CAN-383352(L)-7-67

PLATE 44

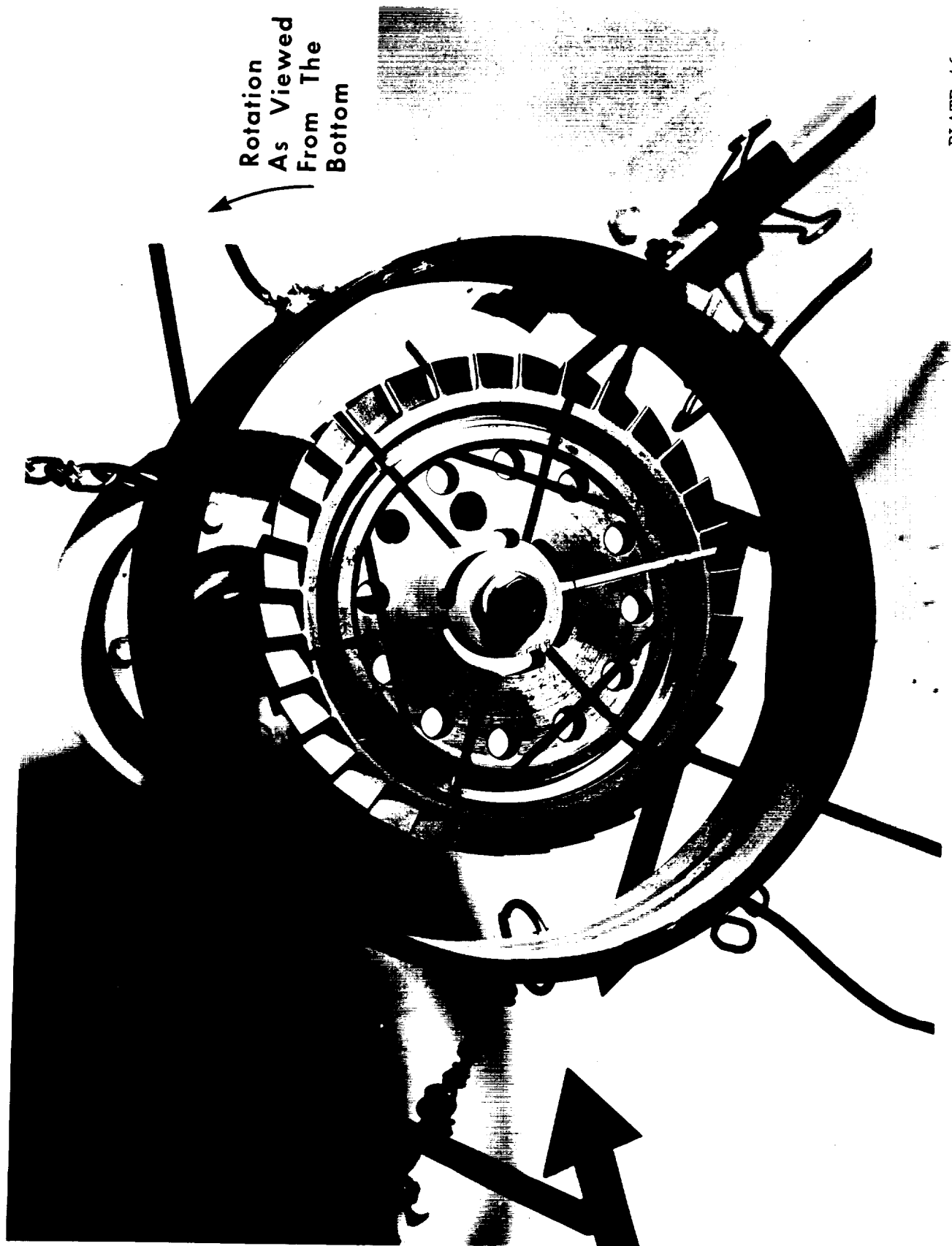
POST-TEST NO.5 CONTAINMENT RING
PERFORATED AREA



PHOTO NO: CAN-383350(L)-7-67

PLATE 45

TEST NO. 20 PRE-TEST ASSEMBLY



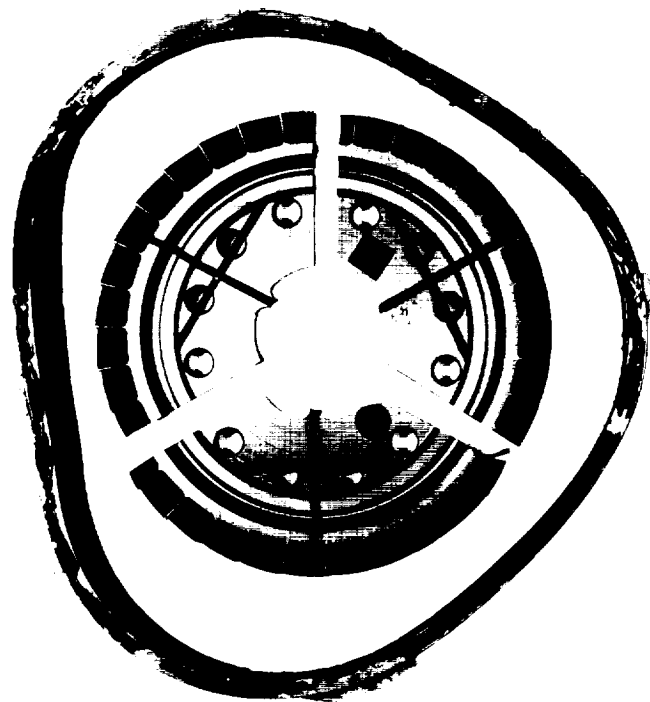
Rotation
As Viewed
From The
Bottom

PLATE 46

PHOTO NO: CAN-384319(L)-9-67

PLATE 46

POST-TEST NO. 20 RING, ROTOR, & DRIVE SPINDLE



Drive Spindle

Rotor Hub

Connector

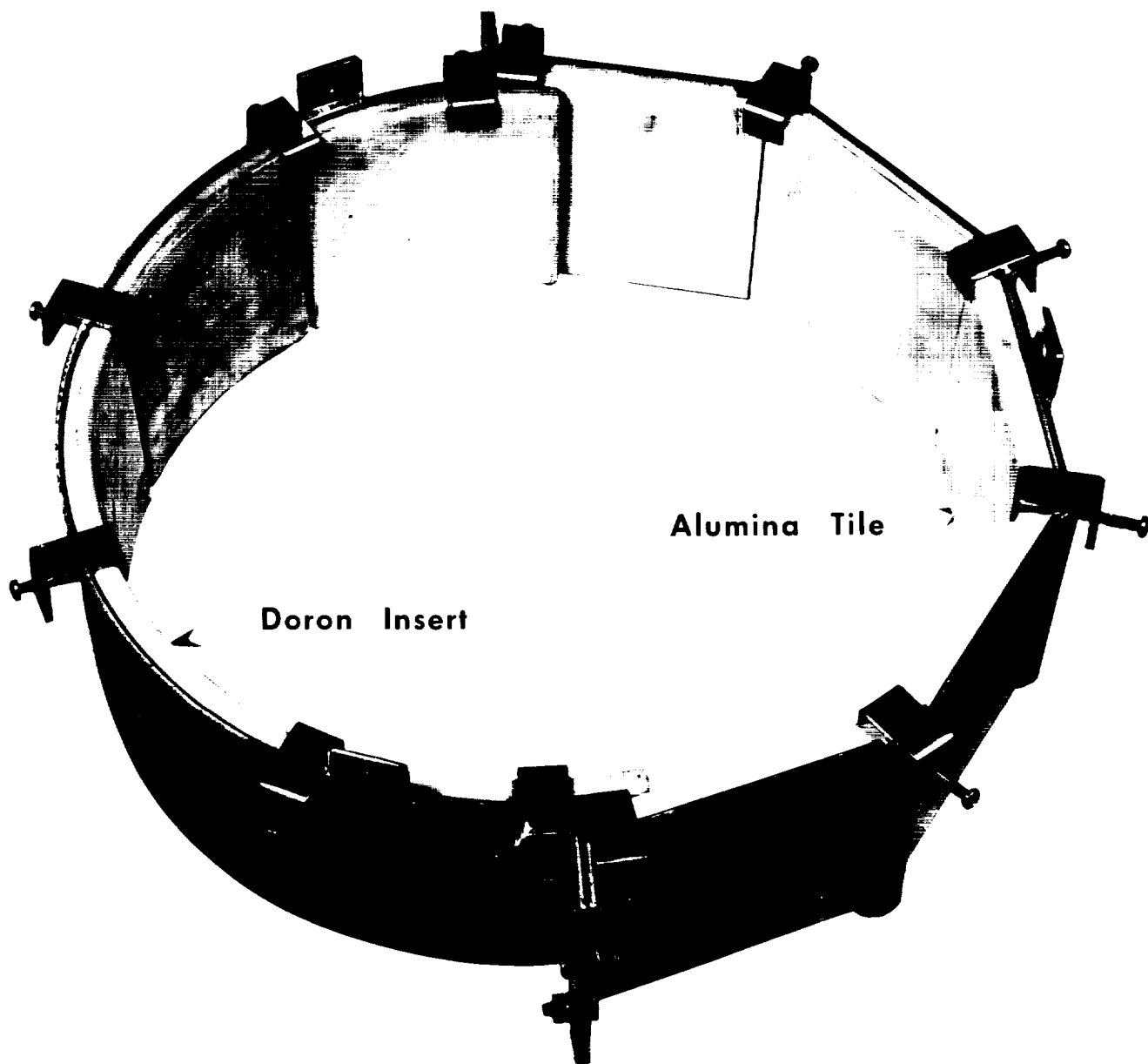
POST-TEST NO. 20
FRAGMENT INDENTATION OF INSIDE
SURFACE OF CONTAINMENT RING



PLATE 48

TEST NO. 17

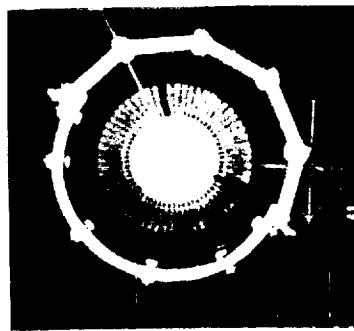
DORON-ALUMINA CONTAINMENT DEVICE



TEST NO. 17
 TRI-HUB ROTOR BURST
 WITHIN A DORON-ALUMINA CONTAINMENT DEVICE

Picture number:

17-0

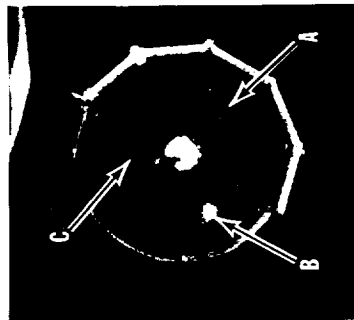


17-2



$t=72.5$

17-3



$t=145.0$

17-4



$t=217.5$

17-5

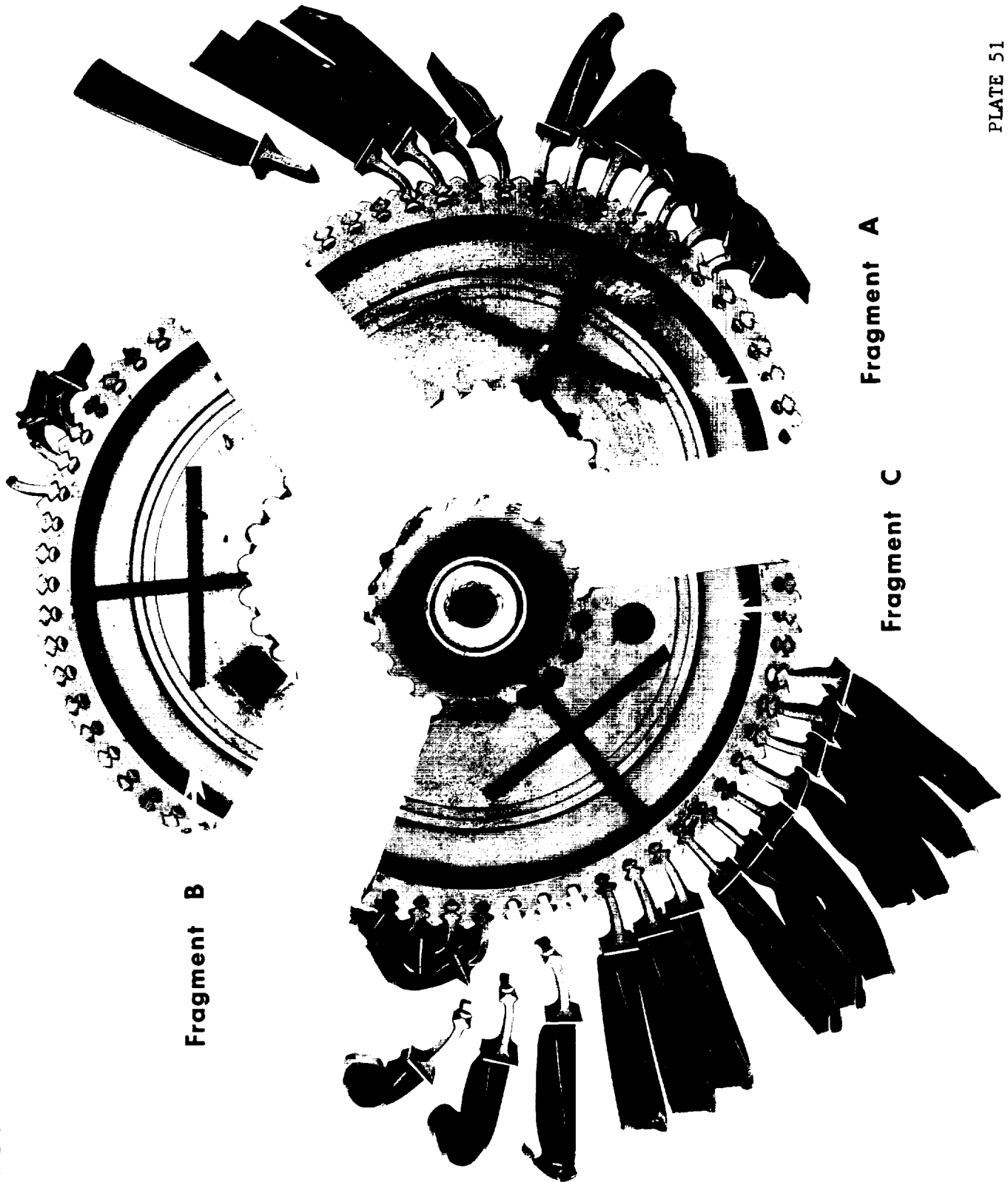


$t=290.0$

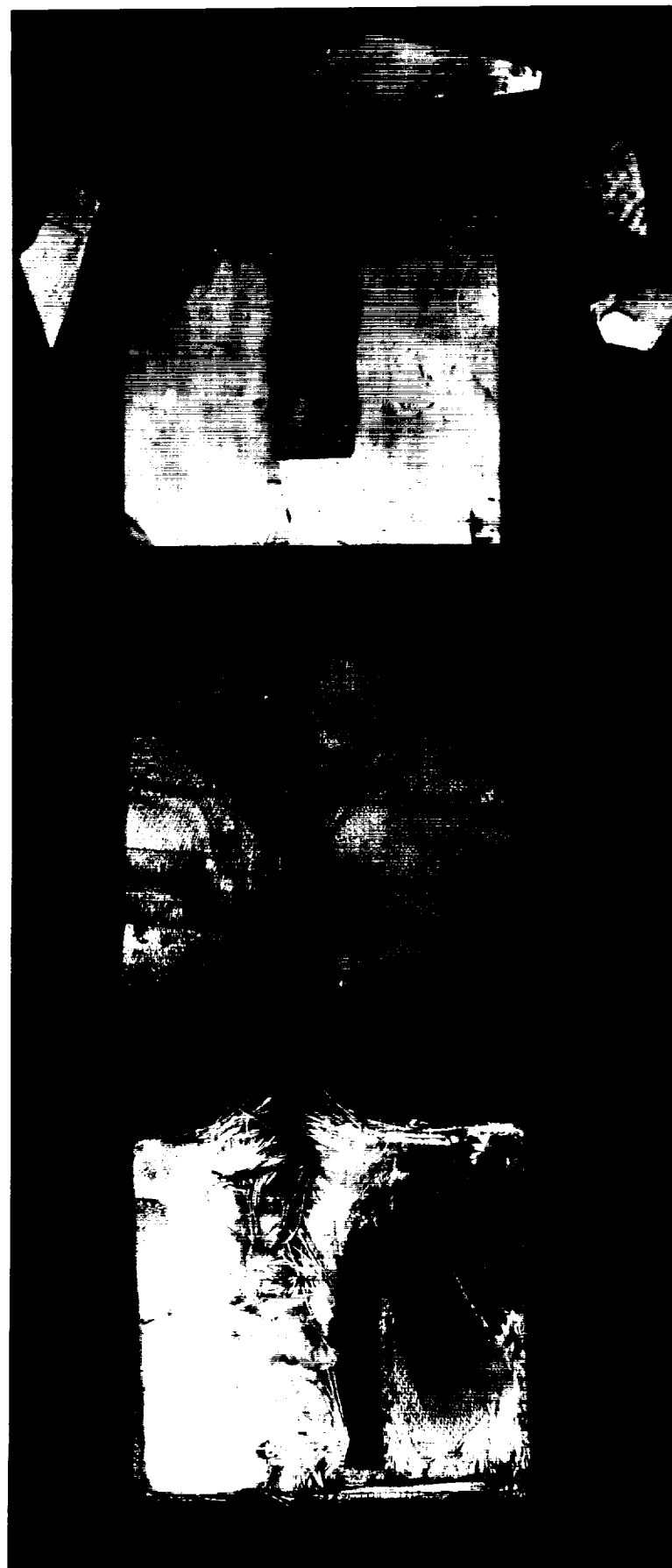
t =Time (microseconds) since first picture

FRAGMENT GENERATOR

POST-TEST NO. 17



POST-TEST NO. 17
DORON INSERTS & ALUMINA TILE



TEST NO. 17 DORON INSERTS

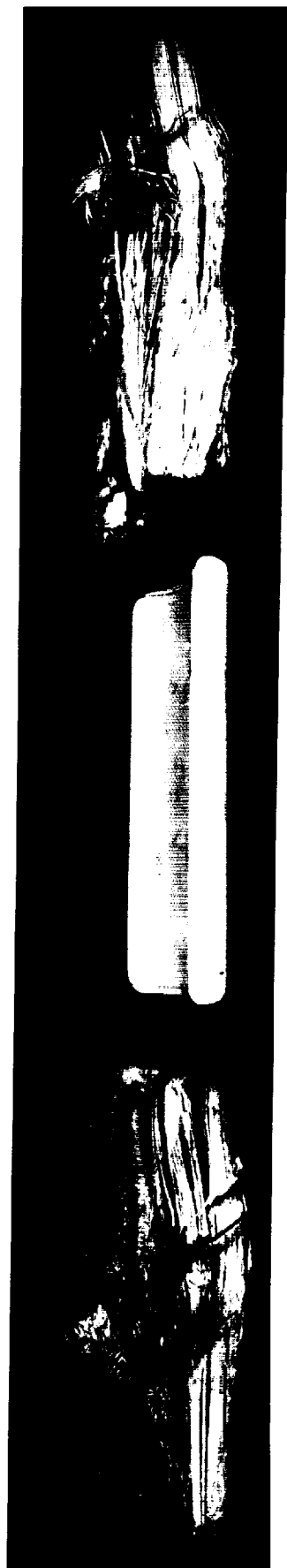


PHOTO NO: CAN-385073(L)-11-67

PLATE 53

PLATE 53

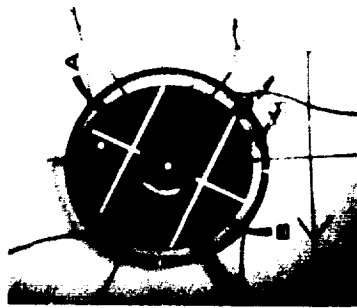
FRAGMENT SHAPE EFFECTS - DATA COMPILATION

Test Number		12	13	14	15	21
No. of Fragments		3	2	4	3	4
Outside Radius	R	3.50	3.50	3.50	3.50	3.50
Hub Radius	r	1.4375	1.4375	1.4375	2.80	1.4375
Radius Ratio	RR	0.411	0.411	0.411	0.800	0.411
Fragment Weight	lb.	1.178	1.768	0.884	0.490	0.884
Burst Speed	rpm	11900	15000	14750	14200	13380
Burst Speed	rad/sec	1246.2	1570.8	1544.6	1487.0	1401.2
KE _D	in - lb	50269	79870	77230	71578	63550
KE _{TOT} /KE _D	%	32.3	49.5	24.7	19.6	24.7
KE _{TOT}	in - lb	16237	39536	19076	14029	15697
KE _T /KE _D	%	21.1	18.7	18.7	13.4	18.7
KE _T	in - lb	10607	14936	14442	9591	11884
KE _R /KE _D	%	11.2	30.8	6.0	6.2	6.0
KE _R	in - lb	5630	24600	4634	4438	3813
KE _T /KE _{TOT}	%	65.3	37.5	75.8	68.5	75.8
Containment		1 pc. out	Yes	2 pcs. out	Yes	1 pc. out

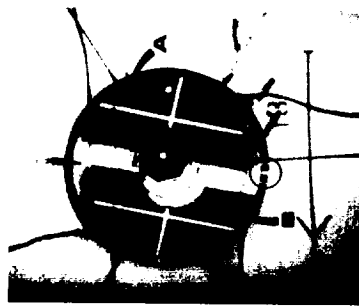
TEST NO. 13 FRAGMENT SHAPE EFFECTS-BI-HUB BURST

picture number:

13-0

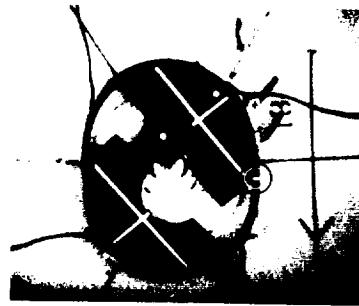


13-1



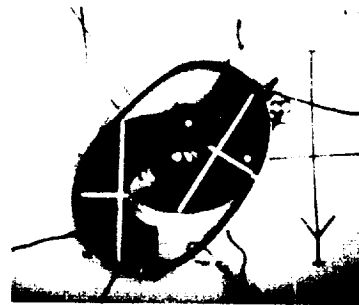
t=0

13-9



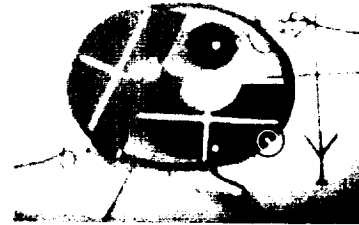
t=584

13-25



t=1752

13-49



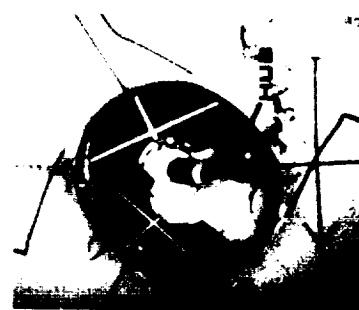
t=3504

13-73



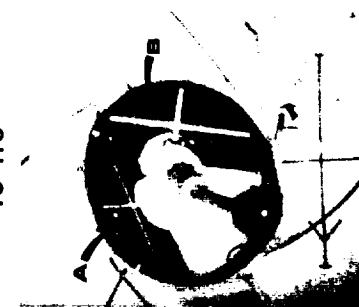
t=5256

13-87



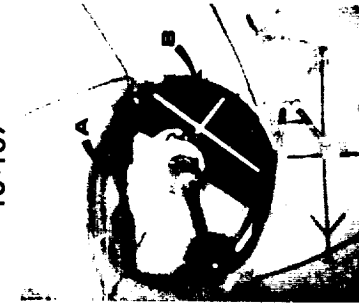
t=6279

13-113



t=8176

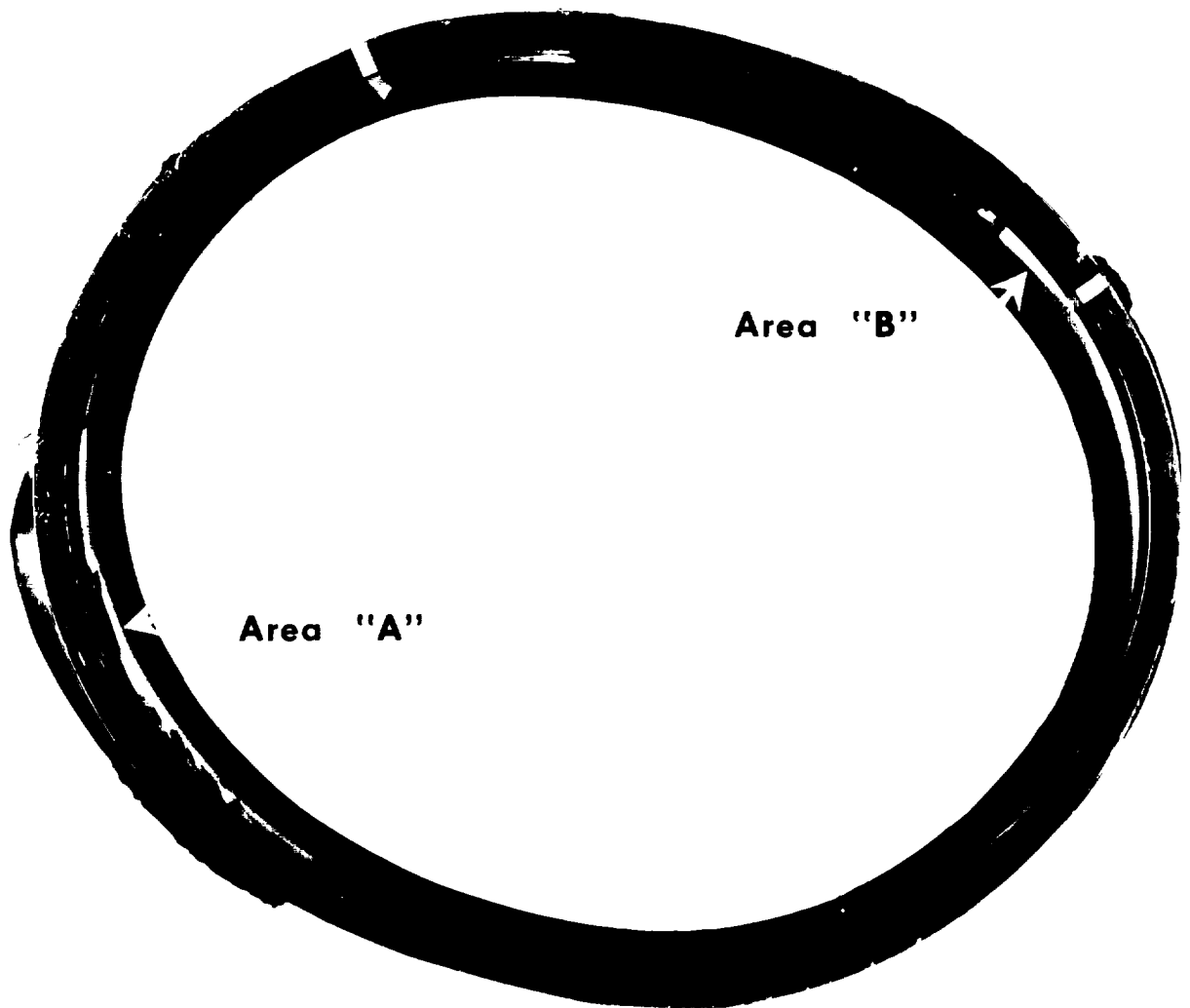
13-137



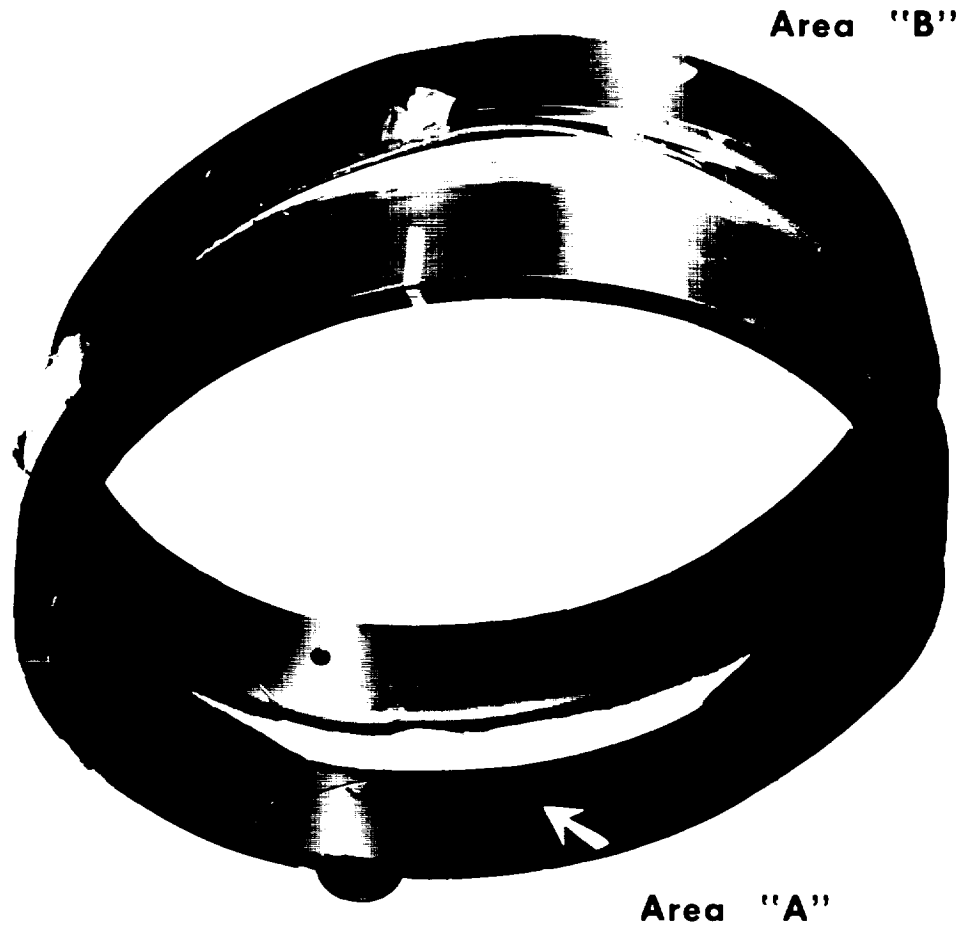
t=9928

t= Time (microseconds) since first picture

POST-TEST NO. 20
CONTAINMENT RING DISTORTION

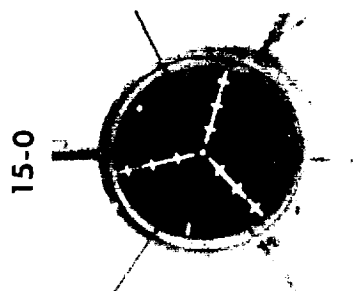


POST-TEST NO. 13
CONTAINMENT RING DETAIL OF OPENINGS



TEST NO. 15 FRAGMENT SHAPE EFFECTS-TRI-HUB RIM BURST

Picture number:



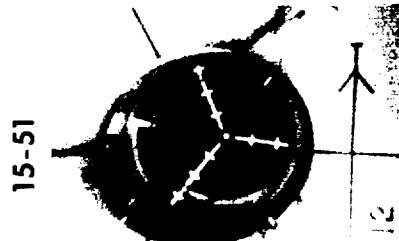
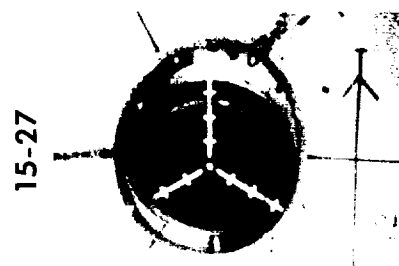
t=0

t=304

t=608

t=1064

t=1368



t=1976

t=3040

t=3496

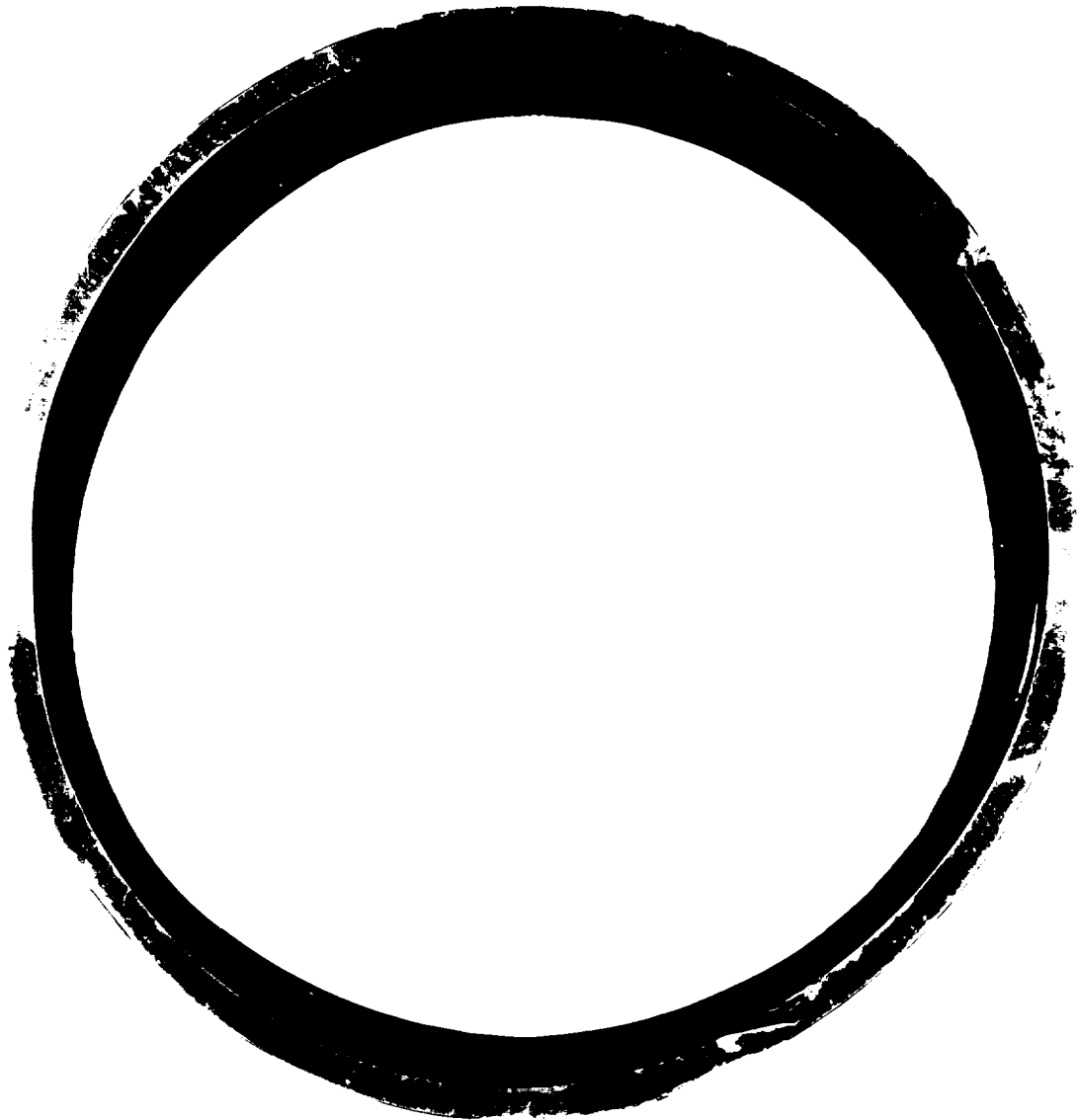
t=3800

t=4560

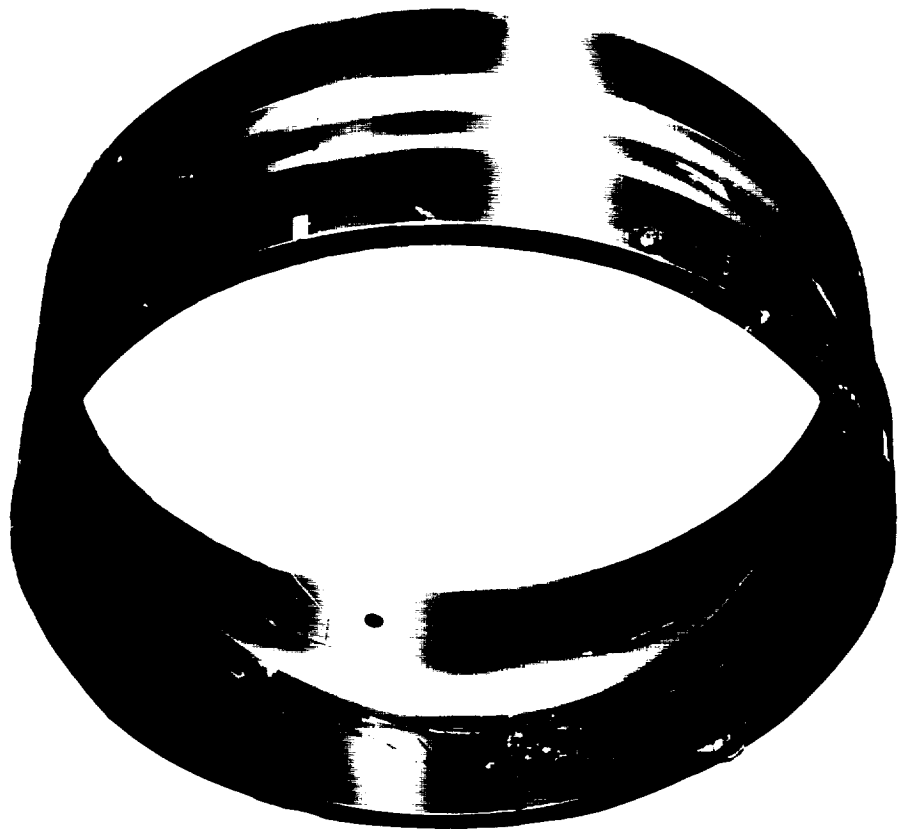
t=7448

t= Time (microseconds) since first picture

POST-TEST NO. 15 CONTAINMENT RING

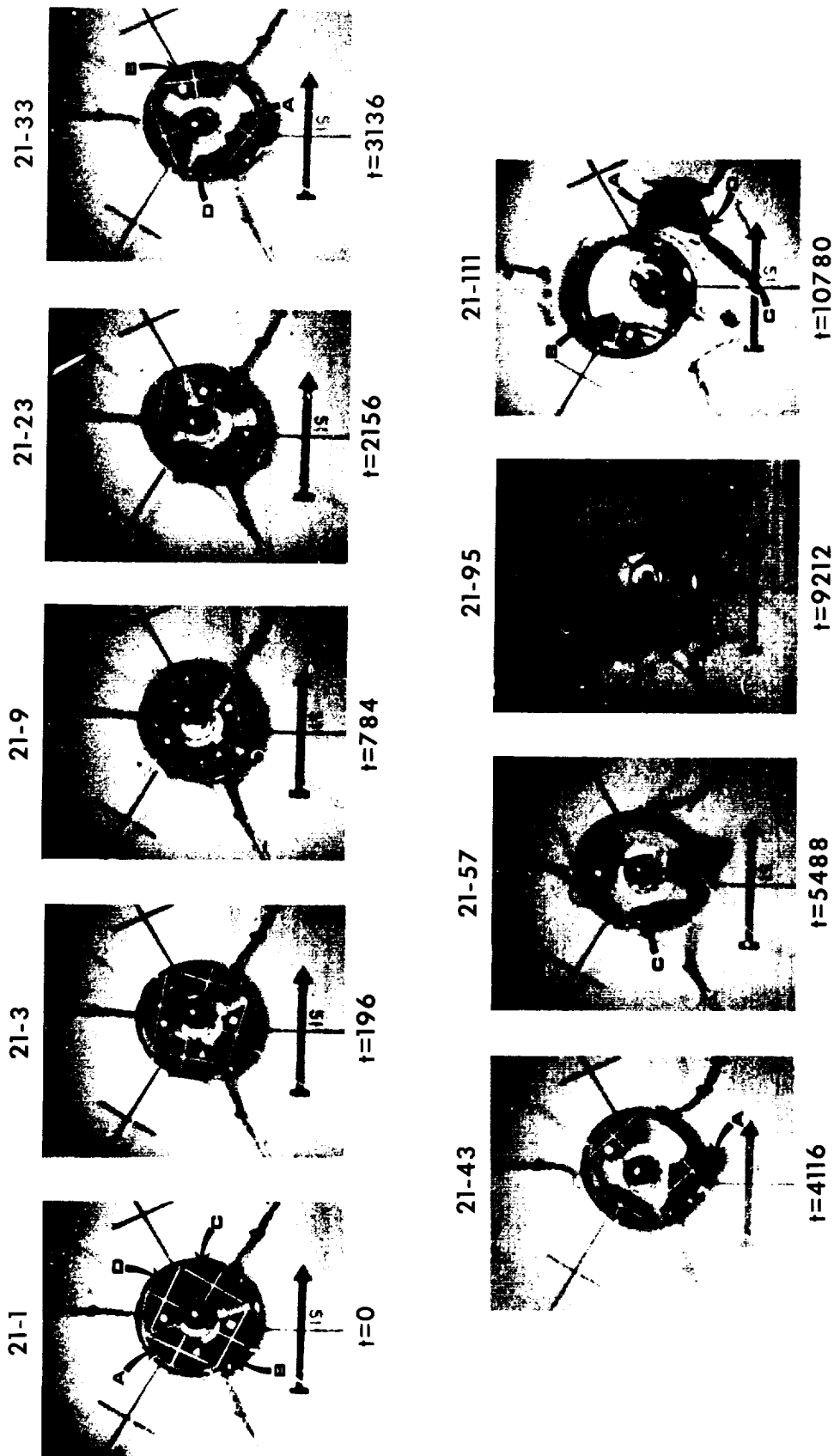


POST-TEST NO. 15
CONTAINMENT RING INDENTATION DETAILS



TEST NO. 21 FRAGMENT SHAPE EFFECTS-QUAD-HUB BURST

Picture number:



$t =$ Time (microseconds) since first picture

POST-TEST NO. 21 CONTAINMENT RING

Metal Curled Back



Strain Gage Epoxy

Serrated Edges

POST-TEST NO. 14 CONTAINMENT RING
OPENING "B" DETAIL

Opening "B"

Serrated Edges



Opening "A"

POST-TEST NO. 14 CONTAINMENT RING
OPENING "A" DETAIL

Opening "A"



Opening "B"

APPENDIX 1

A1-1

<u>TITLE</u>	<u>PLATE NO.</u>
Commercial Air Carriers' Jet Powered Aircraft Experience, 1962-1967 (Operating Hours & Powerplant Shutdowns)	1
Commercial Air Carriers' Jet Powered Aircraft Experience, 1962-1967 (Uncontained Failure Rate & Uncontained Failures)	2
Commercial Air Carriers' Jet Powered Aircraft, Experience, 1962-1967 (Failed Component Distribution)	3
U. S. Naval Aviation Jet Powered Aircraft Experience, FY1960-FY1966 (Operating Hours)	4
U. S. Naval Aviation Jet Powered Aircraft Experience, FY1960-FY1966 (Uncontained Failure Rate & Uncontained Failures)	5
U. S. Naval Aviation Jet Powered Aircraft Experience, FY1960-FY1966 (Failed Component Distribution)	6

U. S. COMMERCIAL AND U. S. NAVAL AVIATION JET-POWERED EXPERIENCE

The Aeronautical Engine Department has continued its survey of uncontained failures occurring in U. S. commercial air carrier and U. S. Naval aviation jet powered aircraft operations. Gas turbine powered aircraft are defined in this report to include all turbojet, turbofan, turboprop, and turboshaft powered aircraft. This survey was initiated as part of the Phase I program. The incident data presented herein has been obtained from two sources. The commercial data is abstracted from the "Summary of Mechanical Reliability Reports" (MRR) published daily by the Flight Standards Technical Division, FAA. Engine operating hours and shutdowns have been obtained from the "Aircraft & Engine Report" published monthly by the Flight Standards Technical Division, AC-700, Maintenance Branch, AC-730, FAA, P. O. Box 1082, Oklahoma City, Oklahoma 73101.

The U. S. Navy data is made available by the U. S. Naval Aviation Safety Center, Records and Statistics Dept., Naval Air Station, Norfolk, Virginia 23511. This data has been abstracted from a compilation of narrative briefs on aircraft mishaps involving compressor and/or turbine disk/blade failures as cause factors and from the yearly "USNASC Aircraft Accident Statistics Reports."

The data presented in this report is the latest information available to the AED as of 1 September 1967.

COMMERCIAL EXPERIENCE

The general comments concerning the accident failure statistics made in references a and b are still applicable. In addition, it should be noted that:

a. we define an uncontained failure as one that produces a fragment that penetrates the engine casing.

b. we are considering only gas turbine powered aircraft, i.e., turbofan, turboprop, and turboshaft.

c. the number of uncontained failures indicated here is the minimum number since we have only considered those incidents that were definitely documented to be uncontained.

The causes of failure are usually well documented but the resulting damage is in most instances not defined sufficiently to definitely determine containment.

Commercial air carriers are accumulating gas turbine powered engine operating experience at an ever increasing rate. This is shown on plate 1. The commercial air line operators are now averaging well over 1,000,000 jet engine operating hours per month. It is a favorable safety trend to note that the gas turbine engine power plant shutdowns (due to all causes) per 1000 turbine engine operating hours (lower portion of plate 1) has steadily decreased even though the usage rate continues to climb. The fact that the power plant shutdown rate is decreasing indicates that the overall engine design, operating practices, maintenance procedures, and failure sensing equipment are continually being

improved. But even with these technical gains, the number and/or rate of uncontained failures does not show a decreasing trend. The number of uncontained failures per million engine operating hours shown on plate 2 indicates an alarming trend upwards. The lower portion of this plate indicates the number of uncontained failures per calendar year. Within the time period investigated, 12 March 1962 to 1 September 1967, a total of 61 uncontained failures has been reported by the FAA. Since operating hours data are only available for the first four months of 1967 at this writing, only the eight uncontained failures that occurred during this four-month period have been used in computing the uncontained failure rate.

The uncontained failure problem has not plagued just a few airline operators or particular aircraft types. Of the 61 incidents reported, 13 airlines have been involved and 11 different aircraft. The extent of damage reported ranges from just a few holes in the engine cowlings to a loss to one aircraft of one engine and a 28 ft section of the outer wing panel.

What engine components are failing and leaving the casing to cause more damage? A breakdown of these components is shown on plate 3. Note the problem is not isolated to one particular item.

U. S. NAVAL AVIATION EXPERIENCE

A review of USN data indicates similar patterns as noted with the US commercial data. The usage rate, shown on plate 4, is seen to be continually increasing to over 3,000,000 engine operating hours in fiscal year 1966. Plate 5 shows the uncontained failure rate decreasing for fiscal year 1960 to fiscal year 1963 but has since reversed itself and is on the climb. The lower portion of plate 5 illustrates the yearly distribution of definite uncontained failures. A total of 33 such failures has been reported. The Navy uncontained failure problem, similar to the commercial experience, is not isolated to one particular powerplant component. The distribution of component cause factors is shown on plate 6.

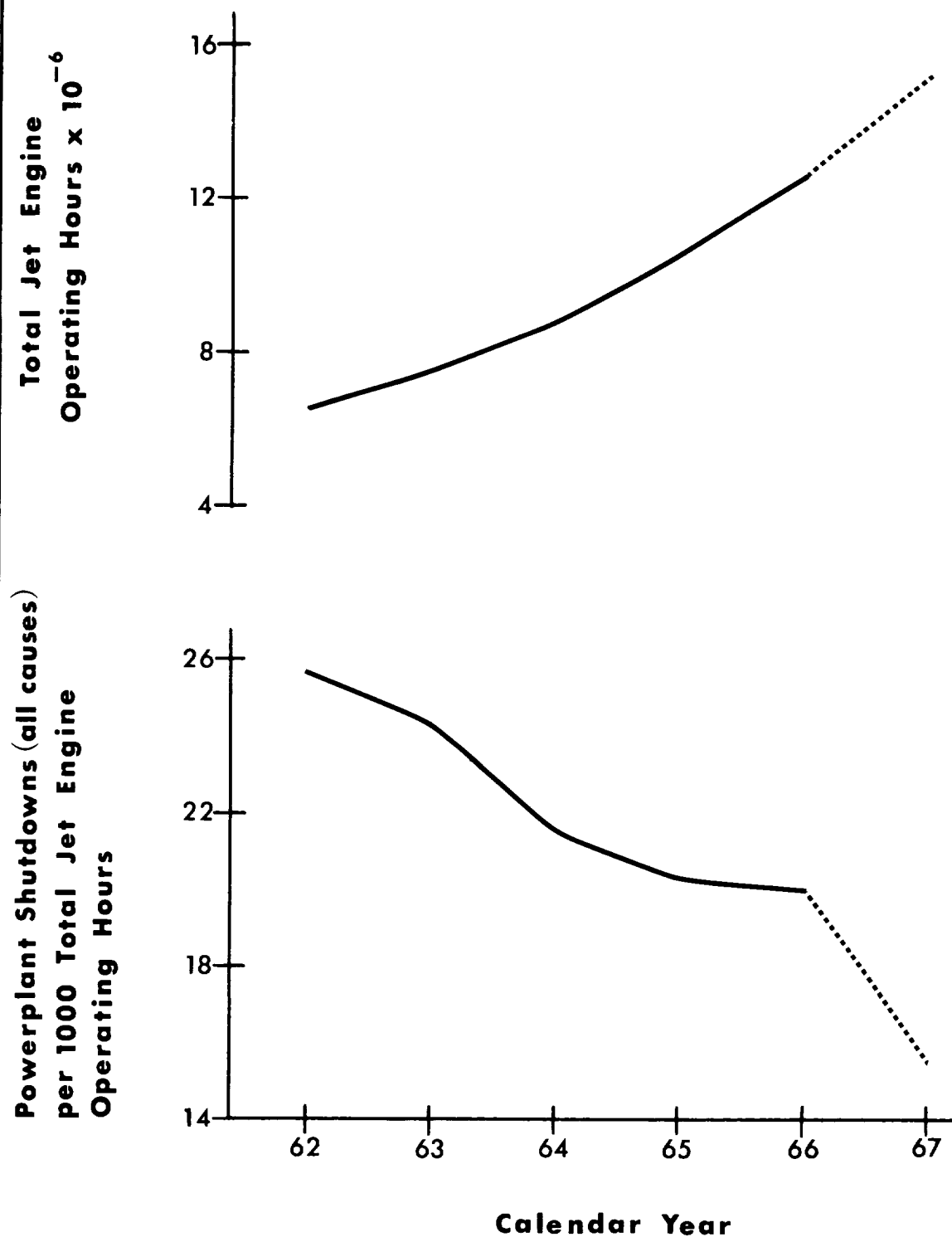
Both the US commercial and Naval aviation data give evidence to the fact that uncontained failures present an ever increasing danger to the operational safety of turbomachinery. The possible catastrophic proportions of this problem demand a rapid solution.

REFERENCES

- a. Martino, Albert A., "Turbine Disk Burst Protection Study - Phase I - Final Report on P. A. NASA DPR R-105", NAEC-AEL Report No. 1793, 31 March 1965
- b. Martino, A. A. and Mangano, G. J., "Turbine Disk Burst Protection Study - Final Phase II-III Report on P. A. NASA DPR R-105", NAEC-AEL Report No. 1848, 28 February 1967.

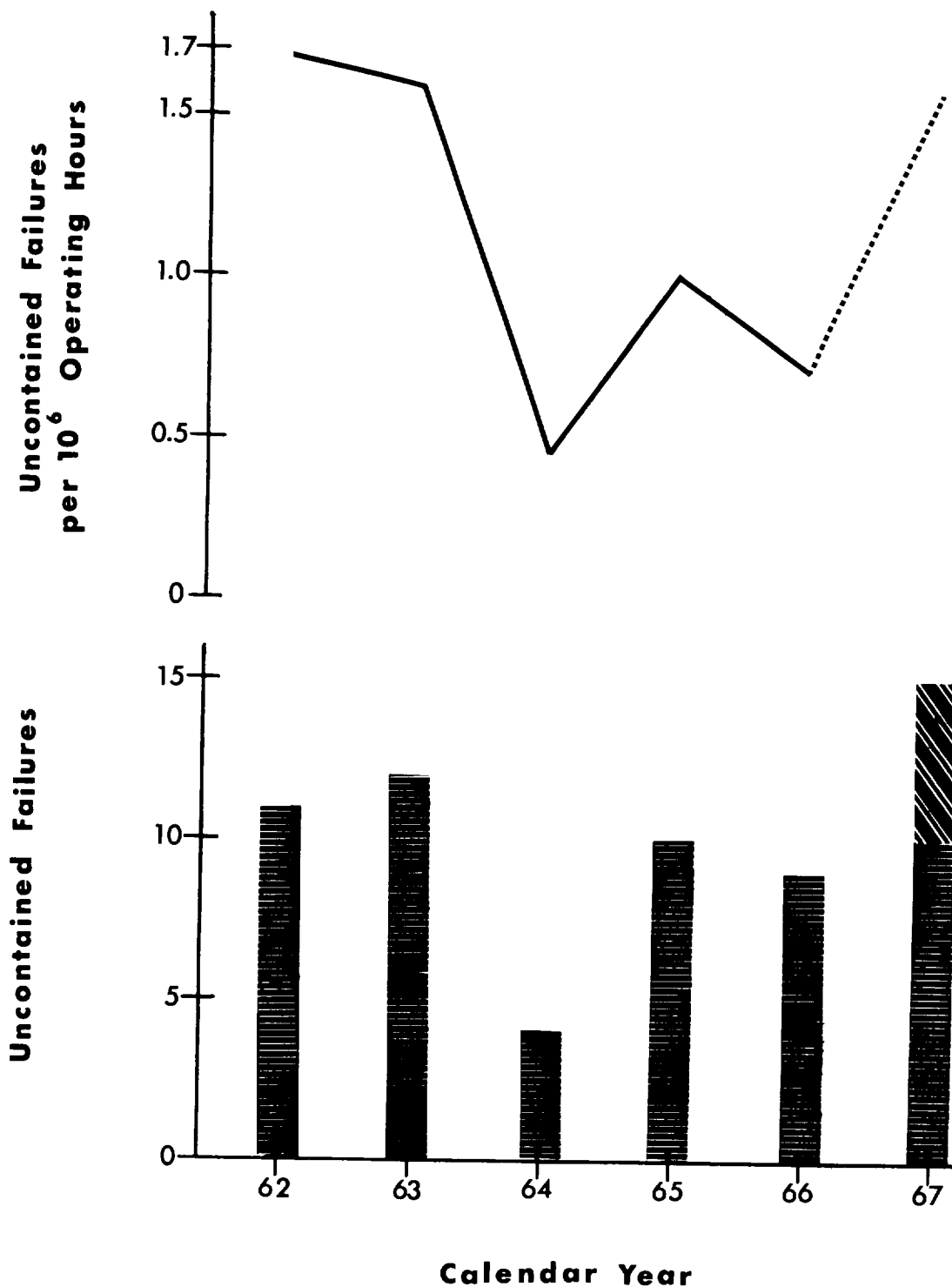
**COMMERCIAL AIR CARRIERS'
JET POWERED AIRCRAFT EXPERIENCE
1962 - 1967**

Operating Hours and Powerplant Shutdown Rate



**COMMERCIAL AIR CARRIERS'
JET POWERED AIRCRAFT EXPERIENCE
1962 - 1967**

Uncontained Failure Rate and Uncontained Failures



**COMMERCIAL AIR CARRIERS'
JET POWERED AIRCRAFT EXPERIENCE
1962 - 1967**

Failed Component Distribution

BLADES	TURBINE	3	4	0	3	1	2	13
	COMPRESSOR	1	0	2	1	1	4	9

SPACERS	TURBINE	4	3	0	0	0	0	7
	COMPRESSOR	0	3	1	0	0	0	4

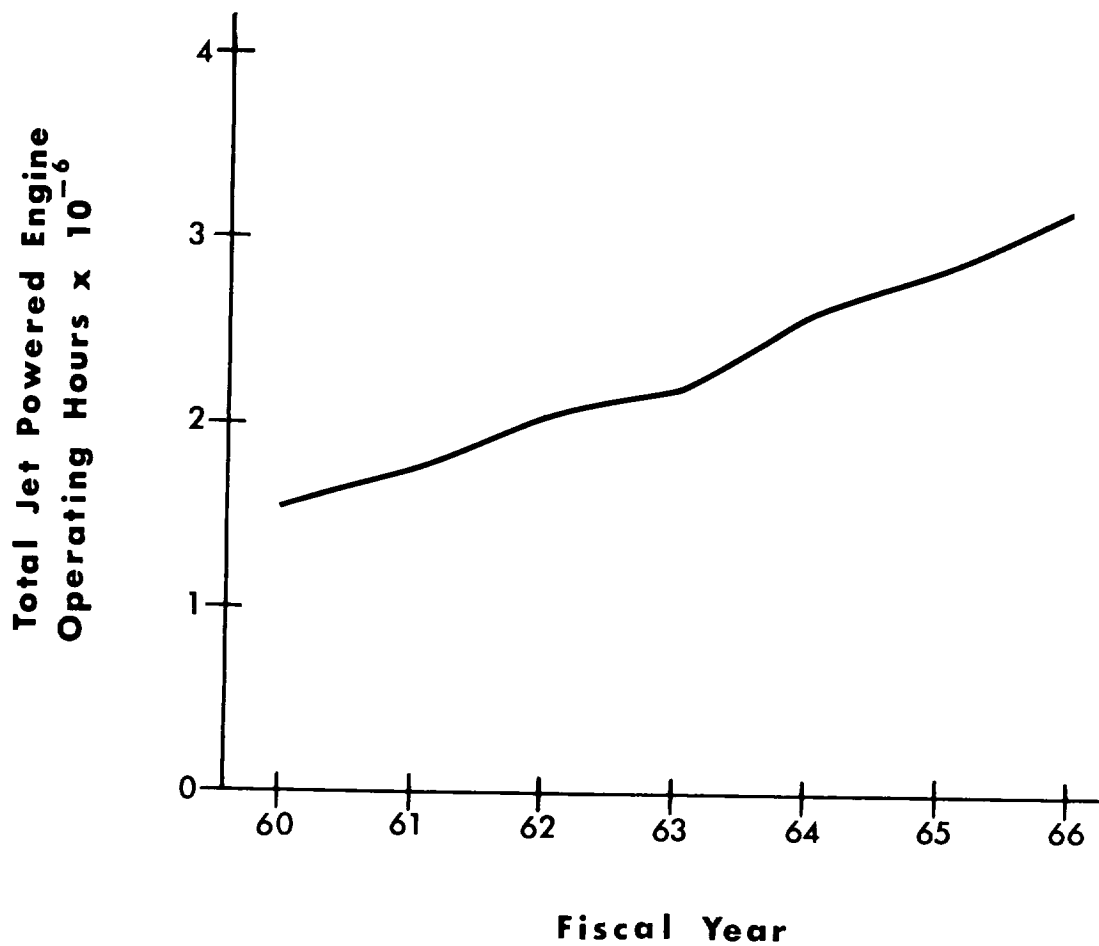
DISKS	TURBINE	1	0	0	3	4	2	10
	COMPRESSOR	2	2	1	3	3	7	18

62	63	64	65	66	67
----	----	----	----	----	----

CALENDAR YEAR

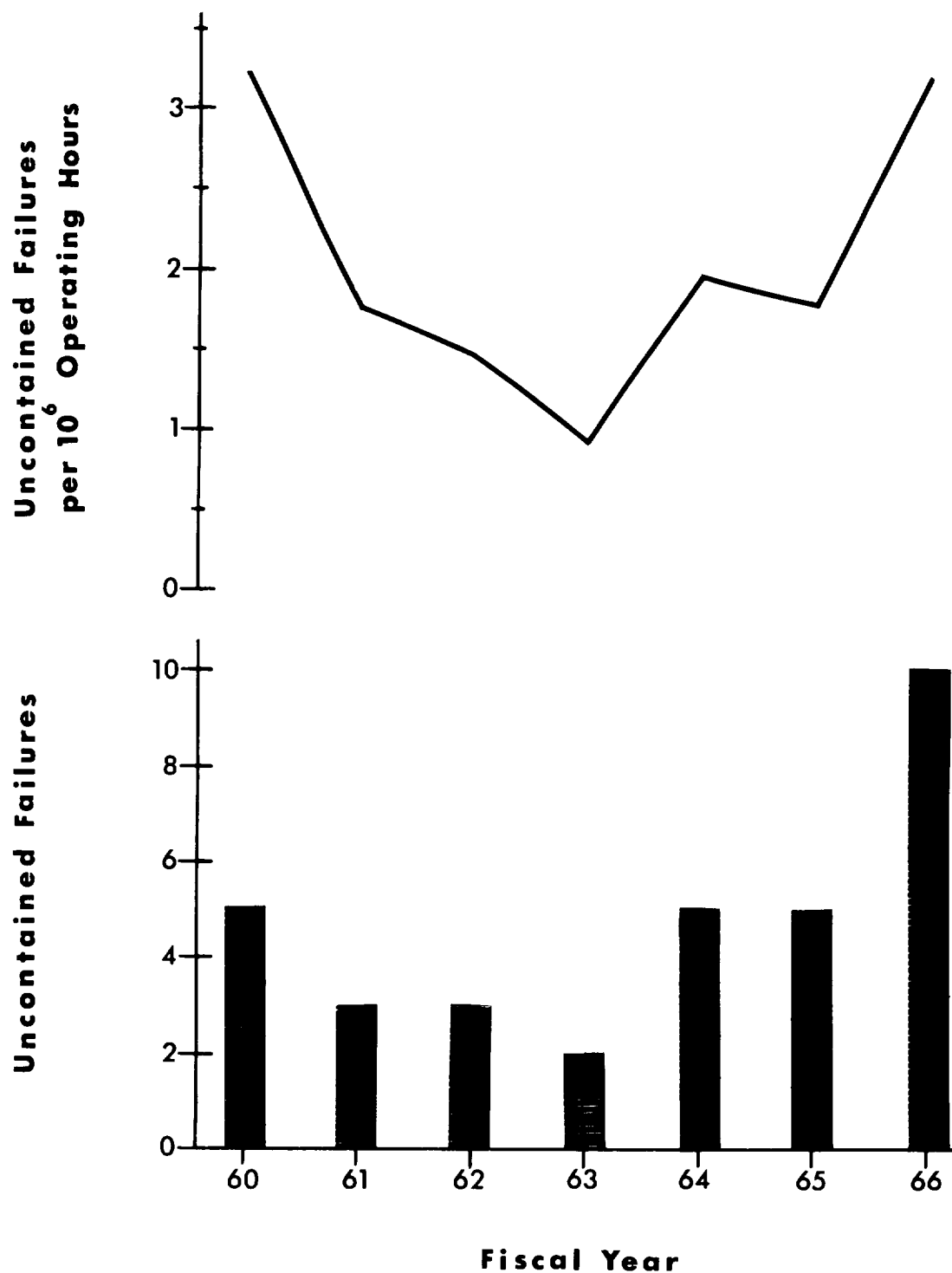
**U.S. NAVAL AVIATION
JET POWERED AIRCRAFT EXPERIENCE
FY 1960 - FY 1966**

Operating Hours



**U.S. NAVAL AVIATION
JET POWERED AIRCRAFT EXPERIENCE
FY 1960 - FY 1966**

Uncontained Failure Rate and Uncontained Failures



**U.S. NAVAL AVIATION
JET POWERED AIRCRAFT EXPERIENCE
FY 1960 — FY 1966**

Failed Component Distribution

BLADES	TURBINE	2	1	0	1	3	3	4	14
	COMPRESSOR	0	0	0	0	0	0	2	2
SPACERS	TURBINE	0	0	1	0	0	0	1	2
	COMPRESSOR	1	0	0	1	1	0	0	3
DISKS	TURBINE	1	2	1	0	1	1	1	7
	COMPRESSOR	1	0	1	0	0	1	2	5
		60	61	62	63	64	65	66	

FISCAL YEAR

APPENDIX 2

A2-1

LIST OF PLATES

<u>TITLE</u>	<u>PLATE NO.</u>
Ideal Rotating System	1
Centroid of the Area of a Circular Sector	2
Total Kinetic Energy of a Fragment (KE_{TOT}/KE_D) Versus Fragment Included Angle ($\Delta\theta$)	3
Translational Kinetic Energy of a Fragment (KE_T/KE_D) Versus Fragment Included Angle ($\Delta\theta$)	4
Rotational Kinetic Energy of a Fragment (KE_R/KE_D) Versus Fragment Included Angle ($\Delta\theta$)	5
Translational Portion of the Total Fragment Energy (KE_T/KE_{TOT}) Versus Fragment Included Angle ($\Delta\theta$)	6
Total Kinetic Energy of a Fragment (KE_{TOT}/KE_D) Versus Fragment Radius Ratio (R_R)	7
Translational Kinetic Energy of a Fragment (KE_T/KE_D) Versus Fragment Radius Ratio (R_R)	8
Rotational Kinetic Energy of a Fragment (KE_R/KE_D) Versus Fragment Radius Ratio (R_R)	9
Translational Portion of the Total Fragment Energy (KE_T/KE_{TOT}) Versus Fragment Radius Ratio (R_R)	10

LIST OF SYMBOLS

t	= Uniform thickness of disk
γ	= Weight density of disk material
ω	= Rotational speed of disk
ω_b	= Disk burst speed
r	= Radius of circular hub section
R	= Outer radius of the disk
R_R	= Radius ratio (r/R)
E_{TOT}	= Total kinetic energy of a rigid body
E_t	= Translational kinetic energy of a rigid body
E^*	= Rotational kinetic energy relative to the center of mass
I_O	= Moment of inertia of a disk with respect to the center of mass axis
I	= Moment of inertia of an annular sector fragment about the axis of rotation of the disk
ρ	= Mass density of disk material
M	= Total mass of the disk
KE_D	= Kinetic energy of the "whole" disk
KE_H	= Kinetic energy of the hub section of the disk
I_{oh}	= Moment of inertia of the hub
M_h	= Mass of the hub
KE_{TOT}	= Total kinetic energy of an individual fragment
KE_R	= Rotational kinetic energy of an individual fragment
KE_T	= Translational kinetic energy of an individual fragment
$\Delta\theta$	= Included angle of a fragment
N	= Number of equally-sized annular sector fragments
\bar{R}_c	= Radial distance to fragment's center of mass
M_f	= Mass of the fragment

Whenever the subject of containment is discussed, the term "energy" is used.

"How much energy must be contained or controlled?"

"A projectile has how much energy upon impact?"

"A target material can absorb "x" ft/lb of energy."

These questions and statements are all familiar and important to the containment engineer. The energy possessed by the attacking fragments, and the energy absorbing capacity of the containment material and/or device are very dominant factors in an analysis of any containment system.

The energies related to a fragment from a failed turbomachine rotor are much more complex than the energies considered when studying a bullet penetrating a target material. This latter field has received much attention in the past, whereas the former has not been studied with the vigor necessary to substantially aid in the solution of containment problems.

During the AED's investigation into various containment practices, it was noted that many failed to realize, or considered as insignificant, the fact that the fragments from a rotor burst possess rotational as well as translational energy. In order to clarify this concept and present data concerning the comparative magnitudes of these energies for an ideal disk, the following development is presented.

The following assumptions have been made (see plate 1 for illustration of ideal system):

(1) An unbladed disk is of uniform thickness (t) and is composed of a material having a constant weight density (γ).

(2) The disk is suspended by a weightless rod from the underside of a motor and rotates in one plane.

(3) The motor is capable of operating at any constant speed (ω).

(4) At the failure speed, all fragments instantaneously break away from the disk and travel in the original plane of rotor rotation.

(5) The fragments do not interact with one another after failure.

(6) All fragments are sector shaped.

The most general disk that will be considered is one with a "central hole." This "central hole" is physically the hub section of the disk. The radius of the hub is r . The remaining annulus section of the disk is considered to fragment in an equal number of annular sectors. The hub section remains intact and connected to the drive spindle. The more specific case also to be discussed will be when the inner radius of the annulus (r) becomes zero and the disk is considered to be "whole" or one piece. When this "whole" disk ideally fragmentizes, an equal number of pie-shaped sector fragments will be produced.

The ratio of the inner radius of the annulus (r) to the outer radius of the annulus (R) can be defined as the radius ratio (R_R). This dimensionless parameter will be used throughout this development.

As in the case of any arbitrary collection of particles, the total kinetic energy of a rigid body (E_{TOT}) can be expressed as equation (1) (reference a).

$$E_{TOT} = E_t + E^* \quad (1)$$

where

E_t = Translational kinetic energy

$$E_t = \frac{1}{2}MV^2 \quad (2)$$

M = Total mass of the body

V = Center of mass velocity

E^* = Rotational kinetic energy relative to the center of mass

The first term of equation (1) is associated with the motion of the center of mass of the body, and the second term with the motion relative to the center of mass. In the case of a rigid body this latter motion is a rotation. Rotational kinetic energy can be expressed in terms of the moment of inertia about this axis of rotation as follows:

$$E^* = \frac{1}{2}\omega^2 \int r^2 dM \quad (3)$$

$$E^* = \frac{1}{2}I_0\omega^2 \quad (4)$$

I_0 is the moment of inertia of the body with respect to the center of mass axis perpendicular to the plane of motion. Therefore the total kinetic energy of a rigid body moving in a plane can then be expressed as

$$E_{TOT} = \frac{1}{2}MV^2 + \frac{1}{2}I_0\omega^2 \quad (5)$$

Since the disk ideally experiences no transverse movement, the translational portion of equation (5) is equal to zero. The total energy of the disk is therefore just the rotational energy of the disk as determined by equation (4).

The moment of inertia of an annular sector fragment about the axis of rotation of the disk can be derived as follows:

$$I = \int_M r^2 dM \quad (6)$$

$$dM = r dr d\theta t \rho \quad (7)$$

$$I = \int_{\theta_1}^{\theta_2} \int_{r_1}^{r_2} r^2 (r dr d\theta t \rho)$$

$$I = t \rho \int_{\theta_1}^{\theta_2} \int_{r_1}^{r_2} r^3 dr d\theta$$

$$I = \frac{t \rho}{4} \int_{\theta_1}^{\theta_2} (R^4 - r^4) d\theta$$

$$I = \frac{t \rho}{4} (R^4 - r^4) (\theta_2 - \theta_1)$$

$$I = \frac{t \rho}{4} (\theta_2 - \theta_1) \left[(R^2 - r^2)(R^2 + r^2) \right] \quad (8)$$

The kinetic energy of a complete annular sector rotating about its center of mass can be determined using equations (4) and (8).

$$E^* = \frac{1}{2} \omega^2 \left[\frac{t \rho}{4} (2\pi) (R^2 - r^2) (R^2 + r^2) \right]$$

$$E^* = \frac{t \rho \omega^2 \pi}{4} (R^2 - r^2) (R^2 + r^2) \quad (9)$$

Equation (9) can be rewritten in terms of the radius ratio (R_R) as

$$E^* = \frac{t \rho \omega^2 \pi R^4}{4} (1 - R_R^4) \quad (9a)$$

For the specific case of a whole disk ($r = 0$, and $\Delta\theta = 2\pi$) equation (8) reduces to

$$I_O = \frac{1}{2} M R^2$$

where M is the total mass of the disk.

The kinetic energy of a "whole" disk (KE_D) rotating at a speed (ω) is therefore:

$$KE_D = \frac{1}{2} I_O \omega^2 = \frac{1}{2} M(R\omega)^2 \quad (10)$$

In order to generalize the results of this development and make it applicable to all size disks of uniform thickness and all speeds, we have normalized the energy components developed by dividing through by the kinetic energy of the "whole" disk (KE_D). All energies being relative to this same rotational speed.

The quantity of kinetic energy possessed by the disk just prior to burst must be conserved by all the fragments after the burst; i.e., the sum of the rotational and translational kinetic energy of all the fragments must equal the kinetic energy of the disk at burst speed. This assumes no energy losses incurred during fragment separation.

Under the ideal conditions being considered, the energy of the entire annulus section is equally distributed to all the individual annular sector fragments. The hub section is considered to remain rotating at the burst speed (ω_b) and therefore possesses a definite amount of kinetic energy (KE_H) which is all rotational energy. KE_H can be determined as follows:

$$KE_H = \frac{1}{2} I_{OH}(\omega_b)^2 \quad (11)$$

Where:

I_{OH} = moment of inertia of the hub

$$I_{OH} = \frac{1}{2} M_H r^2 \quad (12)$$

M_H = mass of the hub

Therefore,

$$KE_H = \frac{1}{2} M_H (\omega_b)^2$$

We define the total kinetic energy of an individual fragment (KE_{TOT}), as the summation of the rotational and translational energies possessed by the fragment immediately after failure. These fragments are generated when the annulus section fragmentizes.

$$KE_{TOT} = KE_R + KE_T \quad (13)$$

Where:

KE_R = rotational kinetic energy of an individual fragment and

KE_T = translational kinetic energy of an individual fragment.

Summarizing the previous paragraphs it can be said that the kinetic energy of the entire disk (KE_D) is equal to the summation of the total kinetic energy of the individual fragments plus the kinetic energy of the hub.

$$KE_D = KE_H + \sum (KE_{TOT}) \quad (14)$$

A total kinetic energy of an individual fragment having an annular sector shape (KE_{TOT}) can be determined by dividing the kinetic energy of a complete annular sector (E^*) given by equation (9), by the

number of equal fragments (N) generated. The included angle of each fragment ($\Delta\theta$) will be

$$\Delta\theta = \frac{2\pi}{N}$$

The kinetic energy is therefore:

$$KE_{TOT} = \frac{t\rho\omega^2(\Delta\theta)}{8} (R^4 - r^4) \quad (16)$$

or incorporating the radius ratio term

$$KE_{TOT} = \frac{t\rho\omega^2(\Delta\theta)R^4}{8} (1 - R_R^4) \quad (16a)$$

Let us first consider the translational kinetic energy associated with a fragment released from a failed rotor.

In general, the kinetic energy of a particle of mass (m) traveling on a straight path with a velocity (v) is equal to $(\frac{1}{2})mv^2$. When related to a fragment as the one being considered, the straight path followed by the fragment is described by a line drawn perpendicular to a radial line from the center of the rotor to the center of mass of the fragment and passing through this center of mass in the direction of rotation.

The center of mass of the fragment from a whole disk can be determined as in reference b.

Since we are considering a disk of uniform thickness, the center of mass is located along the axis of symmetry of the circular sector (refer to plate 2) and the centroid of the area, or essentially the center of mass of the circular sector, is located at

$$\bar{R} = \frac{4R}{3} \cdot \frac{\sin \frac{\theta}{2}}{\theta} \quad (17)$$

For the general case of a disk with a "central hole" the given area can be divided into parts, the centroid of each part being known, and then the moment of the total area will be the sum of the moments of the area of its parts. The centroid of the composite figure (\bar{R}_C) is determined by applying the following equation:

$$\bar{R}_C = \frac{A_R \bar{R} - A_r \bar{r}}{A_R - A_r} \quad (18)$$

The terms of equation (18) are defined on plate 2.

Equation (18) reduces to the following:

$$\bar{R}_C = \left[\frac{4}{3} \cdot \frac{\sin \frac{\theta}{2}}{\theta} \right] \left[\frac{R^3 - r^3}{R^2 - r^2} \right] \quad (19)$$

Utilization of the radius ratio (R_R) further reduces equation (19) to:

$$\bar{R}_c = \left[\frac{4R \sin \frac{\theta}{2}}{3\theta} \right] \left[\frac{1 - R_R^3}{1 - R_R^2} \right] \quad (19a)$$

The entire mass of the fragment (M_f), which is assumed to act at the center of mass, is equal to the product of the area of the annulus sector ($A_R - A_r$), the material mass density (ρ), and the disk thickness (t).

$$M_f = (A_R - A_r)(\rho)(t) \quad (20)$$

$$M_f = \frac{\theta \rho t}{2} (R^2 - r^2) \quad (21)$$

Again incorporating the R_R term, equation (21) becomes

$$M_f = \frac{\theta \rho t R^2}{2} (1 - R_R^2) \quad (21a)$$

The fragment mass (M_f) acting at the center of mass has a tangential velocity $V_T = \bar{R}_c \cdot \omega_b$

The translational kinetic energy of the fragment is therefore

$$KE_T = \frac{1}{2} \cdot M_f \cdot (V_T)^2$$

$$KE_T = \frac{t \rho \omega^2 R^4}{4} \cdot \frac{16 \sin^2 \left(\frac{\theta}{2} \right) (1 - R_R^3)^2}{9\theta (1 - R_R^2)} \quad (22)$$

The rotational kinetic energy of the individual fragment (KE_R) can be determined by subtracting the translational kinetic energy of the fragment (KE_T), equation (22), from the total energy (KE_{TOT}) of the fragment equation (16).

As mentioned previously, each of the energy terms can be normalized by ratioing them to the kinetic energy of the entire disk (KE_D). These normalized parameters are:

$$\frac{KE_{TOT}}{KE_D} = \frac{(\Delta\theta) (1 - R_R^4)}{2\pi} \quad (23)$$

$$\frac{KE_T}{KE_D} = \frac{16 \sin^2\left(\frac{\theta}{2}\right) (1 - R_R^3)^2}{9 \pi (\Delta\theta) (1 - R_R^2)} \quad (24)$$

$$\frac{KE_R}{KE_D} = \frac{KE_{TOT} - KE_T}{KE_D} \quad (25)$$

$$\frac{KE_T}{KE_{TOT}} = \frac{2 \left[4 \sin\left(\frac{\theta}{2}\right) \right]^2}{3\theta} \cdot \frac{(1 - R_R^3)^2}{(1 - R_R^4)(1 - R_R^2)} \quad (26)$$

A computer program, developed by the Data Acquisition and Processing Group, at the AED, (reference c) produced the graphical representation of equations (23 to 26). The normalized parameters (KE_{TOT}/KE_D , KE_T/KE_D , KE_R/KE_D , KE_T/KE_{TOT}), are plotted against the included angle of the sector shaped fragment for a family of radius ratios on plates 3, 4, 5, and 6, respectively; and against the radius ratios for a family of constant included sector angles on plates 7, 8, 9, and 10, respectively;

These curves can be used to determine the energy distribution of a fragment from a failed flat disk of uniform thickness or to assist in the design of containment/control system evaluation tests.

FRAGMENT TOTAL ENERGY

The percentage of the total disk energy possessed by individual fragment can be determined by plate 3 and/or 7.

The magnitude of the total energy per fragment (for a constant radius ratio condition) increases as the included angle of the fragment is increased. Another way of looking at this is to say that the total energy per fragment ($R_R = \text{constant}$) decreases as the number of symmetric fragments produced by the disk failure increases.

The rate at which the total energy per fragment changes with respect to a given incremental change in the included angle of the fragment ($R_R = \text{constant}$) is a constant; and this rate is independent of the magnitude of the radius ratio.

The rate at which the total energy per fragment changes with respect to a given incremental change in the radius ratio of a fragment ($\Delta\theta = \text{constant}$) is a constant; this rate is independent of the magnitude of the included angle of the fragment.

When a disk fails such that there is no remaining hub section, i.e., $R_R = 0$, the energy of the disk is equally distributed to all fragments. This distribution, represented by the uppermost curve on plate 3, shows that a tri-hub burst ($R_R = 0$) produces three fragments each having a total energy of 33.33% of the disk's energy; while an eight-piece burst produces fragments each possessing 12.50% of the disk energy just prior to failure.

For a disk failure that produces annular sector fragments plus a remaining hub section, the total energy per fragment is not as easily

calculated. A disk failure having a $R_R = 0.8$ approaches a condition frequently referred to as a "rim failure", the fragments are portions of a thin ring of material at the outer edge of the disk while the remaining hub section is a comparatively large section of the original disk. For this type of disk failure ($R_R = 0.8$), a tri-hub burst would produce three fragments each having a total energy of 19.6% of the original disk energy. For a three-piece failure ($R_R = 0.8$), the total energy per fragment is only 7.3% of that energy possessed by the complete disk prior to failure.

FRAGMENT TRANSLATIONAL KINETIC ENERGY

Let us now examine the translational kinetic energy of a fragment from a failed disk. From plate 4 it can be seen that the maximum translational kinetic energy of a fragment always occurs when a fragment has an included angle of 0.742 radians (133.56°) regardless of the radius ratio. Maximum translational kinetic energy always occurs when the radius ratio is equal to 0.366. This is also evident when you review plate 8 and observe that the maximum value of KE_T/KE_D for all values of the included angle of the fragment occur at $R_R = 0.366$. The uppermost curve on plate 4 is for a value of $R_R = 0.366$. It can therefore be determined that a fragment having a $R_R = 0.366$ and an included angle of 133.56° will possess the maximum amount of translational kinetic energy that a fragment from a failed disk of uniform thickness can possess the instant after failure. The magnitude of this maximum translational kinetic energy is 21.4% of the total energy of the disk.

Further investigation into the energy distribution of this unique fragment that possesses the maximum translational kinetic energy per fragment shows that the total energy of this fragment is 36.3% of the entire disk (plate 7, $R_R = 0.366$) and it has a rotational kinetic energy component of 14.9% (plate 9, $R_R = 0.366$). It should be noted that the sum of the fragment's translational kinetic energy (0.214) and rotational kinetic energy (0.149) does equal the total kinetic energy of the fragment (0.363).

Inspection of plate 10 indicates that the portion of the total energy of the fragment attributed to translation increases as the radius ratio increases, i.e., as the fragment becomes a part of a thinner and thinner ring. Plate 6 also shows the increased translational component of the total fragment energy. Plate 6 indicates that as the disk failure produces more symmetric fragments, the translational kinetic energy becomes a larger portion of the total fragment energy. Theoretically, fragment energy is all translational when the radius ratio approaches 1.0 and there are infinite number of fragments resulting from this failure.

AED TRI-HUB BURST ENERGY DISTRIBUTION

The first series of tests conducted at the AED Containment Evaluation Facility were made to study the basic kinematics of a tri-hub burst. The following exercise presents an approach to the use of these curves to determine the type and magnitude of energy possessed by the fragments of one such disk burst.

The disk was designed to produce three annular sector fragments and a hub section at failure. The disk possessed the following physical characteristics and was operating at 12,600 rpm when the intentional failure occurred.

- (1) Material: 1020 steel (0.283 lb/cu in.)
- (2) Disk Outer Radius = $R = 3.500$ in.
- (3) Disk Inner Radius = $r = 1.4375$ in.
- (4) Uniform Thickness = $t = 0.375$ in.
- (5) Fragment Included Angle = $\theta = 120^\circ$
- (6) Radius Ratio = $R_R = 0.4107$
- (7) Radial Distance to Fragment Centroid = 2.1614 in.
- (8) Polar Moment of Inertia = $I_o = 0.06474$ in.-lb-sec²

The kinetic energy of the entire disk at the instant of failure (12,600 rpm) (KE_D is equal to $\frac{1}{2}I_o\omega^2$); $KE_D = 56356.5$ in.-lb.

Total Fragment Energy

$$KE_{TOT}/KE_D, \text{ plate 3; } KE_{TOT}/KE_D = 0.323$$

$$KE_{TOT}/KE_D = 18203.1 \text{ in.-lb}$$

This indicates that the total energy possessed by the 1/3 fragment is slightly less than 1/3 of the total energy possessed by the entire disk at failure.

Translational Portion of Total Fragment Energy

$$KE_T/KE_{TOT}, \text{ (Plate 6); } KE_T/KE_{TOT} = 65.3\%$$

$$KE_T/KE_{TOT} = 11891.2 \text{ in.-lb}$$

This indicates that of the total fragment energy (18203.1 in.-lb), only 65.3% is translational in nature.

Translational Kinetic Energy Per Annular Sector Fragment

$$KE_T/KE_D, \text{ (Plate 4); } KE_T/KE_D = 0.211$$

$$KE_T/KE_D = 11891.2 \text{ in.-lb}$$

Total Translational Kinetic Energy

The total amount of translational kinetic energy attacking the containment ring is equal to three times the individual translational kinetic energy per annular sector fragment; i.e., $3 \times 0.211 = 0.633$ or 35673.6 in.-lb.

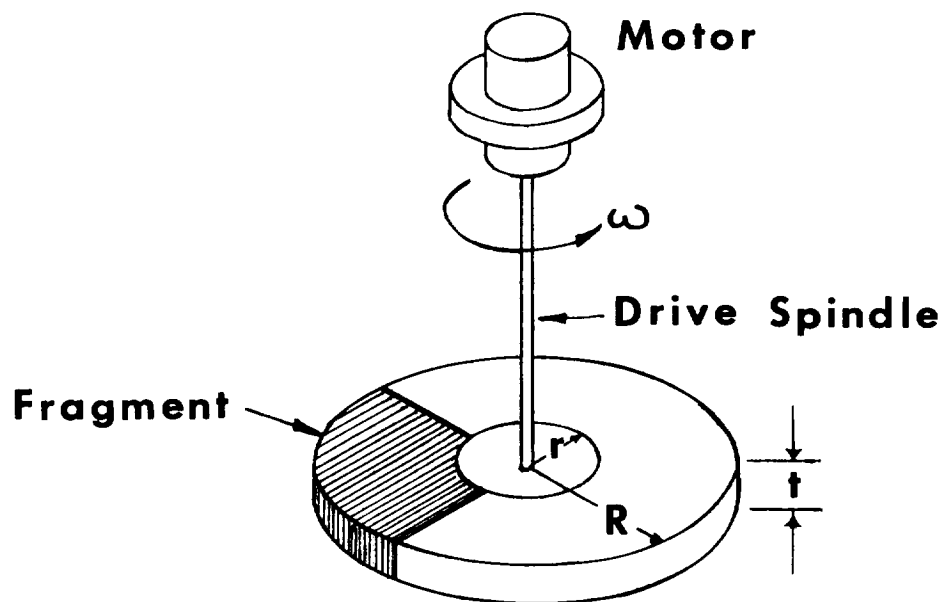
Rotational Kinetic Energy Per Annular Sector Fragment

$$KE_R/KE_D, \text{ (Plate 5); } KE_R/KE_D = 0.112$$

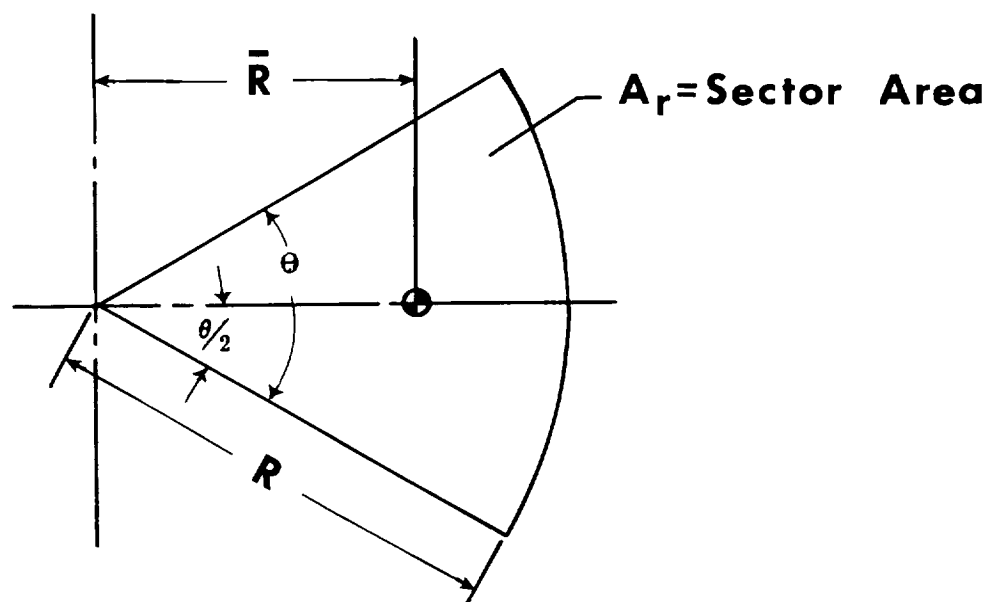
A total rotational kinetic energy per annular sector fragment is equal to 0.112 of the total kinetic energy of the disk just prior to failure, i.e., 6311.9 in.-lb. It is therefore evident that the rotational component of the total kinetic energy of the fragment is equal to 34.7% of the total fragment energy.

REFERENCES

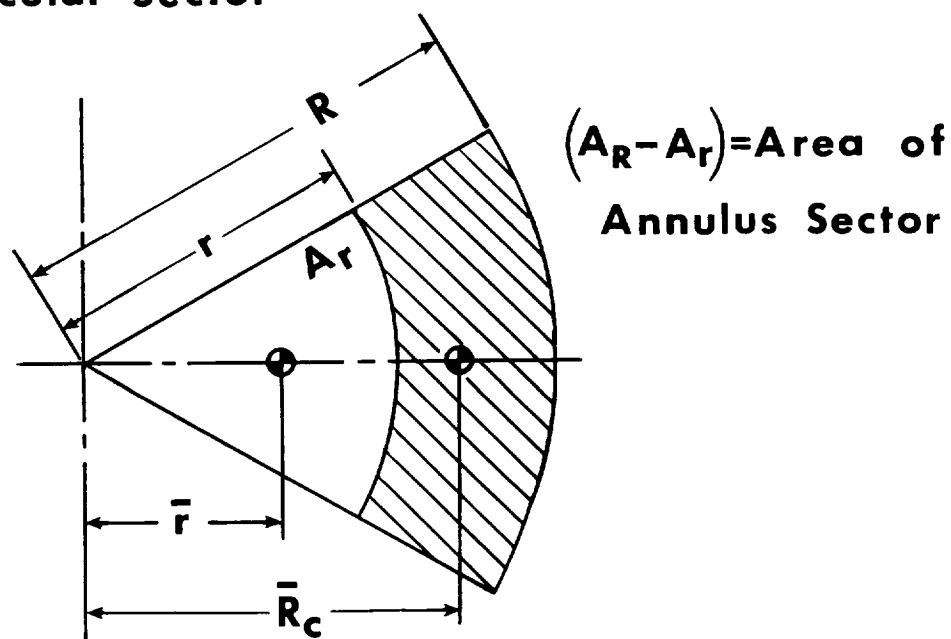
- a. Ingar, U. and Kraushar, W. L., "Introduction to Mechanics, Matter, and Waves", Addison-Wesley Publishing Co., Inc. 1960
- b. Singer, F. L., "Engineering Mechanics", Harper & Brothers, Second Edition, 1954
- c. Paul, R. M., "Disk Energy Profile", Computer Report - Program 0044-A, August 1967.



IDEAL ROTATING SYSTEM

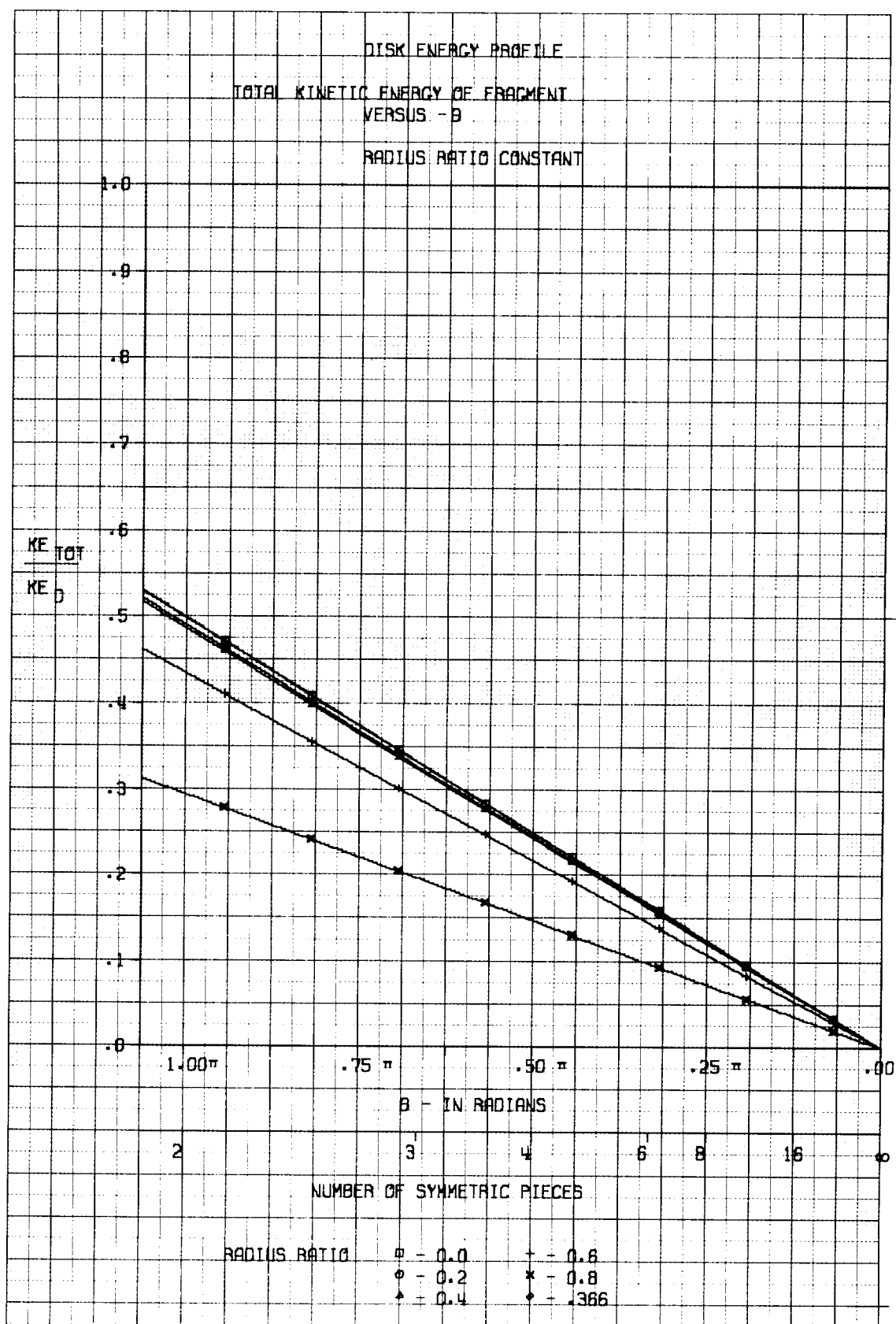


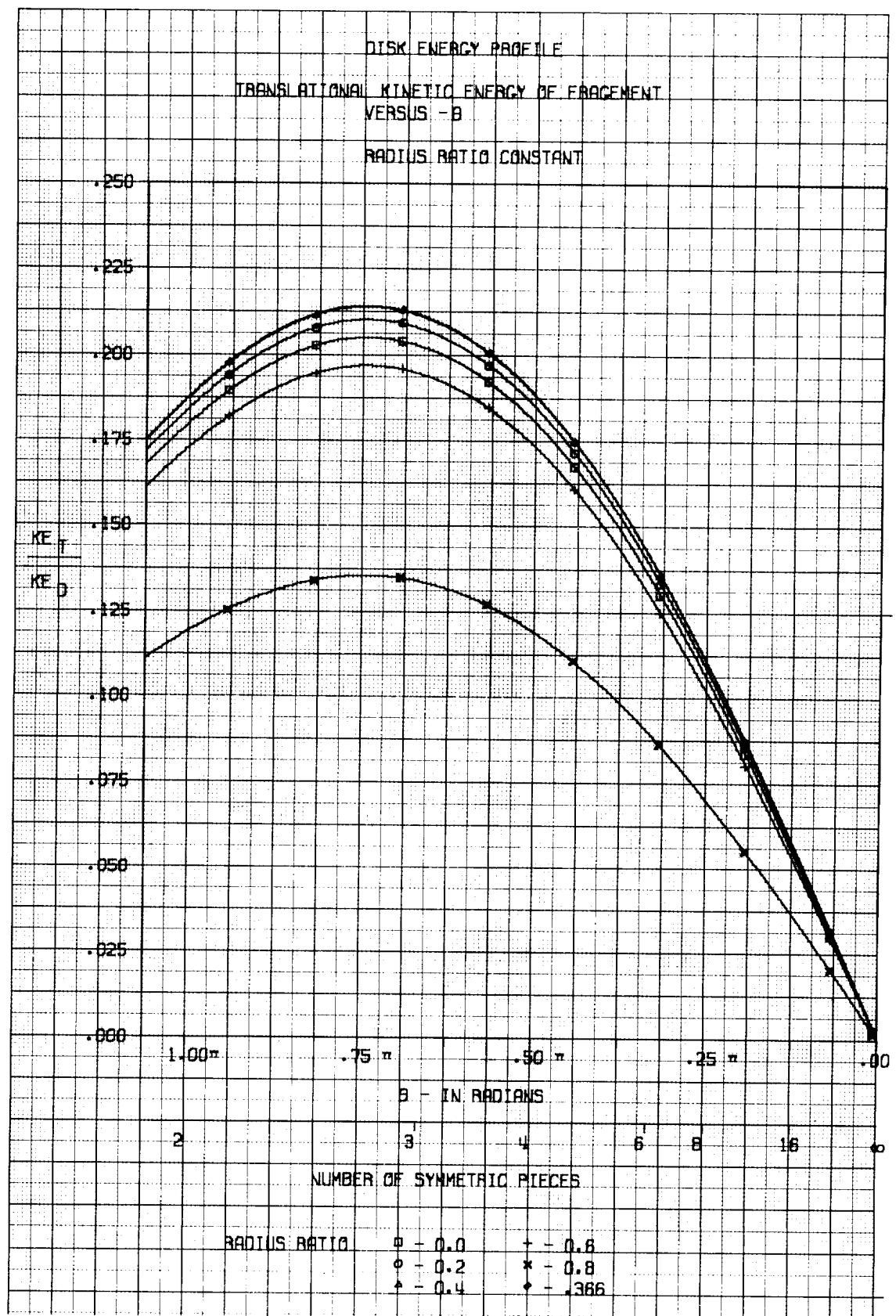
Full Circular Sector

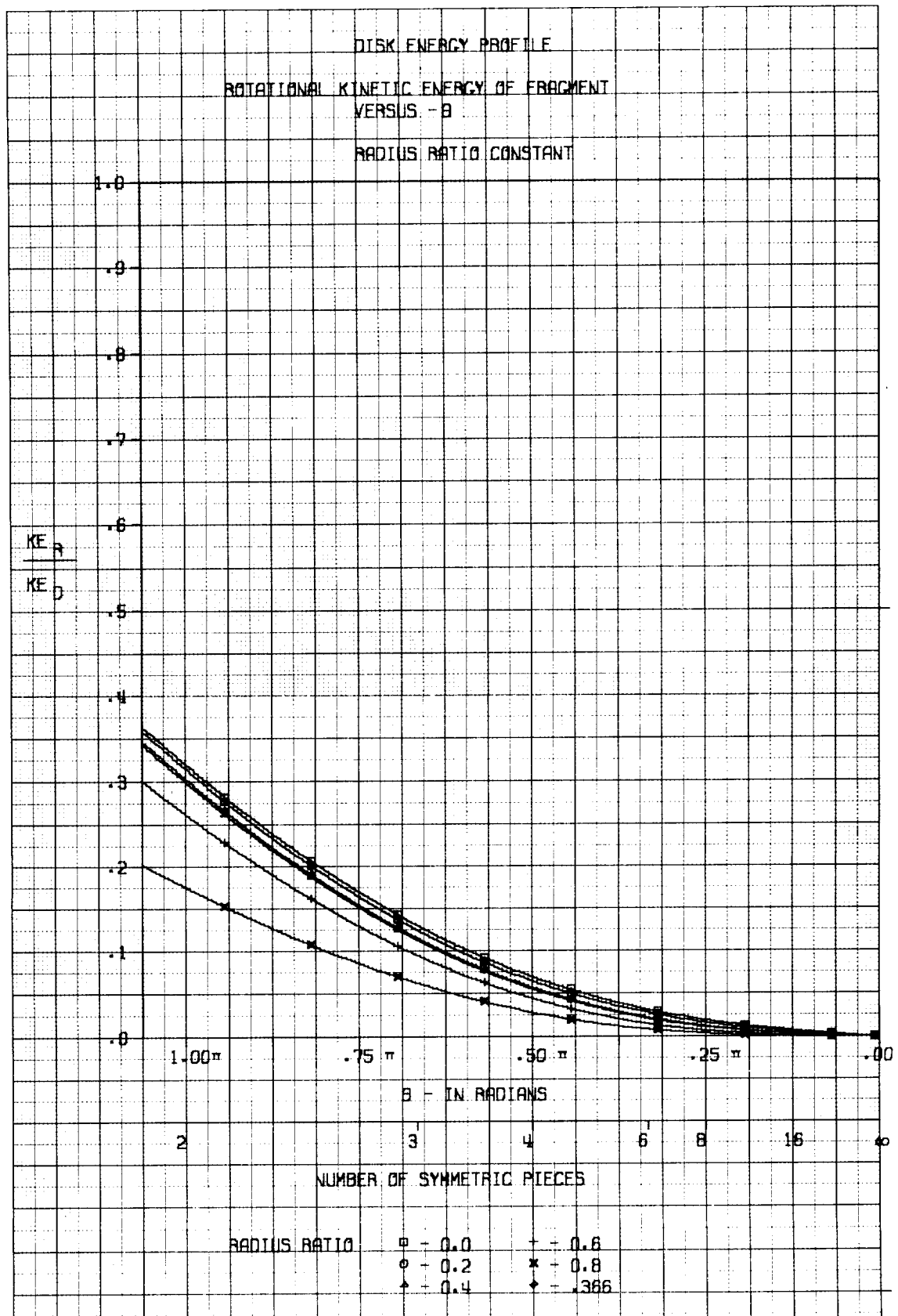


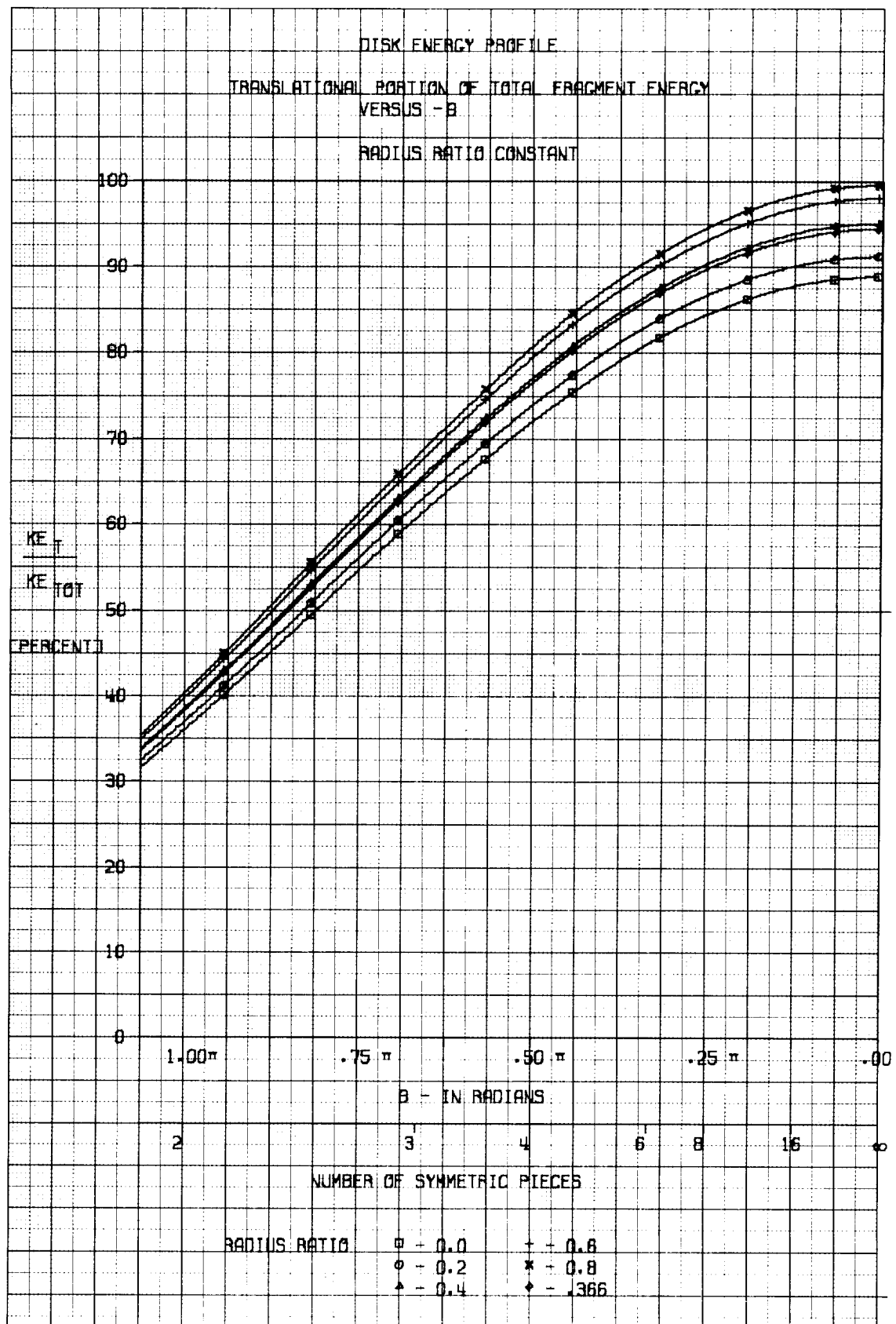
Composite Circular Sector

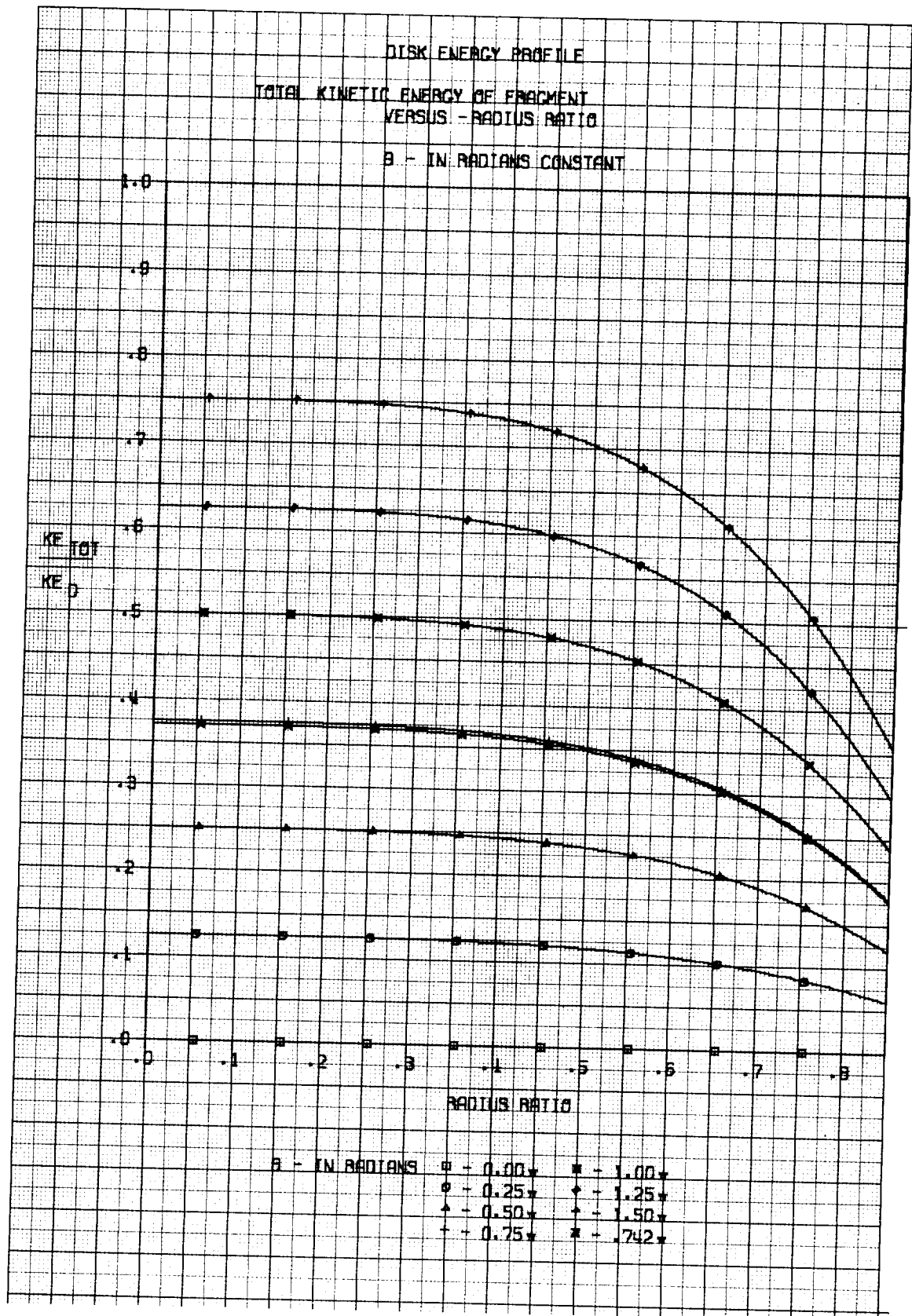
**CENTROID OF THE AREA
OF A CIRCULAR SECTOR**

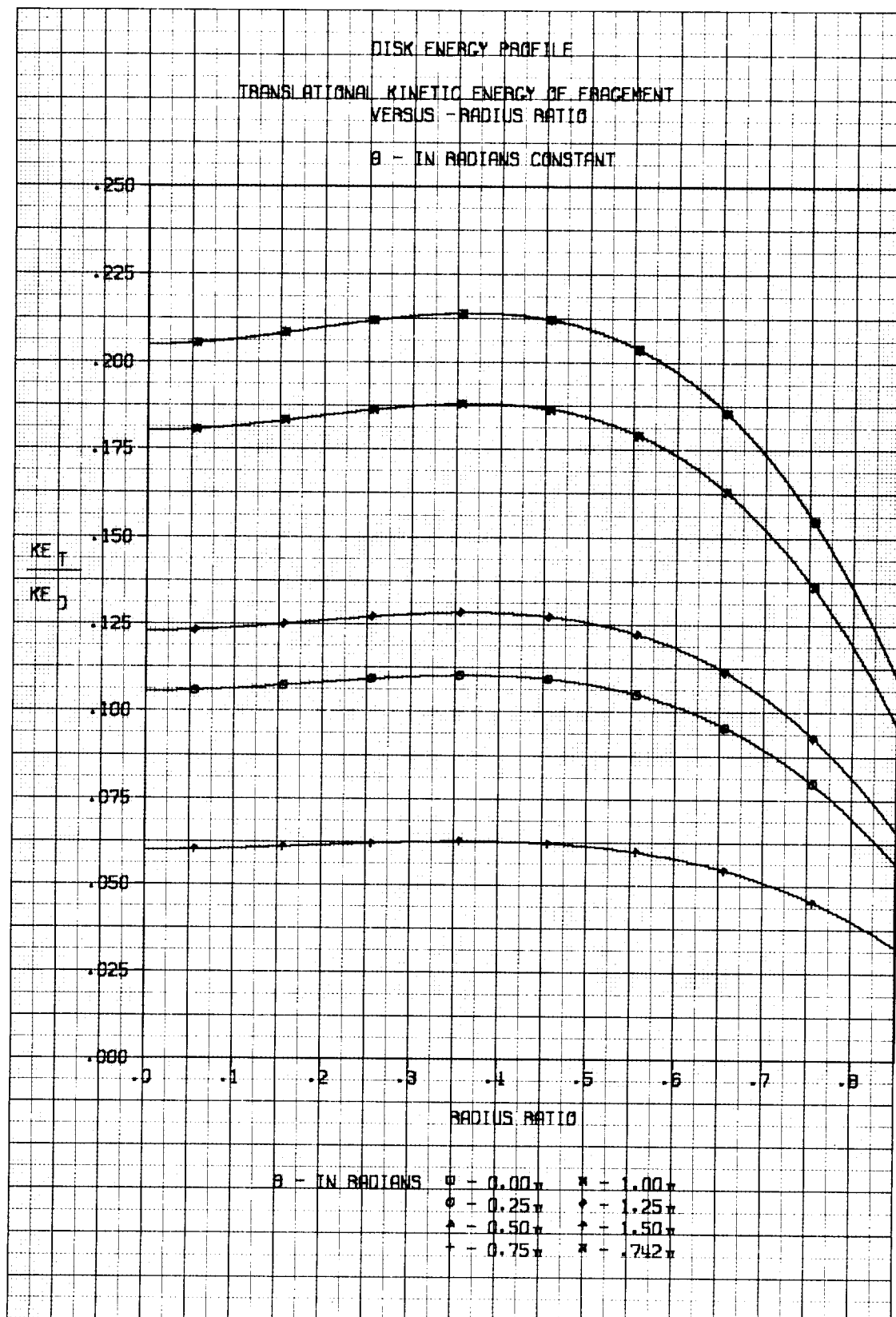


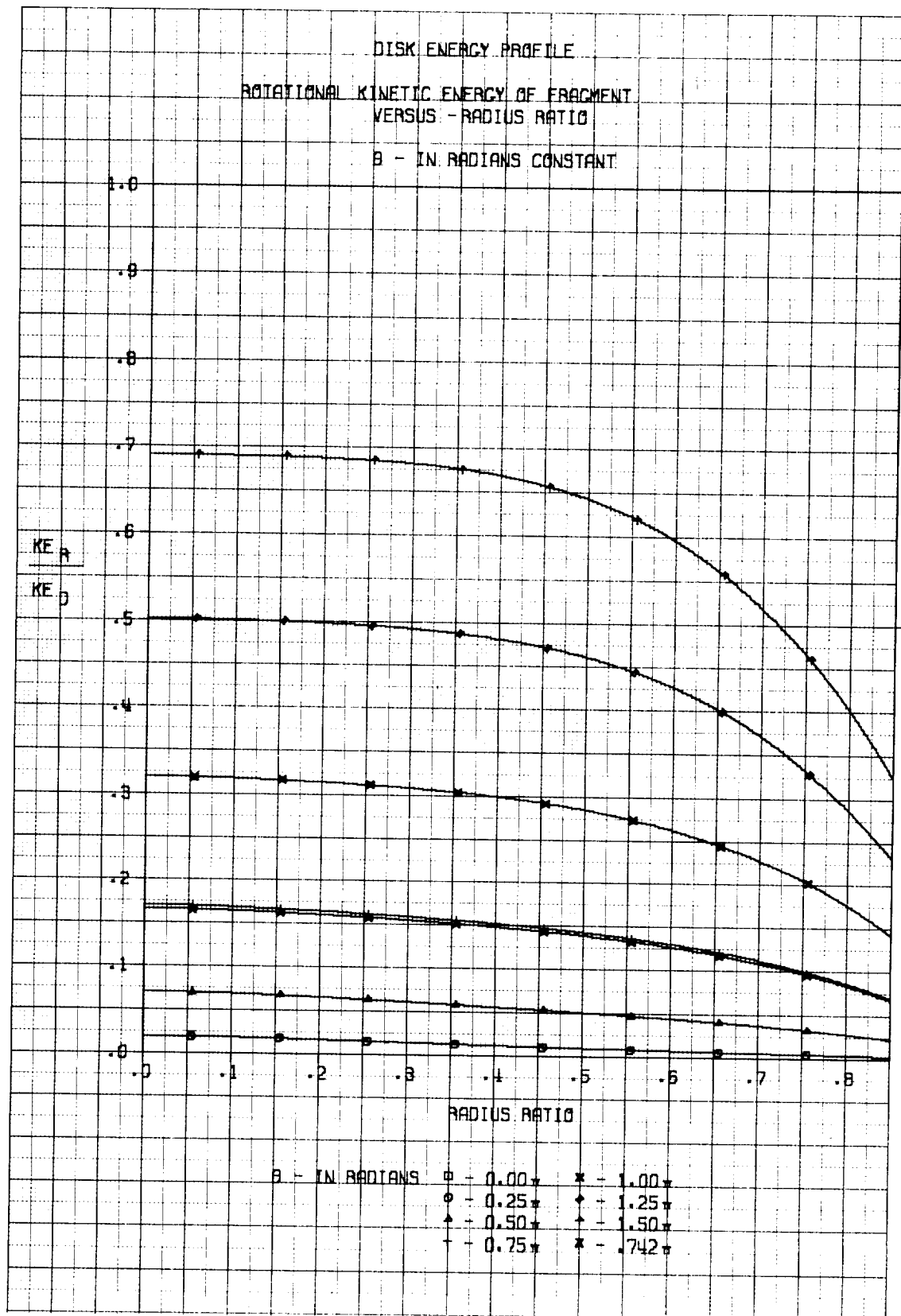


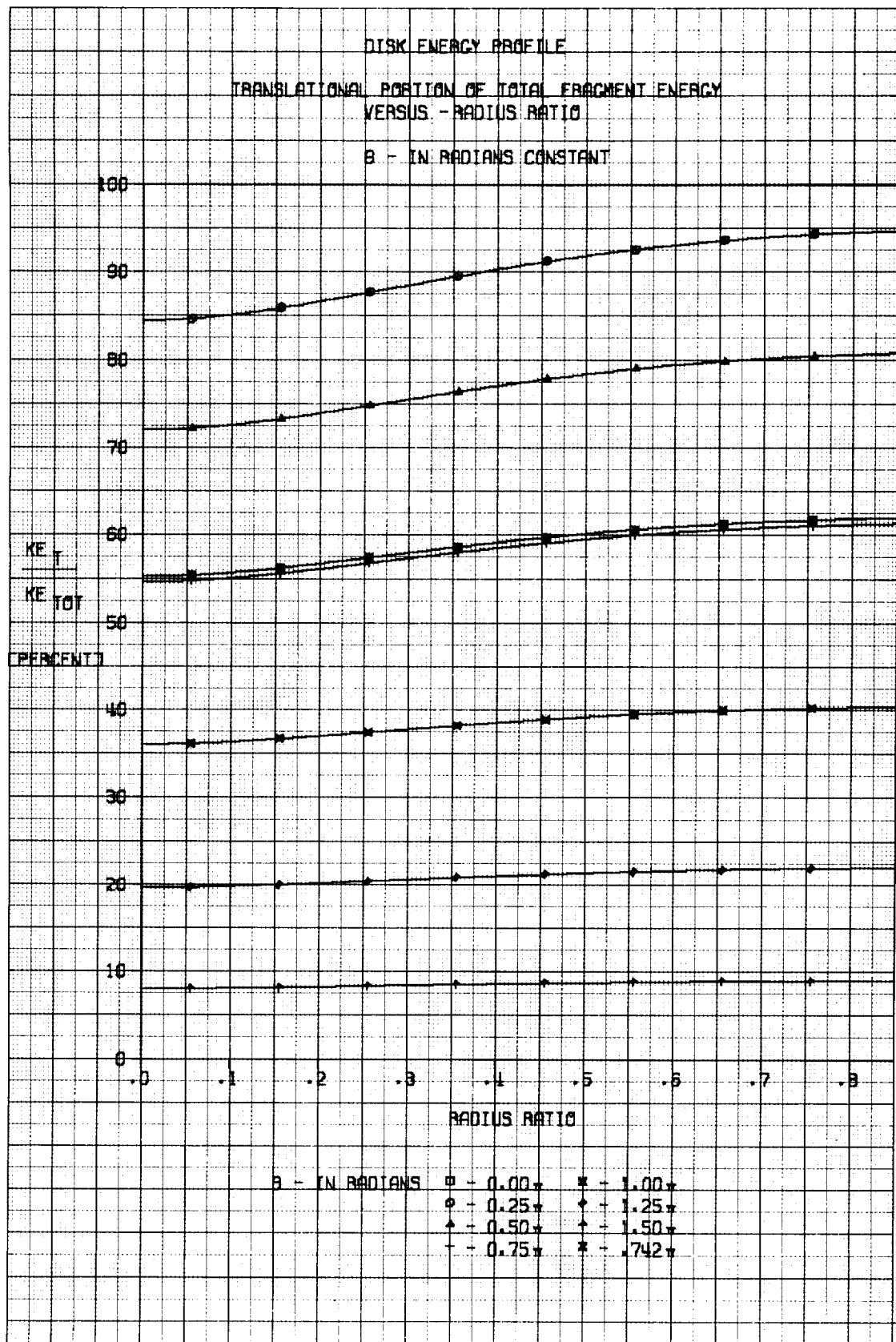












DPR R-105 PHASE IV TEST DATA COMPILATION

A detailed compilation of the 21 tests that were performed during Phase IV of NASA DPR R-105 is presented in plates 1 to 12 of Appendix 3.

This compilation is divided into four sections:

a. Test objectives, photographic coverage, and burst speeds (plates 1, 2, and 3).

b. Fragment generator details (plates 4, 5, and 6).

c. Containment system details (plates 7, 8, and 9).

d. Photographic system details (plates 10, 11, and 12).

The following is a list of symbols used in this compilation:

a. N = No or none

b. Y = Yes or available

c. C = Contained, i.e., no fragment perforated the containment device.

d. Error = Actual speed minus design speed

e. Percent Error = $\frac{\text{Error} \times 100}{\text{Design}}$

f. Detailed photograph of containment device shown in main body of report (plate 46).

g. Detailed drawing and photograph shown in main body of report (plates 34 and 35, respectively).

- h. c.c. = close contact
- i. SAND = Sandwich construction; aluminum-plastic
- j. FOIL = Aluminum foil with SR-4 cement
- k. Visicorder speed record damaged. Speed (21200 rpm)
observed from EPUT digital readout.

Test No.	Test Objective	STILL PHOTOS						BURST SPEED			
		High Speed Photographs	Enlarged Prints	Animation	Polaroids	Pre-test	Post-test	Design (rpm)	Actual (rpm)	Error (d)	Percent Error (e)
1	Rotor Burst Dynamics. Flat Disk Tri-hub Burst	N	N	N	N	N	N	10,000			
2	Rotor Burst Dynamics. Flat Disk Tri-hub Burst	Y	Y	Y	N	N	Y	10,000	12,100	2100	21.00
3	Rotor Burst Dynamics. Flat Disk Tri-hub Burst	N	N	N	N	N	N	13,300	13,500	200	1.503
4	Flat Disk Tri-hub Burst Within a Steel Ring. Large Radial Clearance	Y	Y	Y	Y	N	Y	13,360	13,500	140	1.048
5	Flat Disk Tri-hub Burst Within a Steel Ring. Large Radial Clearance	N	N	N	Y	N	Y	13,360	13,800	440	3.29
6	Flat Disk Tri-hub Burst Within a Steel Ring. Large Radial Clearance	Y	Y	Y	Y	Y	Y	13,360	12,750	-610	-4.56
7	Single "Small" Turbine Blade Dynamics Within a Steel Ring	N	N	N	Y	Y	Y	22,000	21,400	-600	-2.73

Test No.	Test Objective	STILL PHOTOS					BURST SPEED				
		High Speed Photographs	Enlarged Prints	Animation	Polaroids	Pre-test	Post-test	Design (rpm)	Actual (rpm)	Error (d)	Percent Error (e)
8	Material Evaluation - Starter Rotor vs. Energy Absorbent Resin	N	N	N	Y	Y	N	15,000	15,800	800	5.33
9	Material Evaluation - Gas Generator Rotor vs. Doron-Alumina Ring	N	N	N	Y	N	N	26,300	25,000	-1300	-4.94
10	Single "Small" Turbine Blade Dynamics Within a Steel Ring	Y	Y	Y	Y	Y	Y	22,000	21,200 (k)	800	3.64
11	Single "Small" Turbine Blades From a Partially Full Rotor-Steel Ring	N	N	N	Y	N	Y	22,000	19,750	-2250	-10.23
12	Fragment Shape Effects. Tri-hub Burst - Small Radial Clearance	Y	Y	Y	Y	Y	Y	11,820	11,900	80	0.68
13	Fragment Shape Effects. Bi-hub Burst - Small Radial Clearance	Y	Y	Y	Y	N	Y	11,934	15,000	3066	25.69
14	Fragment Shape Effects. Quad-hub Rim Burst - Small Radial Clearance	N	N	N	Y	Y	Y	13,380	14,750	1370	10.24

				STILL PHOTOS			BURST SPEED				
Test No.	Test Objective	High Speed Photographs	Enlarged Prints	Animation	Polaroids	Pre-test	Post-test	Design (rpm)	Actual (rpm)	Error (d)	Percent Error (e)
15	Fragment Shape Effects. Tri-hub Rim Burst - Small Radial Clearance	Y	Y	N	Y	Y	Y	11,950	14,200	2250	18.83
16	Single "Medium" Turbine Blade Dynamics Within a Steel Ring	Y	Y	N	Y	Y	Y	9,540	10,250	710	7.44
17	Material Evaluation - Gas Generator Rotor vs. Doron-Alumina Ring	Y	Y	N	Y	Y	Y	22,400	23,500	1100	4.91
18	Single "Medium" Turbine Blades From a Partially Full Rotor - Steel Ring	N	N	N	Y	N	Y	9,540	13,300	3760	39.41
19	Material Evaluation - Starter Rotor vs. Nylon Backed Energy Absorbent Resin	N	N	N	Y	Y	N	15,000	11,600	-3400	-22.67
20	Tri-hub Starter Rotor Burst Within a Steel Ring	Y	Y	N	Y	Y	Y	15,000	16,750	1750	11.67
21	Fragment Shape Effects. Quad-hub Rim Burst - Small Radial Clearance	Y	Y	N	Y	Y	Y	13,380	11,600	-1780	-13.30

A3-

FRAGMENT GENERATOR												
Test No.	Type	No. of Fragments	Rotor Dia. (in.)	Disk Thickness (in.)	Blade Fragment Length (in.)	Disk Weight (lb)	Fragment Weight (lb)	Fragment Centroid (in.)	Radius Ratio	Material	UTS (K psi)	Hardness (R _C)
1	Flat Disk	3	7.00	0.375		3.95	1.147	2.6562	0.410	1020	65	
2	Flat Disk	3	7.00	0.375		3.95	1.147	2.6562	0.410	1020	65	
3	Flat Disk	3	7.00	0.375		3.95	1.147	2.6562	0.410	1020	65	
4	Flat Disk	3	7.00	0.375		3.95	1.144	2.6562	0.410	4130HT	230	
5	Flat Disk	3	7.00	0.375		3.95	1.144	2.6562	0.410	4130HT	230	
6	Flat Disk	3	7.00	0.375		3.95	1.35	2.6562	0.410	4130HT	230	
7	Small Engine Turbine Rotor	4	14.00	Vari.	3.5		0.08	4.8125		A286	140	24-35

FRAGMENT GENERATOR												
Test No.	Type	No. of Fragments	Rotor Dia. (in.)	Disk Thickness (in.)	Blade Fragment Length (in.)	Disk Weight (lb)	Fragment Weight (lb)	Fragment Centroid (in.)	Radius Ratio	Material	UTS (K psi)	Hardness (R _C)
8	Starter Rotor	3	6.75	0.75		3.611	1.107	1.74		4340	170	38-42
9	Small Engine Gas Generator Rotor	3	10.64	VAR.			1.7306	2.4628		A286	140	24-35
10	Small Engine Turbine Rotor	4	14.0	VAR.	3.5		0.08	4.8125		SEL		
11	Small Engine Turbine Rotor	4	14.0	VAR.	3.5		0.08	4.8125		SEL		
12	Flat Disk	3	7.00	0.375		3.95	1.178	2.118	0.411	4130HT	200	34
13	Flat Disk	2	7.00	0.375		3.95	1.768	1.6318	0.411	4130HT	200	34
14	Flat Disk	4	7.00	0.375		3.95	0.884	2.305	0.411	4130HT	200	34

FRAGMENT GENERATOR												
Test No.	Type	No. of Fragments	Rotor Dia. (in.)	Disk Thickness (in.)	Blade Fragment Length (in.)	Disk Weight (lb)	Fragment Weight (lb)	Fragment Centroid (in.)	Radius Ratio	Material	UTS (K psi)	Hardness (R _C)
15	Flat Disk	3	7.00	0.375		3.95	0.490	2.617	0.800	4130HT	200	34
16	Medium Engine Turbine Rotor	3	30.64	VARI.	3.18		0.165	13.38		INCO 700	170	27-35
17	Small Engine Gas Generator Rotor	3	10.64	VARI.			1.7306	2.4628		A286 & SEL	140	24-35
18	Medium Engine Turbine Rotor	3	30.64	VARI.	3.18							
19	Starter Rotor	3	6.75	0.75		3.611		1.72		4340	170	29
20	Starter Rotor	3	6.75	0.75		3.611	1.122	1.72		4340	170	29
21	Flat Disk	4	7.00	0.375		3.95	0.884	2.305	0.411	4130HT	200	34

CONTAINMENT DEVICE										
Test No.	Type	Degree of Containment	Inside Diameter (in.)	Radial Thickness (in.)	Axial Width (in.)	Material	UKS (K psi)	% Elogation in 2"	Hardness (R _C)	Total Weight (lb)
1	None									
2	None									
3	None									
4	Ring	N	18.00	0.625	3.0	316 SS	90	45	12	3.015
5	Ring	C	14.95	0.252	3.0	1020	65	36	78R _B	10.06
6	Ring	N	14.95	0.228	3.0	1020	65	36	78R _B	9.36
7	Ring	C	14.95	0.250	3.0	1020	65	36	78R _B	10.14

CONTAINMENT DEVICE										
Test No.	Type	Degree of Containment	Inside Diameter (in.)	Radial Thickness (in.)	Axial Width (in.)	Material	UTS (K psi)	% Elongation in 2"	Hardness (RC)	Total Weight (lb)
8	Ring	N	9.25	1.00	2.00	Energy Absorbent Resin	263 x10 ⁻³	2.56		4.73
9	$\frac{1}{2}$ - Pentagon $\frac{1}{2}$ - Circular (f)	N	(6)	(6)	(6)	Doron Alumina				
10	Ring	C	15.375	0.125	3.0	1020	65	36	78RB	5.175
11	Ring	C	15.375	0.125	3.0	1020	65	36	78RB	5.175
12	Ring with thin center section(g)	N	7.875	0.04685 Center Sec	3.0	316 SS	90	45	12	4.299
13	Ring with thin center section(g)	C	7.875	0.04685 Center Sec	3.0	316 SS	90	45	12	4.196
14	Ring with thin center section(g)	N	7.875	0.04685 Center Sec	3.0	316 SS	90	45	12	4.279

CONTAINMENT DEVICE										
Test No.	Type	Degree of Containment	Inside Diameter (in.)	Radial Thickness (in.)	Axial Width (in.)	Material	UTS (K psi)	% Elongation in 2"	Hardness (R _C)	Total Weight (lb)
15	Ring with thin center section (g)	C	7.875	0.04685 Center Sec	3.0	316 SS	90	45	12	4.315
16	Ring	C	31.3125	0.1875	3.0	1020	65	36	78R _B	15.78
17	$\frac{1}{2}$ -Pentagon $\frac{1}{2}$ -Circular (f)	N	(f)	(f)	(f)	Doron-Alumina				
18	Ring	N	31.3125	0.1875	3.0	1020	65	36	78R _B	15.78
19	Ring		9.25	1.00	2.0	Energy Absorbent Resin with a nylon backing	263 x10-3	2.56		
20	Ring	C	9.1875	0.267	2.11	1020	65	36	78R _B	4.751
21	Ring with thin center section (g)	C	7.875	0.04685 CenterSect.	3.0	316 SS	90	45	12	4.262

PHOTOGRAPHIC SYSTEM													
CAMERA								LIGHTING				FILM	
Test No.	Framing Rate (pps)	Quantity of Pictures	Total Writing Time (msec)	Frame Interval Time (μsec)	Stop Size	Lens Setting (mm)	No. of Lights	Light Duration (msec)	Intensity (10 ⁻⁶ BCP)	Triggering Mode	Type Grid	Type	Developer
1	5000	0	5.4	200	3/16	50	1	5.4	3.0	c.c (h)	Vert.	2475	
2	5000	27	5.4	200	3/16	50	1	5.4	3.0	c.c	Vert.	2475	DK-50
3	4600	0	5.4	220	3/16	50	1	5.4	3.0	c.c	Vert.	2475	
4	5400	29	5.4	188	3/8	75	1	5.4	3.0	c.c	Vert.	2475	DK-50
5	5300	0	5.4	190	3/8	37	1	5.4	3.0	c.c	Vert.	2475	
6	5500	29	5.4	184	3/8	37	1	5.4	3.0	c.c	(i) Sand.	2475	DK-50
7	15000	0	10.8	66.6	3/8		1	10.8	1.5	c.c	Sand.	2475	

PHOTOGRAPHIC SYSTEM													
CAMERA							LIGHTING				FILM		
Test No.	Framing Rate (pps)	Quantity of Pictures	Total Writing Time (msec)	Frame Interval Time (μsec)	Stop Size	Lens Setting (mm)	No. of Lights	Light Duration (msec)	Intensity (10 ⁻⁶ BCP)	Triggering Mode	Type Grid	Type	Developer
8	7500	0	10.8	138			1	10.8	1.5	c.c	Horiz.	2475	
9	10000	0	10.8	98.0	3/8		2	10.8	1.5	c.c	Horiz.	2475	
10	15000	56	5.4	66.6	3/8		2	5.4	3.0	c.c	Foil (5)	Tri-X	Dektol
11	7500	154	10.8	135.0	3/8		2	10.8	1.5	c.c	Sand.	2475	DK-50
12	13100	131	10.8	78	3/8		2	10.8	1.5	c.c	Vert.	2475	DK-50
13	13800	142	10.8	73	3/8		2	10.8	1.5	c.c	Vert.	2475	DK-50
14	13500	0	10.8	76	3/8		2	10.8	1.5	c.c	Vert.	2475	DK-50

PHOTOGRAPHIC SYSTEM													
CAMERA							LIGHTING					FILM	
Test No.	Framing Rate (pps)	Quantity of Pictures	Total Writing Time (msec)	Frame Interval Time (μsec)	Stop Size	Lens Setting (mm)	No. of Lights	Light Duration (msec)	Intensity (10 ⁻⁶ BCP)	Triggering Mode	Type Grid	Type	Developer
15	13500	131	10.8	76	3/8		2	10.8	1.5	c.c	Vert.	2475	DK-50
16	10500	168	10.8	96	3/8	23	2	10.8	1.5	c.c	Horiz.	2475	DK-50
17	13700	151	10.8	72.5	3/8		2	10.8	1.5	c.c	Horiz. Wire	2475	DK-50
18	10000	0	10.8	99	3/8		2	10.8	1.5	c.c	Horiz. Wire	2475	DK-50
19	5000	154	10.8	200	3/8	40	2	10.8		c.c	Horiz. Wire	2475	DK-50
20	10500	102	10.8	95	3/8	45	2	10.8		c.c	Vert.	2475	DK-50
21	10000	208	10.8	98	3/8		2	10.8	1.5	c.c	Vert.	2475	DK-50

NAVAL AIR PROPULSION TEST CENTER
AERONAUTICAL ENGINE DEPARTMENT
NAVAL BASE, PHILADELPHIA, PA. 19112

Rotor Burst Protection Program
A. A. Martino & G. J. Mangano

1. Report No.
NAPTC-AED 1869
P.A. No.
2. NASA DFR R-105
Phase IV

The NASA sponsored Rotor Burst Protection program has produced the first high speed photographic sequence of an intentionally failed rotor within a containment device. This technical achievement has provided a means to study the fragment containment system kinematics and material performance associated with disk and blade failures. The results of the first twenty-one tests provide data that can assist in establishing basic guidelines for the design of containment systems. Experiments providing information relative to the complex motion of disk and blade fragments from a failed rotor, and the effects of radial clearance, stress concentration, and material properties are reported. The theoretical derivation and related curves for the energy distribution of fragments from a rotating flat disk provide the total, translational, and rotational kinetic energy per fragment for combinations of fragment included angle and radius ratio are presented. A survey of uncontained failures occurring in U.S. Commercial and Naval aviation experience is reported. Test equipment and techniques are discussed.

NAVAL AIR PROPULSION TEST CENTER
AERONAUTICAL ENGINE DEPARTMENT
NAVAL BASE PHILADELPHIA, PA. 19112

Rotor Burst Protection Program
A. A. Martino & G. J. Mangano

1. Report No.
NAPTC-AED 1869
P.A. No.
2. NASA DFR R-105
Phase IV

The NASA sponsored Rotor Burst Protection program has produced the first high speed photographic sequence of an intentionally failed rotor within a containment device. This technical achievement has provided a means to study the fragment containment system kinematics and material performance associated with disk and blade failures. The results of the first twenty-one tests provide data that can assist in establishing basic guidelines for the design of containment systems. Experiments providing information relative to the complex motion of disk and blade fragments from a failed rotor, and the effects of radial clearance, stress concentration, and material properties are reported. The theoretical derivation and related curves for the energy distribution of fragments from a rotating flat disk provide the total, translational, and rotational kinetic energy per fragment for combinations of fragment included angle and radius ratio are presented. A survey of uncontained failures occurring in U.S. Commercial and Naval aviation experience is reported. Test equipment and techniques are discussed.

NAVAL AIR PROPULSION TEST CENTER
AERONAUTICAL ENGINE DEPARTMENT
NAVAL BASE, PHILADELPHIA, PA. 19112

Rotor Burst Protection Program
A. A. Martino & G. J. Mangano

1. Report No.
NAPTC-AED 1869
P.A. No.
2. NASA DFR R-105
Phase IV

The NASA sponsored Rotor Burst Protection program has produced the first high speed photographic sequence of an intentionally failed rotor within a containment device. This technical achievement has provided a means to study the fragment containment system kinematics and material performance associated with disk and blade failures. The results of the first twenty-one tests provide data that can assist in establishing basic guidelines for the design of containment systems. Experiments providing information relative to the complex motion of disk and blade fragments from a failed rotor, and the effects of radial clearance, stress concentration, and material properties are reported. The theoretical derivation and related curves for the energy distribution of fragments from a rotating flat disk provide the total, translational, and rotational kinetic energy per fragment for combinations of fragment included angle and radius ratio are presented. A survey of uncontained failures occurring in U.S. Commercial and Naval aviation experience is reported. Test equipment and techniques are discussed.

NAVAL AIR PROPULSION TEST CENTER
AERONAUTICAL ENGINE DEPARTMENT
NAVAL BASE PHILADELPHIA, PA. 19112

Rotor Burst Protection Program
A. A. Martino & G. J. Mangano

1. Report No.
NAPTC-AED 1869
P.A. No.
2. NASA DFR R-105
Phase IV

The NASA sponsored Rotor Burst Protection program has produced the first high speed photographic sequence of an intentionally failed rotor within a containment device. This technical achievement has provided a means to study the fragment containment system kinematics and material performance associated with disk and blade failures. The results of the first twenty-one tests provide data that can assist in establishing basic guidelines for the design of containment systems. Experiments providing information relative to the complex motion of disk and blade fragments from a failed rotor, and the effects of radial clearance, stress concentration, and material properties are reported. The theoretical derivation and related curves for the energy distribution of fragments from a rotating flat disk provide the total, translational, and rotational kinetic energy per fragment for combinations of fragment included angle and radius ratio are presented. A survey of uncontained failures occurring in U.S. Commercial and Naval aviation experience is reported. Test equipment and techniques are discussed.

DOCUMENT CONTROL DATA - R&D

(Security classification of title, body of abstract and indexing annotation must be entered when the overall report is classified)

1. ORIGINATING ACTIVITY (Corporate author) NAVAL AIR PROPULSION TEST CENTER AERONAUTICAL ENGINE DEPARTMENT PHILADELPHIA, PA. 19112		2a. REPORT SECURITY CLASSIFICATION UNCLASSIFIED	
		2b. GROUP	
3. REPORT TITLE Rotor Burst Protection Program Initial Test Results			
4. DESCRIPTIVE NOTES (Type of report and inclusive dates) Final Phase IV Report			
5. AUTHOR(S) (Last name, first name, initial) MARTINO, Albert A. MANGANO, Gaetan J.			
6. REPORT DATE		7a. TOTAL NO. OF PAGES 161	7b. NO. OF REFS 7
8a. CONTRACT OR GRANT NO.		9a. ORIGINATOR'S REPORT NUMBER(S) NAPTC-AED-1869	
b. PROJECT NO. NASA DPR R-105			
c.		9b. OTHER REPORT NO(S) (Any other numbers that may be assigned this report)	
d.			
10. AVAILABILITY/LIMITATION NOTICES N/A			
11. SUPPLEMENTARY NOTES		12. SPONSORING MILITARY ACTIVITY National Aeronautics and Space Administration	
13. ABSTRACT The NASA sponsored Rotor Burst Protection program has produced the first high speed photographic sequence of an intentionally failed rotor within a containment device. This technical achievement has provided a means to study the fragment-containment system kinematics and material performance associated with disk and blade failures. The results of the first twenty-one tests provide data that can assist in establishing basic guidelines for the design of containment systems. Experiments providing information relative to the complex motion of disk and blade fragments for a failed rotor, and the effects of radial clearance, stress concentration, and material properties are reported. The theoretical derivation and related curves for the energy distribution of fragments from a rotating flat disk provide the total, translational, and rotational kinetic energy per fragment for combinations of fragment included angle and radius ratio are presented. A survey of uncontained failures occurring in U.S. Commercial and Naval aviation experience is reported. Test equipment and techniques are discussed.			